QCD cross section measurements with the OPAL and ATLAS detectors

Ph.D. thesis

Attila Krasznahorkay Jr.

Supervisors: Dr. Dezső Horváth,
Dr. Thorsten Wengler

University of Debrecen
Faculty of Sciences and Technology
Debrecen, 2008

Ezen értekezést a Debreceni Egyetem TTK Fizikus Doktori Iskola Részecskefizika programja keretében készítettem a Debreceni Egyetem TTK doktori (PhD) fokozatának elnyerése céljából.

Debrecen, 2008, ...

Ifj. Krasznahorkay Attila
jelölt

Tanúsítom, hogy Ifj. Krasznahorkay Attila doktorjelölt 2004–2008 között a fent megnevezett Doktori Iskola Részecskefizika programjának keretében irányításommal végezte munkáját. Az értekezésben foglalt eredményekhez a jelölt önálló alkotó tevékenységével meghatározóan hozzájárult. Az értekezés elfogadását javaslom.

Debrecen, 2008, ...

Dr. Horváth Dezső
témavezető

I certify that Attila Krasznahorkay Jr., doctoral candidate, has done his work under my supervision during 2004-2008 in the particle physics program of the above mentioned PhD school. The candidate has contributed significantly with autonomous creative work to the results presented in this thesis. I propose the thesis to be accepted.

Debrecen, 2008, ...

Dr. Thorsten Wengler
supervisor

QCD cross section measurements with the OPAL and ATLAS detectors

Értekezés a doktori (Ph.D.) fokozat megszerzése érdekében
a fizika tudományágban

Írta: Ifj. Krasznahorkay Attila okleveles fizikus

Készült a Debreceni Egyetem Fizikai-tudományok doktori iskolája
(Részecskefizikai programja) keretében

Témavezetők: Dr. Horváth Dezső,
Dr. Thorsten Wengler

A doktori szigorlati bizottság:

elnök:	Dr.	.....
tagok:	Dr.	.....
	Dr.	.....

A doktori szigorlat időpontja: 200... . .....

Az értekezés bírálói:

Dr.	.....
Dr.	.....
Dr.	.....

A bírálóbizottság:

elnök:	Dr.	.....
tagok:	Dr.	.....
	Dr.	.....
	Dr.	.....
	Dr.	.....

Az értekezés védésének időpontja: 200... . .....

"A man should look for what is,
and not for what he thinks should be."

Albert Einstein

Contents

Introduction

Since the beginning of mankind two questions have always concerned the brightest minds of their time: What are we made of, and why does the world work like it does? Over the course of history many theories were developed to answer these questions, all of which were able to describe the observations of their present age.

Our understanding of the most basic constituents and laws of the Universe has improved enormously over the last few decades thanks to the experiments performed at the highest achievable energies. From the large number of observations a single theory was born that could explain all the observed phenomena. It was named the Standard Model of Particle Physics – the Standard Model for short.

While the Standard Model is supported by a large number of experimental observations, it has also a few shortcomings. Some of the most important problems can be summarised as follows:

- How is the mass of elementary particles generated? The gauge symmetries upon which the Standard Model is built, do not allow particles to have a mass. The Standard Model explains the observed weight of the elementary particles by a local symmetry breaking, that generates masses for the particles. As a "side-effect", this model predicts the Higgs particle that has not been experimentally observed yet.

- Is it possible to unite the electro-weak and strong interactions – and maybe even gravity – into a single theory? Our findings show that the elementary interactions become similar to each other at increasingly high energies. But the Standard Model in its current form cannot describe this unification of the forces.

- What is dark matter made of? Cosmological observations suggest that the matter that we can see, makes up only about 15% of the matter in the Universe. The other 85% of matter, the gravitational force of which we can see, is currently invisible to us, and the Standard Model gives no explanation to its existence.

There are currently a multitude of theories which provide solutions for these issues. Perhaps the most acknowledged ones are the supersymmetry (SUSY) theories. While these theories provide solutions to the aforementioned problems, they also suggest the existence of yet unseen particles and interactions.

All of the large particle physics experiments of the last decades were designed to test the predictions of the Standard Model at higher and higher energies, and to look for signals of physics beyond the Standard Model. The Large Electron Positron Collider (LEP) for instance provided the first precision measurements of the properties of the weak bosons, and was later on used to study many Standard Model processes.

In 2003 I joined the work of one of the experiments that was built at LEP, the OPAL experiment. I started working in the two-photon working group, studying the interactions of high energy photons with each other. These interactions allow us to study the behaviour of one of the most fundamental constituents of the Standard Model under unusual circumstances, providing very precise tests for our ability to describe quantum electro-dynamics (QED), and quantum chromo-dynamics (QCD).

The most powerful particle accelerator ever built – the Large Hadron Collider (LHC) – is now entering its turn-on phase. The main goals of the LHC are to find the Higgs boson – or to prove that it does not exist –, verify predictions of the Standard Model at the highest energies, and to look for the predicted new particles and interactions.

In 2004 I became a member of the ATLAS collaboration, building the largest experiment for the LHC, the ATLAS detector. I joined the trigger group, working for the most part on the Level-1 and muon triggers, and got involved in the work of the bottom and top quark physics groups. Unlike at the LEP experiments, the trigger system plays a central role in every experiment built for the LHC. In order to be able to observe processes with very small probabilities, the LHC will generate proton–proton collisions with an intensity never seen before. This implies that only a small fraction of the generated data can be saved for further processing. In this way every single physics analysis performed at the LHC will have to know precisely how the trigger behaved when selecting events interesting for that particular analysis.

In the first part of my thesis I present an analysis that I performed in the two-photon group of the OPAL collaboration, measuring the cross section to produce hadron-showers (jets) in photon–photon interactions. In the second part of my thesis I present two studies I have done in the trigger group of the ATLAS collaboration for measuring and optimising the performance of the muon trigger for selecting events from B-hadron and top quark decays, which will be instrumental for measuring various cross sections with the ATLAS detector.

Part I

Inclusive jet production cross section measurement in photon–photon collisions at OPAL

CHAPTER 1

$\gamma\gamma$ interactions at LEP

The photon is a fundamental particle in our current understanding of the interactions of elementary particles. These interactions are successfully described by the Standard Model of Particle Physics, which is a combination of gauge theories [1]. The photon is the gauge boson of quantum electrodynamics (QED) and mediates the electromagnetic force between charged particles. In QED interactions, the photon can be regarded as a point-like, structure-less object, called the *direct*, or *bare* photon. QED being an abelian gauge theory, the photon has no self-couplings, and to our current understanding, the photon has no mass.

In this chapter I will describe the photon as a particle with a structure, that can have self-interactions, and show the framework in which such interactions can be studied. Then I discuss jet production in photon–photon interactions, and show how the study of such interactions helps us to understand the photon itself.

1.1 The photon structure

While the direct photon shows no structure, following the Heisenberg uncertainty principle, written as[1]

$$\Delta E \Delta t \geq \frac{1}{2}\,, \tag{1.1}$$

the photon is allowed to violate the energy conservation rule by ΔE amount for a Δt length of time. In this time the photon is allowed to fluctuate into a fermion anti-fermion pair ($\mathrm{f\bar{f}}$), carrying the same quantum numbers as the photon, with the

$$\gamma \rightarrow \mathrm{f\bar{f}} \rightarrow \gamma \tag{1.2}$$

[1] Throughout this thesis I shall use $c = \hbar = 1$.

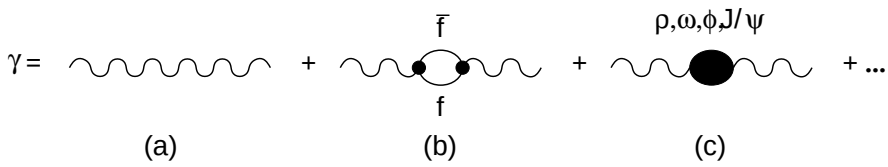

Figure 1.1: The resolved photon. In QCD the photon is a superposition of the direct (a), anomalous (b) and hadronic (c) part of the particle.

reaction. If during a fluctuation one of the fermions[2] interacts via a gauge boson with another particle, then it can be extracted from the photon, with the photon getting *resolved* and revealing its structure.

In the framework of QED, the photon is coupled to charged fermions, which either means leptons, l, with $l = e, \mu, \tau$, or quarks. The case of lepton pair production can be calculated in QED. Quark pair production is more complex, since there are more kinds of possible fluctuations, and QCD corrections have to be taken into account. In leading order the photon can take part in a reaction in three ways:

- The photon can interact directly, as shown in Figure 1.1 (a), and it does not reveal a structure. In these cases the photon is called a *direct* or *bare* photon.

- The photon can fluctuate into a leptonic or hadronic state in a way that is perturbatively calculable – shown in Figure 1.1 (b) –, in which case it is called the *point-like* or *anomalous* photon.

- The photon can fluctuate into a hadronic state that has the same quantum numbers as the photon ($J^{PC} = 1^{--}$) – shown in Figure 1.1 (c) –, in which case it is called the *hadron-like* or *hadronic* photon. The photon behaves like a hadron, and the hadron-like part of the hadronic photon structure function can successfully be described by the vector meson dominance model (VMD), considering the low mass vector mesons ρ, ω, ϕ and J/Ψ.

The fact that the photon can either interact directly or in a resolved manner adds another duality to the nature of the photon, and makes it a very interesting particle to investigate.

[2]Fermions and anti-fermions are not distinguished in this thesis. For instance electrons and positrons will be referred to uniformly as electrons.

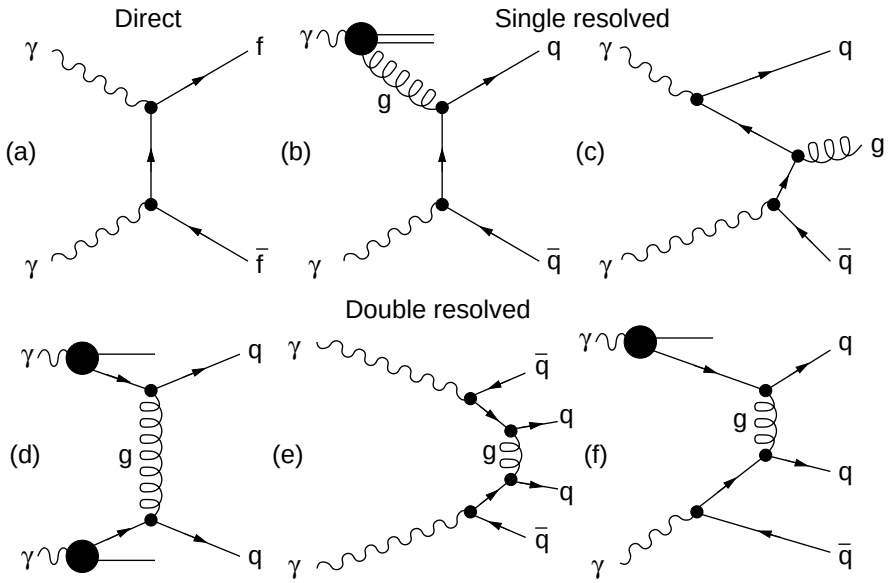

Figure 1.2: Types of photon–photon interactions. Direct (a); Single resolved: VMD × direct (b), anomalous × direct (c); Double resolved: VMD × VMD (d), anomalous × anomalous (e), VMD × anomalous (f).

1.2 Photon–photon interactions

The photon–photon reactions are usually classified based on the kind of objects that take part in the hard/primary interaction. This kind of classification can be seen in Figure 1.2, showing the following classes of interactions:

- In Figure 1.2 (a) the two photons interact directly through a virtual fermion[3]. Such interactions are called *direct* interactions.
- Figure 1.2 (b) and (c) show one of the photons fluctuating into an anomalous or hadronic state and interacting with the other photon through a virtual fermion. These are called *single resolved* interactions.
- In Figure 1.2 (d), (e) and (f) both photons take part in the interaction in a resolved state. These interactions are called *double resolved* interactions.

In theoretical calculations these cases have to be handled separately. It is possible to separate the contributions of the different types of processes in certain types of final states, which makes it possible to study the theory's description of a certain interaction channel more precisely.

[3]A particle is called virtual, if its properties fulfil $E^2 - \vec{p}^2 \neq m^2$.

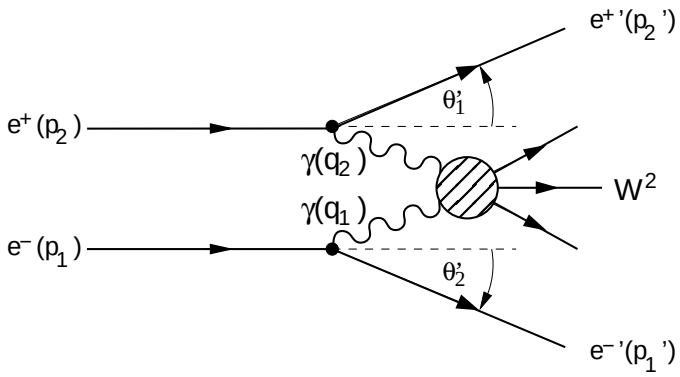

Figure 1.3: Schematic view of photon–photon interactions at LEP.

1.3 Interaction kinematics

At the LEP ring, photon–photon interactions could be studied in the following process:

$$e^+e^- \to e^+e^-\gamma^*\gamma^* \to e^+e^-X, \tag{1.3}$$

where the electrons each emit a virtual photon, which produce an X final state, while the electrons leave the interaction without being annihilated. A schematic view of this process can be seen in Figure 1.3

The spectrum of the photons which possess the y fraction of the electron beam energy, can be calculated using the Equivalent Photon Approximation (EPA) [2]:

$$f_{\gamma/e}(y, Q^2) = \frac{\alpha_{\rm em}}{2\pi Q^2}\left[\frac{1+(1-y)^2}{y} - \frac{2m_e^2 y}{Q^2}\right], \tag{1.4}$$

where $\alpha_{\rm em}$ is the electromagnetic coupling constant, m_e is the mass of the electron, and $Q^2 = E^2 - \vec{p}^2$ is the virtuality of the photon. The integrated form of this formula – known as the Weizsäcker-Williams formula [3, 4] – can give the fraction of photons in a $[Q^2_{\rm min}, Q^2_{\rm max}]$ interval:

$$\begin{aligned} f_{\gamma/e}(y, Q^2_{\rm min}, Q^2_{\rm max}) = \frac{\alpha_{\rm em}}{2\pi}\,\frac{1+(1-y)^2}{y}\log\left(\frac{Q^2_{\rm max}}{Q^2_{\rm min}}\right) - \\ 2m_e^2 y\left(\frac{1}{Q^2_{\rm min}} - \frac{1}{Q^2_{\rm max}}\right). \end{aligned} \tag{1.5}$$

The kinematics of the $\gamma\gamma$ process [1] for our purposes at a given $\sqrt{s_{\rm ee}} = E_{\rm cm}$ centre of mass energy is described by the negative square of the four-

momenta carried by the photons ($i = 1, 2$), $Q_i^2 = -q_i^2$, and the invariant mass of the hadronic final state, $W^2 = s_{\gamma\gamma} = (q_1 + q_2)^2$. Particles in high energy physics are described by their four-momenta, which for a particle with a momentum of $\vec{p} = (p_x, p_y, p_z)$ and energy E, is written as:

$$\begin{pmatrix} q_0 \\ q_1 \\ q_2 \\ q_3 \end{pmatrix} \equiv \begin{pmatrix} -E \\ p_x \\ p_y \\ p_z \end{pmatrix} \tag{1.6}$$

1.4 Hadron showers

The hard processes in high-energy reactions often lead to the production of quarks and gluons (partons). At high energies the strong coupling constant becomes small, allowing the partons to interact directly. Because of the small value of the coupling constant, these interactions can be handled using perturbative calculations.

However as the produced partons are leaving each other and the distance between them grows, the coupling constant increases. At a certain distance it becomes large enough to produce dozens of new partons. Finally these quarks and gluons form "colourless" hadrons which we can observe. This last step of the interaction – called hadronisation or fragmentation – results in collimated hadron showers called jets.

The hadronisation process cannot be calculated analytically, as perturbative calculations can not be performed for large coupling constants. It can only be simulated using certain types of models. These models, however, can only be tested together with the model describing the hard process between the interacting partons, which makes their validation non-trivial.

CHAPTER 2

LEP and OPAL

In this chapter I describe the Large Electron Positron accelerator ring and one of its experiments, the OPAL detector.

2.1 The Large Electron Positron collider

The Large Electron Positron collider (LEP) was an e^+e^- storage ring built at CERN, in Geneva, Switzerland. It had a circumference of 27 km and was located underground at depths of approximately 100 m. It started operation in 1989 and until 1995 was used to collide electron and positron beams at a centre of mass energy close to the Z^0 mass (at about 90 GeV). This period is now called LEP1. LEP2 running started in 1996 with the gradual increase of the centre of mass energy of the electron beams from 161 GeV to 209 GeV by the end of 2000.

LEP was designed for precision measurements of the Standard Model quantities and for searches for *New Physics*[1]. Two-photon physics became important in the LEP2 running, as at these high energies large statistics could be collected from photon–photon events.

The layout of the CERN accelerator complex that provided LEP with electron and positron beams can be seen in Figure 2.1.

2.1.1 Electron and positron beams at LEP

LEP relied on the pre-existing Proton Synchrotron (PS) and Super Proton Synchrotron (SPS) rings to pre-accelerate the electron and positron beams before they were injected in the LEP ring for the final step of the acceleration. The electron and positron beams were generated in the following way:

[1] The thesis refers to physics not covered by the Standard Model of Particle Physics, as *New Physics*.

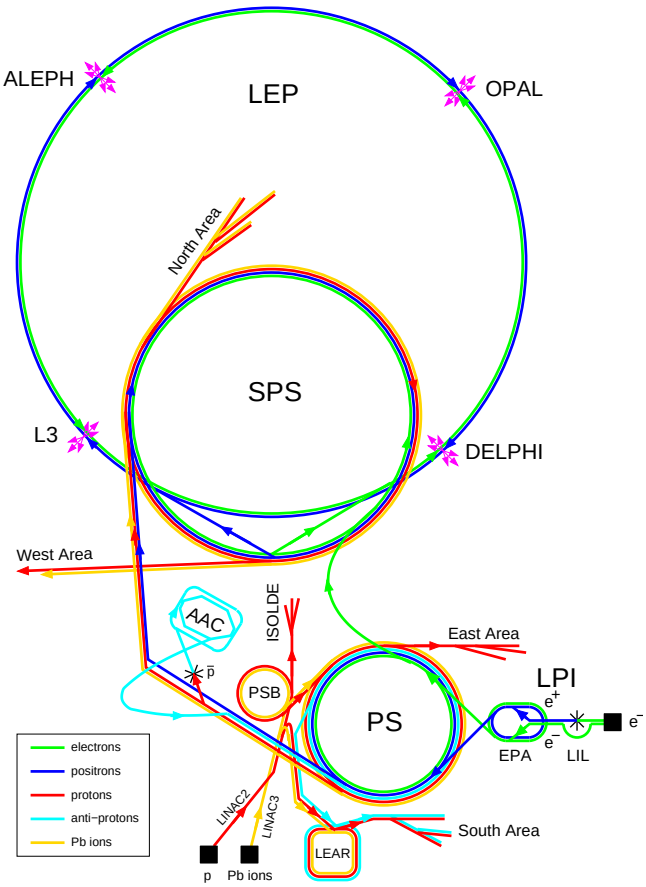

Figure 2.1: Schematic view of the CERN accelerator complex servicing LEP. (Status of 1996.) Description of the individual parts can be found in Section 2.1.1.

1. an electron gun was used to create bunches of electrons at a rate of about 100 Hz;

2. the electrons were accelerated to 600 MeV in the LEP Injector Linac (LIL). Some electron bunches were used to produce positrons via Bremsstrahlung and pair production on a fixed target. The positrons were then also accelerated to 600 MeV using LIL;

3. the Electron Positron Accumulator (EPA) was used to collect the electrons and positrons into 4 or more bunches;

4. from EPA, the electrons and positrons were injected into the PS and accelerated to 3.5 GeV;

5. the bunches were then fed into the SPS where the final pre-acceleration of the electrons and positrons took place, accelerating the bunches to 20 GeV;

6. finally the beams were injected into the LEP ring where they were accelerated to the desired energy (45 – 104 GeV), and brought to collision at the centre of the 4 main experiments.

It took about 15 – 30 minutes to fill LEP with $\sim 5{\times}10^9$ electrons and positrons, repeating this sequence. A fill lasted for about 15 hours in LEP1 and 4 – 5 hours in LEP2 before the luminosity of the beam decreased to the point that the ring had to be filled up again.

2.1.2 Beam luminosity

The beam luminosity is defined as

$$\mathcal{L} = \frac{N_1 \cdot N_2 \cdot n_\mathrm{b} \cdot f_\mathrm{rev}}{A}, \tag{2.1}$$

where $N_{1,2}$ are the number of electrons in the colliding bunches, n_b is the number of bunches, f_rev is the revolution frequency, and A is the interaction cross section of the colliding beams.

The luminosity received by the experiments was measured by counting low-angle Bhabha scattering events. These are events where the electron and positron scatter elastically into the detector and are characterised by two high energy back-to-back electromagnetic clusters with no other recorded activity in the detector. The cross section of this process (σ_Bhabha) is very well known [5,6] and is large at small polar angles, so the simple formula of

$$\mathcal{L} = \frac{N_\mathrm{Bhabha}}{\sigma_\mathrm{Bhabha}} \tag{2.2}$$

could be used to calculate the recorded luminosity with a very good precision.

2.2 Omni Purpose Apparatus for LEP

OPAL [7] was one of the four detectors built for the LEP accelerator. It was a general purpose detector designed to study a wide variety of interactions occurring in e^+e^- collisions. It was first used in 1989, and with some upgrades it was in operation until the closure of LEP at the end of 2000.

A cut away diagram showing the components of OPAL can be seen in Figure 2.2. The main types of sub-detectors were:

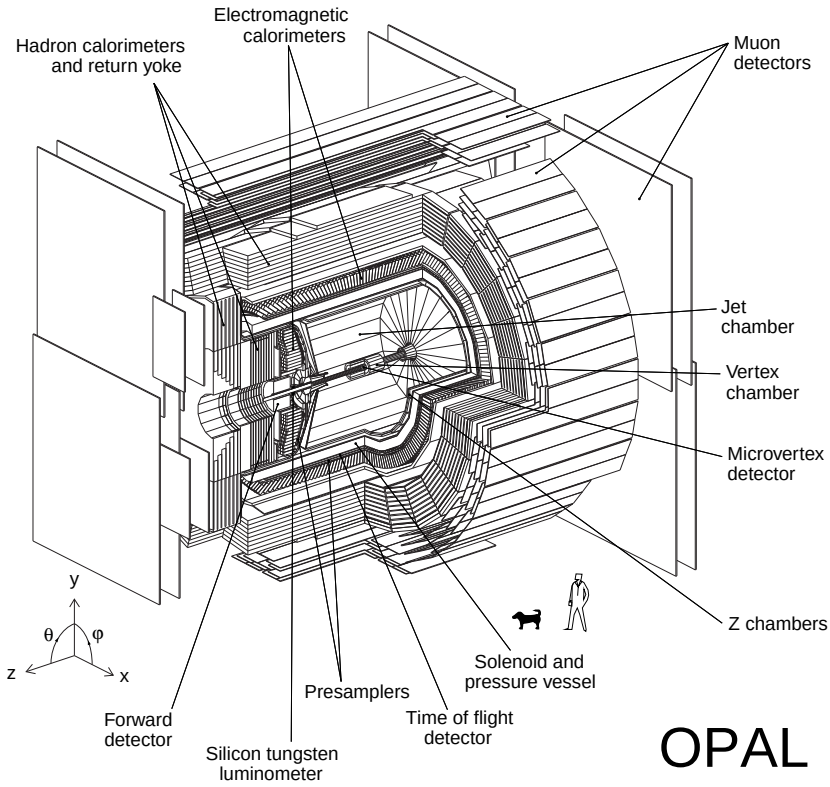

Figure 2.2: Cut away diagram showing the components of OPAL.

- Vertex and tracking detectors to record the tracks of charged particles in the central region, provide dE/dx information on the tracks for particle identification and reconstruct primary and secondary vertices of an event.
- Electromagnetic calorimeter for the energy measurement of electrons and photons.
- Hadronic calorimeter for the energy measurement of hadrons.
- Muon detectors for the identification and reconstruction of muon tracks.
- Forward detectors used mainly as luminosity monitors and for the detection of scattered electrons from non-elastic scattering events.

The thesis uses the standard OPAL coordinate system, which is a right-handed coordinate system where the z-axis points in the direction of the e^--beam and the x-axis points to the centre of the LEP ring. The polar angle θ and the azimuthal angle ϕ are defined relative to the $+z$-axis and $+x$-axis,

respectively. In cylindrical polar coordinates, the radial coordinate is denoted r. The transverse momentum is defined as a component of the momentum perpendicular to the z-axis. The pseudo-rapidity, η, is defined as

$$\eta = -\ln\left[\tan\left(\frac{\theta}{2}\right)\right]. \tag{2.3}$$

Pseudo-rapidity is preferred in particle collider experiments to describe the polar direction of particles coming from the interactions instead of the polar angle, θ, as the observed total particle production cross section is flat in η. The relation between θ and η is demonstrated in Figure 2.3.

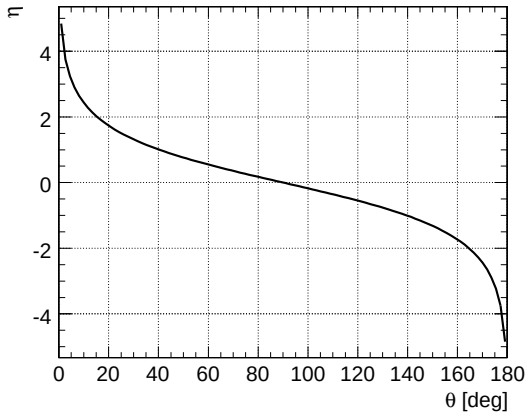

Figure 2.3: Relation between the polar angle measured from the beam axis, and the pseudo-rapidity calculated from the polar angle, following Equation 2.3.

Figure 2.4 shows a cross section view of the detector in planes perpendicular and parallel to the beam axis. The central tracking chambers were contained inside a solenoid that provided a uniform magnetic field of 0.435 T. Going from inside out, the solenoidal magnet coil was surrounded by time-of-flight counters, a lead glass electromagnetic calorimeter with a presampler, a hadron calorimeter constructed by instrumenting the magnet return yoke and four layers of outer muon chambers. In the following I give more details about the detector parts that were actively used in the analysis presented in Chapter 3.

2.2.1 The tracking detectors

The central tracking system was composed of three main elements: a high resolution vertex detector, a "jet chamber" type drift chamber and the z-chambers. The chambers are shown in Figures 2.2 and 2.4 together with the other parts of

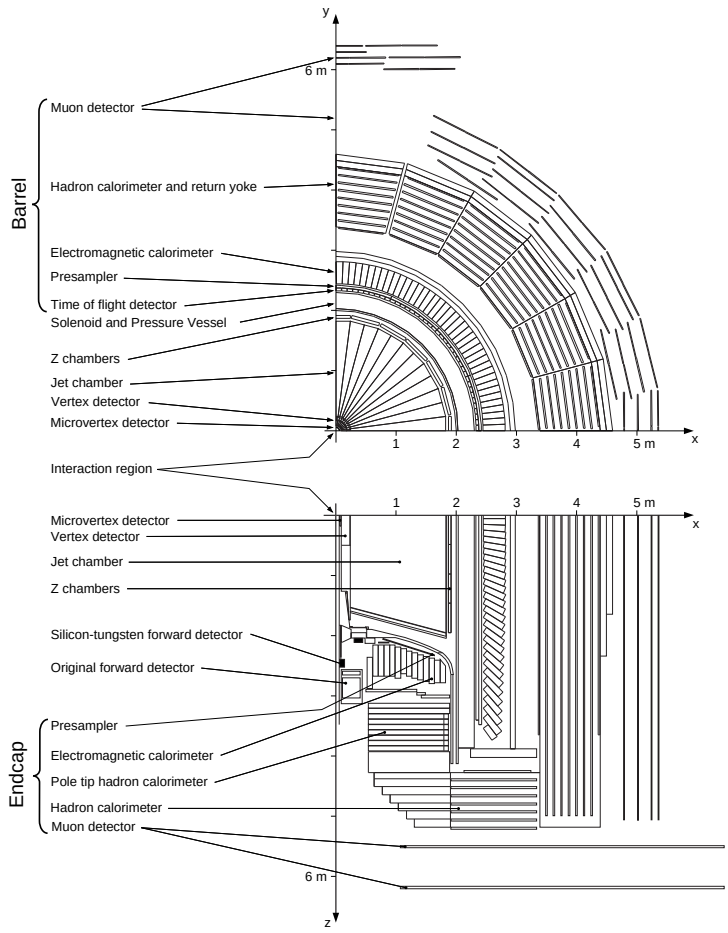

Figure 2.4: Cross sections of OPAL parallel and perpendicular to the beam axis.

the detector. The vertex detector was located between the beam pipe and the jet chamber. It was used to reconstruct the decay vertices and to improve the charged track momentum resolution. The jet chamber recorded the charged particle tracks over almost the entire solid angle and measured their momenta. The z-chambers were used to obtain a precise measurement on the z coordinate of the charged tracks, thereby improving on the invariant mass reconstruction precision. The performances of the various tracking detectors are detailed in the following.

The vertex detector

Originally the vertex detector was the innermost component of OPAL. It was a 1 metre long, 470 mm diameter, cylindrical drift chamber surrounding the

carbon fibre beam pipe. It operated within the common 4 bar central tracking system pressure vessel. The chamber consisted of an inner layer of 36 cells with axial wires and an outer layer of 36 small angle stereo cells.

In 1991 a silicon micro-vertex detector was installed in the centre of the detector, around the 5.35 cm radius beam-pipe. It consisted of two concentric cylinders with 6.1 and 7.8 cm radius built from silicon microstrip detectors.

The micro-vertex detector provided a position measurement in the $r-\phi$ plane with $\sigma = 5$ μm precision and $\sigma = 13$ μm along the z axis. The axial cells of the vertex detector provided position measurements in the $r-\phi$ plane with a precision of $\sigma = 50$ μm, while maintaining a good multi-hit detection capability to resolve individual particles within jets. A coarse measurement of the z-coordinate (along the wires) was possible by measuring the time difference between the signals on the two ends of the anode wires. This information was used both in the fast track trigger, and in offline track finding.

The jet chamber

The jet chamber was designed to provide good spatial resolution for jet-like events, with the possibility of particle identification, within almost the full 4π solid angle. The sensitive volume of the jet chamber was a cylinder with a length of about 4 m, surrounding the vertex detector. Its inner- and outer diameters were 0.5 and 3.7 m, respectively. It was subdivided into 24 identical sectors, each containing a plane with 159 sense wires. The maximum drift distance varied from 3 cm at the innermost wires to 25 cm at the outermost wires.

159 points could be measured along each track in the $43° < \theta < 137°$ range, and at least 8 points could be obtained for a track over a solid angle of 98% of 4π. For each point true three-dimensional coordinates (r, ϕ, z) could be measured from the wire position, drift time and the charge division. The charge division method required the measurement of the integrated charges for each hit at both ends of the signal wires. The ratio of these charges were used to determine the z position of the hit, and the sum were used to calculate the dE/dx energy loss of the particles in the chamber gas for particle identification.

The average spatial resolutions of the jet chamber were $\sigma_{r-\phi} = 135$ μm and $\sigma_z = 6$ cm at a mean drift distance of 7 cm.

The z-chambers

The z-chambers were arranged as a barrel around the jet chamber. They covered the polar angle from 44° to 136° and 94% of the azimuthal angle. They provided precise measurements of the z coordinates of the charged particles as they left the jet chamber. This resulted in an improvement in both the polar

angle and invariant mass measurements.

They consisted of 24 drift chambers, which were 4 m long, 50 cm wide and 59 mm thick each. The chambers were divided such that the maximum drift distance was about 25 cm in the z direction. It had an absolute z resolution of around $\sigma_z = 300$ μm. Its $r - \phi$ resolution was on the order of 1.5 cm.

Performance

The momentum of charged particles could be reconstructed based on the radius of their tracks in the magnetic field generated by the central solenoid. If a track traversed each tracking detector, the relative uncertainty of the momentum measurement was:

$$\frac{\sigma_p}{p} = \sqrt{0.02^2 + (0.0015 \cdot p[\mathrm{GeV/c}])^2}. \tag{2.4}$$

This means that the $p = 2$ GeV/c measured momentum of a charged track had a 2% uncertainty.

2.2.2 The electromagnetic calorimeter

The electromagnetic calorimeter was used to detect and measure the energies of electrons and photons ranging from a few tens of MeV to about 100 GeV. It was a total absorption Cherenkov calorimeter. As shown in Figures 2.2 and 2.4, it was mounted between the coil and the iron yoke of the solenoid magnet. It consisted of three separate assemblies of lead glass blocks: a barrel surrounding the magnet coil, and two end-caps. Together they covered 98% of the solid angle.

As there was about $2X_0$ of material[2] in front of the calorimeter (mostly due to the magnet coil and pressure vessel), most electromagnetic showers were initiated before the lead glass itself. For this reason presampling devices were installed immediately in front of the lead glass both in the barrel and end-cap regions to measure the positions and sample energies of these electromagnetic showers. The presamplers improved both the π^0-photon and electron-hadron discrimination and the electromagnetic energy resolution. The pulse height in the presampler was approximately proportional to the number of minimum ionising particles (pions) entering the device, which itself was proportional to the energy deposited in the material in front of the presampler. This meant that the energy resolution could be improved using the information from the presamplers.

[2]Radiation length is commonly denoted as X_0 in this thesis. X_0 is the amount of material that a charged particle traverses before losing all but $1/e$ of its total energy in electromagnetic interactions.

Barrel electromagnetic calorimeter

The barrel part of the electromagnetic calorimeter consisted of a cylindrical array of 9440 lead glass blocks of 24.6 X_0 length. It covered the full azimuthal angle and $|\cos\theta| < 0.82$. It was instrumented with magnetic field tolerant phototubes. The longitudinal axes of the lead glass blocks pointed towards the interaction point in the middle of the detector to minimise the probability of a single particle to deposit energy in more than one block. However the blocks were slightly tilted from the perfect pointing geometry to prevent neutral particles (especially photons) from escaping the calorimeter in the gaps between the lead glass blocks.

End-cap electromagnetic calorimeter

The end-cap part of the electromagnetic calorimeter consisted of two "dome-shaped" arrays, each built from 1132 lead glass blocks. They covered the full azimuthal angle and $0.81 < |\cos\theta| < 0.98$. Here the lead glass blocks were mounted with their axes coaxial with the beam line, mainly because of geometrical constraints. The glass blocks were instrumented with special, single stage multipliers known as vacuum photo triodes (VPTs) that could operate in the full axial field of the detector magnet.

Performance

The typical energy resolution of the calorimeter, without any additional material in front of it, was:

$$\frac{\sigma_E}{E} \approx 0.2\% + \frac{6.3\%}{\sqrt{E[\mathrm{GeV}]}}. \tag{2.5}$$

However adding 2.08 X_0 material in front of the detector degraded this resolution substantially, by about a factor of 2 at 6 GeV. But using the information from the presamplers, ∼50% of this degradation could be recovered.

2.2.3 The hadron calorimeter

The hadron calorimeter was used to measure the energy and rough position of hadrons leaving the electromagnetic calorimeter and to assist in the identification of muons. It used the iron of the magnet return yoke as absorber, as that provided 4 or more interaction lengths[3], λ, of absorber material over 97% of the solid angle.

[3]The mean free path travelled by a hadron before it enters a non-elastic interaction is denoted by λ.

The yoke was segmented into multiple layers, with detector planes between each layer. These formed a cylindrical sampling calorimeter that was about 1 m thick. Its energy resolution was mainly limited by the material in front of the calorimeter (mostly the material of the electromagnetic calorimeter), and by the structure of the return yoke itself. It was constructed in three parts: the barrel, the end-caps and the pole tips.

Barrel and end-cap hadron calorimeter

The barrel consisted of 9 layers of detector chambers, separated by 8 iron slabs. Its inner and outer radii were 3.39 m and 4.39 m, respectively. The slabs were 100 mm thick with 25 mm gaps between them. The calorimeter was closed on both ends by doughnut-shaped end-caps. The end-caps had 8 layers of detector chambers alternating with 7 slabs of iron. The slabs were also 100 mm thick in the end-cap, but were separated by 35 mm gaps. Since there was a high probability for the hadrons to interact with the detector material before reaching the hadron calorimeter[4], the overall hadronic energy had to be determined by combining the signals from the electromagnetic and hadron calorimeters.

Pole tip hadron calorimeter

This part of the detector extended the solid angle coverage of the hadron calorimeter from $|\cos\theta| < 0.91$ to 0.99. The gaps between the iron plates – available for the detectors – were reduced to 10 mm, to minimise the perturbation of the magnetic field. The energy resolution of the central detector was falling off in this direction. To compensate for this, the number of samplings was increased to 10.

Performance

The barrel and end-cap parts of the calorimeter had similar energy resolutions. Their energy resolution for 10 GeV particles was found to be:

$$\frac{\sigma_E}{E} \approx \frac{120\%}{\sqrt{E[\mathrm{GeV}]}} \tag{2.6}$$

The pole tip calorimeter had slightly better resolution at energies below approximately 15 GeV ($100\%/\sqrt{E}$), which deteriorated for higher energies. The energy resolution of the combined detector varied from $100\%/\sqrt{E}$ for energies below 15 GeV to about $140\%/\sqrt{E}$ at 50 GeV.

[4]The tracking detectors and the electromagnetic calorimeter accounted for $\sim$2.2 λ.

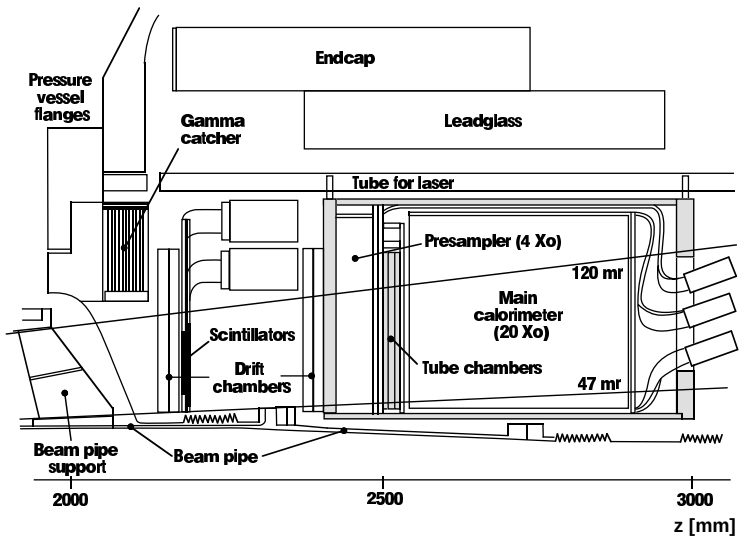

Figure 2.5: The structure of the forward detector.

2.2.4 The forward detectors

The main purpose of the forward (FD) detectors was to measure the luminosity of LEP by detecting the electrons from small-angle Bhabha scattering, and to tag electrons from $\gamma\gamma$ interactions. They were placed at either ends of the detector to measure very low angle particles with respect to the beam line. There were multiple separate parts of the forward detector: the gamma catcher, drift chambers, fine luminosity monitor counters, the main calorimeter and the tube chambers. Their layout is shown in Figure 2.5.

It had a clean acceptance for particles from the interaction point between 47 and 120 mrad from the beam line. Its various parts, from which information was used in the analysis, are described below.

Main calorimeter

The forward calorimeter was composed as a lead-scintillator sandwich with 35 layers, which accounted for about $24X_0$. Its energy resolution for Bhabha events was $\sigma_E/E \approx 17\%/\sqrt{E[\mathrm{GeV}]}$, with its response being linear with energy and uniform between segments.

Tube chambers

Between the presampler and the main section of the calorimeter, there were three planes of brass-walled proportional tube chambers. Their main purpose was to detect the positions of individual showers. The uncertainty of this

measurement was mainly limited by the shower fluctuations after traversing $4X_0$ of material in the presampler, and was about ± 3 mm.

Drift chambers

Drift chambers were placed in two planes before the main calorimeter to measure the locations of particles entering the forward detector, with high accuracy. Their resolution was 300 μm in the drift direction and 1 mm along the sense wires.

Gamma catcher

The gamma catcher was a ring of lead–scintillator sandwich modules with a thickness of $7X_0$. It could detect electrons or gamma rays with more than 2 GeV energy, giving a veto on background events for the neutrino counting channel $e^+e^- \to Z^0\gamma$, with $Z^0 \to \nu\bar{\nu}$.

Performance

The energy resolution of the full system, combining the signals of all parts, for electromagnetic showers, was

$$\frac{\sigma_E}{E} \approx \frac{18\%}{\sqrt{E[\mathrm{GeV}]}}. \tag{2.7}$$

Its hadron energy measurement was much less precise, the combined resolution was $\sigma_E/E \approx 90\%/\sqrt{E[\mathrm{GeV}]}$.

2.2.5 The silicon-tungsten calorimeter

The silicon-tungsten (SW) detectors were placed on either ends of the detector, 239 cm from the interaction point, between the beam pipe and the forward detector. It was installed in 1993 to give an improvement on the luminosity measurement. They were sampling calorimeters that consisted of 19 layers of sampling silicon separated by 18 layers of tungsten. They covered the 33-59 mrad polar angle region in practically the full azimuth angle. Their energy resolution for electromagnetic showers was $\sigma_E/E \approx 25\%/\sqrt{E[\mathrm{GeV}]}$, and had a spatial resolution of about 10 μm.

2.2.6 The OPAL trigger system

The OPAL trigger decision was based on the signals of most of the detectors discussed previously – comprising a "track trigger", a time-of-flight trigger, electromagnetic calorimeter, hadron calorimeter and muon triggers. With four

electron bunches circulating the LEP ring, the bunch-crossing interval was 22 μs. The chamber drift times were up to 8 μs and electronics reset times up to 7 μs. They left several microseconds for sophisticated triggering. Since the readout deadtime of OPAL was about 20 ms per event, the trigger rate had to be kept below 5 Hz in order to keep losses below 10%.

The OPAL trigger system [8] was implemented in separate parts – the various sub-detector signals were formed independently and were combined to give an overall trigger signal by the "central trigger logic" processor. There were two kinds of sub-detector trigger signals. First, "direct" trigger signals, such as total observed energy or track multiplicities were created from information from a single detector component and had relatively high thresholds to keep their rates low. To allow lower thresholds for final state particles, the sub-detectors were divided into θ and ϕ elements (the "θ-ϕ matrix") requiring spatial coincidences between the components. The full azimuthal range was covered by 24 bins, and the polar angle by 6 bins. This gave a total of 144 θ-ϕ bins. The matrix had five "layers" corresponding to the track, time-of-flight, electromagnetic, hadron and muon triggers.

In the following I describe the triggers that were efficient for selecting the events analysed in Chapter 3.

The track trigger

The track trigger used information from the 12 axial wires of each sector of the vertex detector and from three groups of 12 adjacent wires at different radii of each jet chamber sector. Signals formed by the vertex detector and jet chamber trigger electronics were combined by the track trigger processor. It detected the presence of tracks in any bins of the θ-ϕ matrix and provided various track multiplicity signals. In addition, simple counts of the number of hit wires were provided, and also trigger signals depending on the specific ionisation of particles were available from the jet chamber electronics.

The track trigger was designed to be flexible, with all parts of the decision making being programmable. It was possible to run the track trigger with a required track multiplicity of 2-3 at a sustainable rate. Such a trigger item was found to be 98.5% efficient for selecting $e^+e^- \to \mu^+\mu^-$ events.

The electromagnetic calorimeter trigger

The trigger logic for the electromagnetic calorimeter was as follows. Several analogue energy sums were provided for different segmentations of the calorimeter, for instance sums over the total barrel, over each end-cap and over each of the 144 θ-ϕ cells. Each energy sum was discriminated at two thresholds, a "high" and a "low" threshold.

There were a number of direct trigger inputs sent from the electromagnetic calorimeter to the central trigger logic. The total energy sum trigger could be sustained by requiring a total observed energy on the order of 10 GeV in the electromagnetic calorimeter.

The hadron calorimeter trigger

The hadron calorimeter was divided into 92 bins in the θ-ϕ plane. Separate analogue sums were measured for each of these bins, discriminating them at three different thresholds. The 92 bins were matched by the trigger electronics onto the 144 overlapping bins of the θ-ϕ matrix, to give input to the combined triggers.

The hadron calorimeter trigger could also be operated with requiring total energy sums of around 10 GeV.

Performance

Single particle triggers from only one detector were not possible due to too high trigger rates, except for the single cluster trigger in the electromagnetic calorimeters that could be operated with thresholds < 10 GeV. Signals requiring only one hit in a detector layer were running at high rates due to various backgrounds, but the θ-ϕ coincidences between layers had low rates, even for low calorimeter thresholds, as the coincidences suppressed random noise and low energy background seen in only one detector layer.

The trigger efficiency for a few physics channels are summarised in Table 2.1 [8]. As can be seen, the trigger efficiency for final states with considerable activity in the detector was practically 100%.

Physics channel	$\lvert\cos\theta\rvert$	Efficiency [%]
$e^+e^- \rightarrow$ hadrons	< 1.0	100
$e^+e^- \rightarrow \mu^+\mu^-$	< 0.95	99.9 ± 0.1
$e^+e^- \rightarrow \tau^+\tau^-$	< 0.90	99.9 ± 0.1
$e^+e^- \rightarrow e^+e^-$	< 0.85	100
$e^+e^- \rightarrow \gamma\gamma$	< 0.90	> 99.9
small angle Bhabha	0.989 - 0.999	> 99.9

Table 2.1: Overall OPAL trigger efficiencies for various standard physics channels. The efficiencies for each physics channel are relative to the particular selection cuts of the analysis [8, 9].

CHAPTER 3

Inclusive jet production in photon–photon collisions

As shown in Chapter 1, comparing the inclusive jet production cross section from photon–photon interactions with theoretical predictions, is a good way to test our models for the description of the resolved photon, the perturbative calculation of the hard scatter, and for the hadronisation of the produced partons.

For this reason, a study measuring this quantity has been published previously by the OPAL collaboration [10], where the inclusive jet production cross section was measured for centre of mass energies from 130 to 136 GeV, with a cone jet finding algorithm, and found to agree well with QCD calculations. Recently the L3 collaboration published a study at higher beam energies [11], that measured a jet production cross section significantly larger than the prediction for high $p_{\mathrm{T}}^{\mathrm{jet}}$, shown in Figure 3.1.

The aim of the study presented here was to extend the energy range of the measurement on the inclusive jet production cross section presented in [10] to 189 – 209 GeV and to a significantly larger integrated luminosity, thereby covering also the phase space used in [11].

3.1 Monte Carlo simulation

All signal and background Monte Carlo samples used for detector corrections and background determinations were passed through a full simulation of the OPAL detector [12]. They were analysed using the same reconstruction algorithms as were applied to the data.

The Monte Carlo generator PYTHIA 5.722 [13–15] was used to simulate the signal processes (photons with low virtuality producing final states with partons) for the determination of detector corrections, as large samples with full detector simulation and reconstruction were available. For all other purposes

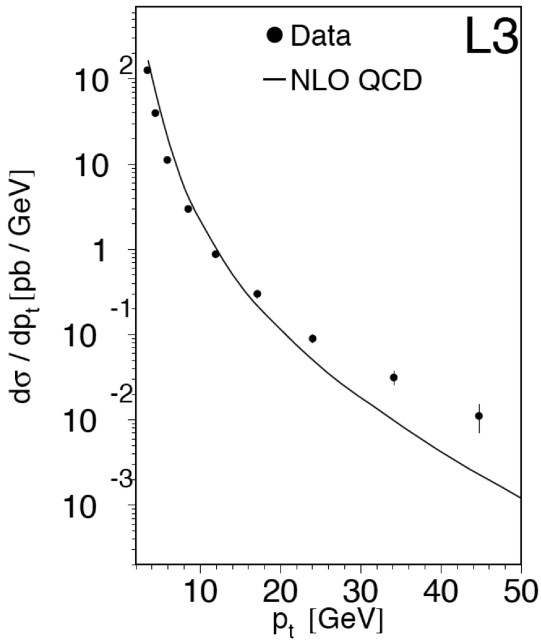

Figure 3.1: The inclusive jet production cross section presented by the L3 collaboration in [11].

the more modern PYTHIA 6.221 was used to generate the samples. PYTHIA is based on leading order QCD matrix elements for massless quarks with the addition of parton showers and hadronisation.

The following generators were used for the simulation of the six background processes that contribute significantly after the event selection described later in the chapter:

- PYTHIA for $Z^0/\gamma^* \to \mathrm{q\bar{q}}$ and $\mathrm{e^+e^-} \to W^+W^-$,
- BDK [16–19] for $\gamma\gamma \to \tau^+\tau^-$,
- HERWIG [20,21] for deep-inelastic electron-photon scattering ($\gamma^*\gamma$),
- KORALZ [22] for $Z^0 \to \tau^+\tau^-$, and
- GRC4F [23] for $\mathrm{e^+e^-} \to \mathrm{e^+e^-q\bar{q}}$

3.2 Event selection

We have studied the inclusive production of jets in collisions of two quasi real photons at $\mathrm{e^+e^-}$ centre of mass energies, $\sqrt{s_{\mathrm{ee}}}$, from 189 to 209 GeV, with a

total integrated luminosity of 593 pb^{-1} of data collected by the OPAL detector. For the purpose of this analysis, the difference between the data taken at the various values of $\sqrt{s_{\mathrm{ee}}}$ is small and therefore the distributions for all energies have been added up. The luminosity-weighted average centre of mass energy is 198.5 GeV.

At these centre of mass energies, events having a low-p_{T} jet are dominated by two-photon interactions. This makes the selection of two-photon events with a jet having $p_{\mathrm{T}}^{\mathrm{jet}} < 10$ GeV rather easy. However events having jets with $p_{\mathrm{T}}^{\mathrm{jet}} > 20$ GeV are very strongly dominated by $Z^0/\gamma^* \to q\bar{q}$ processes. For this reason special care must be taken when selecting two-photon events with energetic jets.

The event selection was performed in multiple steps. First a pre-selection was run on the data collected at $\sqrt{s_{\mathrm{ee}}}$ from 189 to 209 GeV and only the events passing this selection were processed later on in the analysis. This reduced the data set for further analysis to a more manageable size.

The final selection of the two-photon events was performed using maximum likelihood distribution functions trained on Monte Carlo events. Evaluating a few multi-variate event selection techniques, this selection method proved to be the most stable, providing much better signal to background ratio than a simple cut-based event selection.

3.2.1 Event kinematics

The properties of the two interacting photons ($i = 1, 2$) are described by their negative squared four-momenta, Q_i^2, and the invariant mass of the photon–photon system, W. Each Q_i^2 is related to the electron scattering angle, θ_i', relative to the beam axis by

$$Q_i^2 = -\left(p_i - p_i'\right)^2 \approx 2E_i E_i' \left(1 - \cos\theta_i'\right), \tag{3.1}$$

where p_i and p_i' are the four-momenta of the beam electrons and the scattered electrons respectively, and E_i and E_i' are their energies. The invariant mass of the photon–photon system is calculated from the reconstructed hadronic final state by

$$W^2 = \left(\sum_h E_h\right)^2 - \left(\sum_h p_h\right)^2, \tag{3.2}$$

where the summation iterates over all reconstructed hadrons.

To select only the photon–photon interactions where the virtuality of both photons is small, events with one or both scattered electrons detected (single-tagged or double-tagged events) are excluded from the analysis. Driven by the

angular acceptance of the forward (FD) and silicon-tungsten (SW) calorimeters, a value of $Q^2 = 4.5$ GeV^2 is used in the analysis as the maximum possible Q^2. The median Q^2 resulting from this limit cannot be determined from data, since the scattered electrons are not tagged, but is predicted by the Monte Carlo simulations to be of the order of $\langle Q^2 \rangle = 10^{-4}$ GeV^2.

3.2.2 Jet reconstruction

In the analysis, a sum over all particles in the event or in a jet means a sum over two kinds of reconstructed objects: tracks satisfying the quality cuts detailed below, and all calorimeter clusters, including the ones in the forward calorimeters.

A track is required to have a minimum transverse momentum of 120 MeV and at least 20 hits in the central jet chamber. The track's point of closest approach to the origin must have a distance of less than 25 cm in z and a radial distance, d_0, of less than 2 cm from the z-axis for low-p_{T} tracks. In the analysis I have found that to ensure a good momentum measurement for high-p_{T} tracks having a transverse momentum larger than 5 GeV, I had to require a d_0 distance of less than 0.15 cm.

Calorimeter clusters had to pass an energy threshold of 100 MeV in the barrel section or 250 MeV in the end-cap section of the electromagnetic calorimeter, 600 MeV for the barrel and end-cap sections of the hadronic calorimeter, 1 GeV for the FD, and 2 GeV for the SW calorimeters. An algorithm is applied to avoid the double-counting of particles in the central tracking system and the calorimeters [10].

The measured hadronic final state for each event consists of all objects thus defined. Jets are formed from the reconstructed hadronic final state using the $\mathrm{k}_\perp$ jet algorithm [24]. In this algorithm the distance measure between any pair of objects i, j to be clustered is taken to be

$$d_{ij} = \min\left(p_{T,i}^2, p_{T,j}^2\right) \left(\frac{R_{ij}^2}{R_0^2}\right), \text{ with} \tag{3.3}$$

$$R_{ij}^2 = (\Delta\eta_{ij})^2 + (\Delta\phi_{ij})^2. \tag{3.4}$$

In the equations $p_{T,i}$, η_i and ϕ_i are the transverse momentum, pseudo-rapidity and azimuthal angle of the i-th particle, respectively. Throughout the analysis we set $R_0^2 = 1.0$.

d_{ij} is calculated for all object combinations, together with $d_i = p_{T,i}^2$ values for all objects. From this combined set, the minimum value, $d_{\min}$, is selected. If $d_{\min}$ is associated to an i, j object pair, the two objects are merged into a new object using the p_{T} recombination scheme. In this scheme the properties of the merged particles are computed as

$$p'_T = p_{T,i} + p_{T,j}, \tag{3.5}$$

$$\eta' = \frac{p_{T,i}\eta_i + p_{T,j}\eta_j}{p'_T}, \tag{3.6}$$

$$\phi' = \frac{p_{T,i}\phi_i + p_{T,j}\phi_j}{p'_T}. \tag{3.7}$$

If $d_{\min}$ is associated to a single object i, the object is added to the list of jets and removed from the clustering list.

3.2.3 Pre-selection

As a first step of the event selection, all data and Monte Carlo samples were pre-selected with the conditions explained in this section. The preselection criteria were as follows.

1. Using the $k_\perp$ jet algorithm, the event had to contain at least one reconstructed jet with pseudo-rapidity $|\eta^{\text{jet}}| < 1.5$ and a transverse momentum of $p_{\text{T}}^{\text{jet}} > 5$ GeV.

2. The total energy deposited in the electromagnetic and hadronic calorimeters had to be less than 80 GeV. This cut removes most of the hadronic Z^0 decays, including events with a radiative return to the Z^0 peak.

3. To remove events with scattered electrons in the FD and SW calorimeters, the total energy sum measured in the FD calorimeter had to be less than 55 GeV, and the total energy sum measured in the SW calorimeter had to be less than 40 GeV.

4. To reduce the background due to beam-gas interactions, the z position of the primary vertex was required to satisfy $|z| < 5$ cm and the net charge, Q_{el}, of the event – calculated from adding the charges of all reconstructed tracks – was required to be $|Q_{\text{el}}| < 5$.

5. The radial distance of the primary vertex from the beam axis had to be less than 3 cm to remove events originating from interactions between beam electrons and the beam-pipe.

In comparing the pre-selected events to Monte Carlo simulations, the signal Monte Carlo generator PYTHIA 5.722 underestimates the normalisation of the cross section by about 50%, and is scaled up accordingly. A similar deficiency was also observed in a previous study on di-jets [25]. Furthermore previous studies have shown that the prediction of Monte Carlo generators for

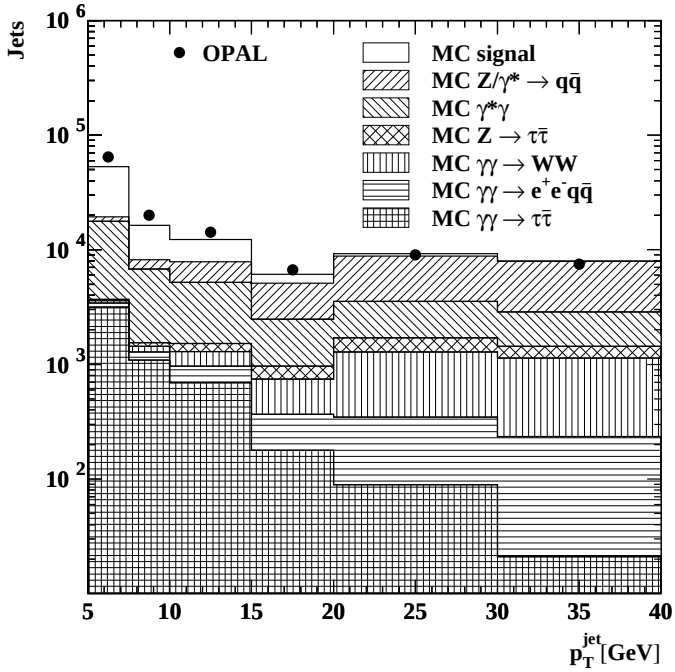

Figure 3.2: The $p_{\mathrm{T}}^{\mathrm{jet}}$ spectrum for all reconstructed jets with $|\eta^{\mathrm{jet}}| < 1.5$ after pre-selection. The signal MC and the contribution of the $\gamma^*\gamma$ have been scaled up as described in section 3.2.3.

jet events in photon–photon collisions, where one of the photons is strongly virtual, is too low by a factor of two [26,27]. The prediction of the contribution from $\gamma^*\gamma$ events has been scaled up accordingly, resulting in an adequate description of all quantities used in the analysis.

Events passing these pre-selection requirements were written out into event files much smaller than the original samples, making further processing of the data more simple. As it is demonstrated in Figure 3.2, the $p_{\mathrm{T}}^{\mathrm{jet}}$ spectrum after this pre-selection is dominated by background at high-$p_{\mathrm{T}}^{\mathrm{jet}}$. To suppress these backgrounds, an advanced event selection algorithm must be used.

3.2.4 Comparison of event selection methods

The method for selecting photon–photon interaction events had to be chosen early on in the analysis process. Three different kinds of event selection techniques were evaluated: selecting events by imposing simple cuts on event quantities; selecting events using an artificial neural network; and selecting

events using maximum likelihood distribution functions.

These event selection techniques require very different, long optimisation procedures. Because of this, the analysis was not completed using all of them, which would have provided a very good comparison of the overall usability of the event selection techniques. Instead the selection method was chosen based on the signal purity and selection efficiency they could provide with a simple optimisation of the technique. The event selection efficiency is defined as

$$\text{efficiency} = \frac{N_{\text{sel}}}{N_{\text{total}}}, \tag{3.8}$$

where N_{sel} and N_{total} mean the number of selected and total simulated Monte Carlo signal events. I define the signal purity as

$$\text{purity} = \frac{N_{\text{sig}}}{N_{\text{sig}} + N_{\text{bkgs}}}, \tag{3.9}$$

where N_{sig} and N_{bkgs} note the number of signal and background events remaining after the event selection, calculated from Monte Carlo.

I used the artificial neural network implemented in the NETTRA and NETGEN packages [28], which are based on the JETNET3 package [29]. These packages are written in FORTRAN, and were used mainly by the "b tagging" group of OPAL – the group responsible for identifying jets coming from the hadronisation of a b quark. To select events using maximum likelihood distribution functions, I used the software package detailed in the next section.

I will not give thorough details about the setup of the various event selection techniques here, just note that they were used with little optimisation for the comparison. This means that in the comparison I did not use the final optimisation of the selection presented in the next section. The results from the comparison can be seen in Figure 3.3. As can be seen, the likelihood based event selection method (Figure 3.3 (c)) provides by far the best signal purity, but with relatively low event selection efficiency. Raising the selection efficiency of this method to the level of the other two methods, still produced higher signal purities compared to them. For this reason, I made the decision of using maximum likelihood distribution functions for selecting photon–photon interaction events.

3.2.5 Selection using maximum likelihood distribution functions

The final event selection is based on maximum likelihood functions as implemented in the PC package [30] of the OPAL offline reconstruction software. It uses the Projection and Correlation Approximation (PCA) method to try to classify the events. As with most Multi-Variate Analysis (MVA) techniques,

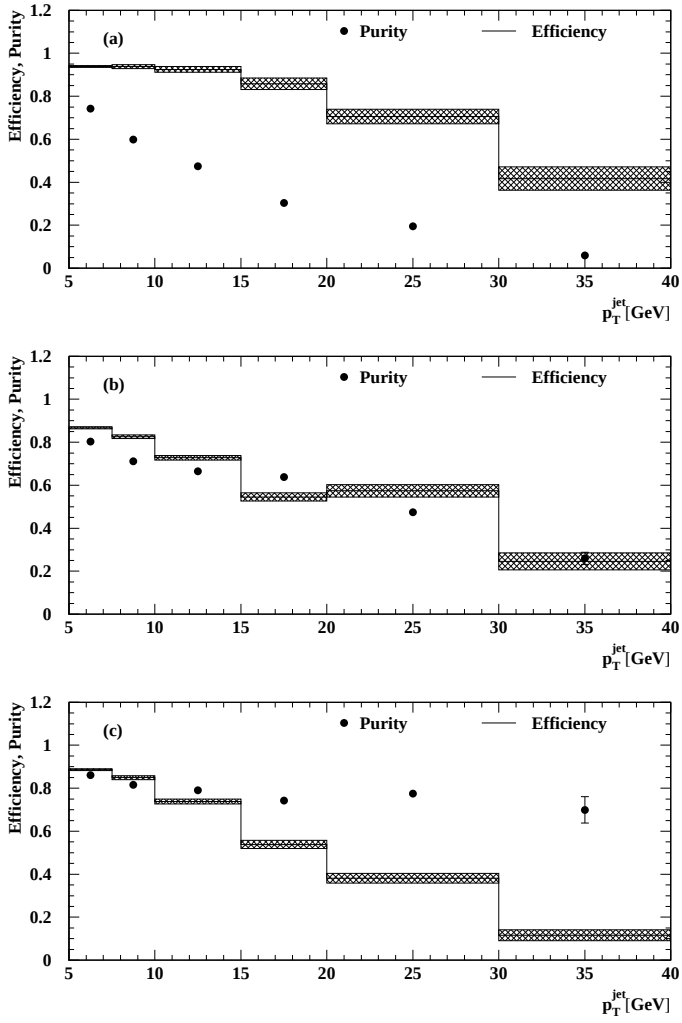

Figure 3.3: Comparison of different event selection methods. The efficiencies and purities of a cut-based (a), artificial neural network based (b), and maximum likelihood based (c) selection are shown as a function of $p_{\mathrm{T}}^{\mathrm{jet}}$.

one has to be careful when choosing the reconstructed variables that the selection algorithm can use in the classification, as providing the algorithm with too many, or too correlated parameters can result in a loss in selection efficiency/purity.

The selection algorithm requires hard limits on the values a variable can take. If in an event one of the selection variables lies outside of these limits, the event is automatically considered to be a background event.

The likelihood selection code implemented in the PC package is able to measure how well a given property of the event can differentiate between the event being signal or background. The code is also able to measure the correlation of the input variables during its training, and takes these correlations into account in the event selection. The impact of wrongly determining the correlations from the Monte Carlo samples was evaluated by artificially changing the correlation constants in the event selection, and was found to be negligible on the final results. The evaluation of a large number of selection variables resulted in the following seven being used by the likelihood function:

1. The visible invariant mass measured in the electromagnetic calorimeter only, W_{ECAL} (in the range [0–80] GeV);

2. The visible invariant mass calculated from the entire hadronic final state, W_{rec} (in the range [0–120] GeV);

3. The number of tracks (in the range [6–70]);

4. The sum of all energy deposits in the electromagnetic calorimeter, E_{ECAL} (in the range [0–80] GeV);

5. The sum of all energy deposits in the hadronic calorimeter, E_{HCAL} (in the range [0.1–55] GeV);

6. The missing transverse momentum of the event calculated from the measured hadronic final state (in the range from zero to $\sqrt{s_{\mathrm{ee}}}/2$);

7. To improve the rejection of background coming from hadronic Z^0 decays, an invariant mass, M_{J1H2}, is calculated from the jet with highest $p_{\mathrm{T}}^{\mathrm{jet}}$ in the event and the four-vector sum of all hadronic final state objects in the hemisphere opposite to the direction defined by this jet (considered in the range [0.1–100] GeV).

Figure 3.4 shows four examples of the distributions of the parameters used in the likelihood selection. The parameter space of the events was split into two parts for the event selection. The events were categorised into two groups depending on whether the jet with the highest energy in the event had a $p_{\mathrm{T}}^{\mathrm{jet}}$ larger or smaller than 30 GeV. The region of high $p_{\mathrm{T}}^{\mathrm{jet}}$, where most of the discrepancy with Next to Leading Order (NLO) QCD is observed in [11], is strongly affected by background from $Z^0/\gamma^* \to \mathrm{q\bar{q}}$ which is not important at lower $p_{\mathrm{T}}^{\mathrm{jet}}$. A separate optimisation of the selection is hence necessary to maximise the reach of the analysis in $p_{\mathrm{T}}^{\mathrm{jet}}$.

The output of the likelihood functions for the data and all simulated processes is shown in Figure 3.5. The cuts on the likelihood outputs are chosen

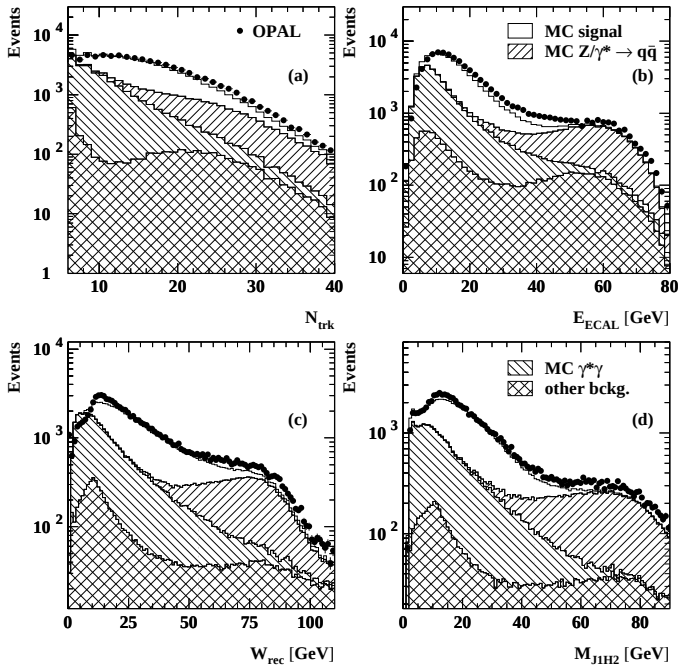

Figure 3.4: Example inputs to the likelihood functions: (a) the number of tracks in the event; (b) the total energy sum deposited in the ECAL; (c) the invariant mass reconstructed from the hadronic final state; and (d) the distribution of the M_{J1H2} variable. The signal MC and the contribution of the $\gamma^*\gamma$ have been scaled up as described in section 3.2.3.

to be $LH > 0.26$ and 0.98 for the low and high $p_{\mathrm{T}}^{\mathrm{jet}}$ region, respectively, as these cuts provided the best signal to background ratio with acceptable efficiency. Applying this cut in the low $p_{\mathrm{T}}^{\mathrm{jet}}$ region reduces the background by 91% while reducing the signal by 27%. Applying the cut in the high $p_{\mathrm{T}}^{\mathrm{jet}}$ region reduces the background by 99.5% while reducing the signal by 71%.

The $p_{\mathrm{T}}^{\mathrm{jet}}$ distribution after the full event selection is shown in Figure 3.6. The dominant background at low $p_{\mathrm{T}}^{\mathrm{jet}}$ is due to $\gamma^*\gamma$ events, while for high $p_{\mathrm{T}}^{\mathrm{jet}}$ the background is dominated by $Z^0/\gamma^* \to \mathrm{q\bar{q}}$ events.

As presented, the analysis uses strict cuts, requiring events to contain multiple high-p_{T} tracks. It has been shown previously that in this kinematical region the efficiency of the OPAL trigger is close to 100% [10] and thus the trigger was assumed to be fully efficient to select the events for the analysis.

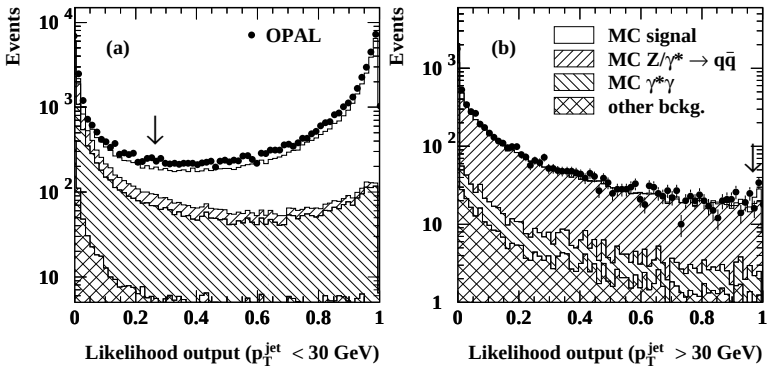

Figure 3.5: Outputs of the likelihood functions. Plots (a) and (b) show the output of the likelihood functions for events with $p_{\mathrm{T}}^{\mathrm{jet}} < 30$ GeV and $p_{\mathrm{T}}^{\mathrm{jet}} > 30$ GeV, respectively. The signal MC and the contribution of $\gamma^*\gamma$ have been scaled up as described in section 3.2.3.

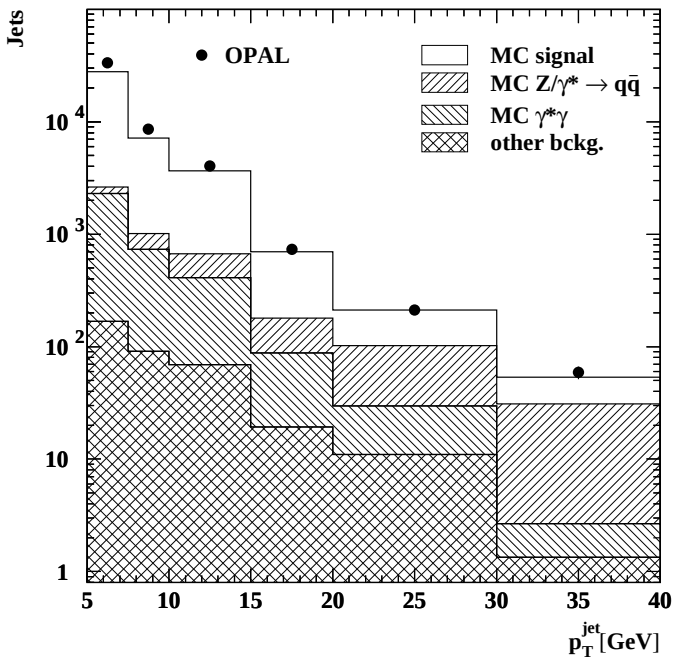

Figure 3.6: Number of jets in each $p_{\mathrm{T}}^{\mathrm{jet}}$ bin after the full event selection. The signal MC and the contribution of $\gamma^*\gamma$ have been scaled up as described in section 3.2.3.

3.3 Uncertainties and corrections

3.3.1 Systematic uncertainties

Besides having uncertainties in the cross section measurement from finite statistics, there are a number of effects responsible for adding systematic uncertainties to the results. The various uncertainties are calculated separately for each bin of the $p_{\mathrm{T}}^{\mathrm{jet}}$ spectrum, then added up in quadrature to calculate the total systematic uncertainty. The values for each bin were averaged with results from its two neighbours (single neighbour for endpoints) to reduce the effect of bin-to-bin fluctuations. The sources of systematic uncertainties considered are given below.

- The absolute energy scale of the electromagnetic calorimeter is known to about 3% [31] for the jet energy range in this analysis. To estimate the influence of this uncertainty, the energy scale of the data is varied by this amount, and the analysis is repeated.

- To assess the uncertainty associated with the subtraction of background events, all backgrounds – except for $\gamma^*\gamma$ – have been varied by 10%. The prediction of the contribution from $\gamma^*\gamma$ events has been scaled up by a factor of two, as described earlier. By comparing the Monte Carlo predictions to the data in regions where this background dominates, we concluded that this scaling factor cannot be varied by more than about 30% while keeping a good description of the data. The scaling factor is varied accordingly. The resulting uncertainty is dominated by the distributions from the $\gamma^*\gamma$ and $Z^0/\gamma^* \to \mathrm{q\bar{q}}$ backgrounds.

- To test the event selection's dependence on the simulation of the signal, the signal Monte Carlo has been re-weighted to have a $p_{\mathrm{T}}^{\mathrm{jet}}$-slope in which it significantly either over- or underestimates the data at high $p_{\mathrm{T}}^{\mathrm{jet}}$ and the analysis is repeated.

- The dependence on the event selection algorithm's configuration is tested by changing the cut on the likelihood output value down to $LH > 0.23$ and up to 0.29 for the low $p_{\mathrm{T}}^{\mathrm{jet}}$ region, and down to 0.88 for the high $p_{\mathrm{T}}^{\mathrm{jet}}$ region. Such $\pm 10\%$ variations are considered to give a conservative estimation on the uncertainty introduced by the selection procedure.

- The uncertainty on the determination of the integrated luminosity is much less than 1%, and is neglected.

The results for the uncertainties for each bin can be found in Table 3.1.

p_T^{jet} [GeV]	ECAL energy [%]	Backg. subtr. [%]	Cut selection [%]	Signal rew. [%]	Total [%]
5.0 – 7.5	3.2	4.4	0.1	2.6	6.0
7.5 – 10.0	3.5	4.6	0.2	2.2	6.2
10.0 – 15.0	3.6	5.3	0.8	1.4	6.6
15.0 – 20.0	3.7	6.2	1.7	3.1	8.0
20.0 – 30.0	9.1	7.7	3.7	4.0	13.2
30.0 – 40.0	12.2	8.6	4.7	5.0	16.5

Table 3.1: Systematic uncertainties on the inclusive jet cross section in the individual p_T^{jet} bins.

3.3.2 Multiple parton interactions and hadronisation corrections

The NLO calculations do not take into account the possibility of an *underlying event*[1], which leads to an increased energy flow between the electrons taking part in the process, and therefore to a larger cross section above any given threshold in the jet transverse momentum. Any interaction other than the hard process, is referred to as *underlying event*. This includes initial- and final state radiation, and any interactions between the outgoing particles. PYTHIA 6.221 has been used to study the effect of either considering (default) or leaving out multiple interactions for the signal Monte Carlo. In PYTHIA the underlying event is modelled by multiple parton interactions (MIA). At the lowest transverse momenta considered the signal Monte Carlo cross section increases by up to 20% when including MIA. This effect reduces to less than 10% for transverse momenta larger than 7 GeV.

The measured inclusive jet cross section will be compared to NLO QCD calculations which describe jet cross sections for partons, while the experimental cross section is presented for hadrons. There is as yet no rigourous way to use the Monte Carlo generators to correct the partons in the NLO predictions for this process so that they could be compared to the data, because the partons in the Monte Carlo generators and the partons in the NLO calculations are defined in different ways. But because the usage of Monte Carlo generators is the only available option so far, they are used to approximate the size of this hadronisation correction. The size of the hadronisation corrections have been estimated using PYTHIA 6.221. At $p_T^{jet} = 5$ GeV the correction is about

[1] I denote the interactions between the incoming or outgoing particles not covered by the hard process as the *underlying event*.

15%. The correction decreases with increasing p_T^{jet} and is below 5% in our study for $p_T^{jet} > 20$ GeV. Disabling MIA in PYTHIA while determining the hadronisation corrections leads to values of the correction factors within 2% of those determined with MIA enabled.

3.4 Differential cross section

The inclusive jet cross sections have been measured for the photon–photon kinematical region of invariant masses of the hadronic final state $W > 5$ GeV, and a photon virtuality of $Q^2 < 4.5$ GeV^2. The results are compared to predictions of PYTHIA 6.221 and NLO perturbative QCD [32–34].

The NLO cross sections are calculated using the QCD partonic cross sections in NLO for direct, single- and double-resolved processes, convoluted with the Weizsäcker-Williams effective photon distribution. The hadronisation corrections discussed in section 3.3.2 are applied to the NLO calculation before it is compared to the data. The GRV-G HO parametrisation of the parton densities of the photon [35,36] is used with $\Lambda^{(5)}_{DIS} = 131$ MeV. The renormalisation and factorisation scales in the calculation are set equal to p_T^{jet}. The cross section calculations were repeated for the kinematic conditions of the present analysis. The calculations shown below are obtained from [32]. We have verified that using the independent calculation presented in [33,34] yields results within 5%, except in the lowest bin in p_T^{jet}, where it predicts a cross section about 25% higher.

Figure 3.7 and Table 3.2 show the cross section as a function of p_T^{jet} for $|\eta^{jet}| < 1.5$. Both PYTHIA 6.221 and the NLO calculation achieve a good description of the data, with the exception of the lowest bin in p_T^{jet}, where the NLO calculation is too low.

In order to be able to compare the results of the analysis with the results presented by the L3 collaboration in [11], the analysis was repeated with the same kinematic conditions which were used in that analysis. The resulting cross section is shown in Figure 3.8 and Table 3.3. As can be seen, the current analysis finds lower production cross sections at high p_T^{jet} than the L3 study, thus being in good agreement with the NLO and PYTHIA calculations performed for these kinematic conditions.

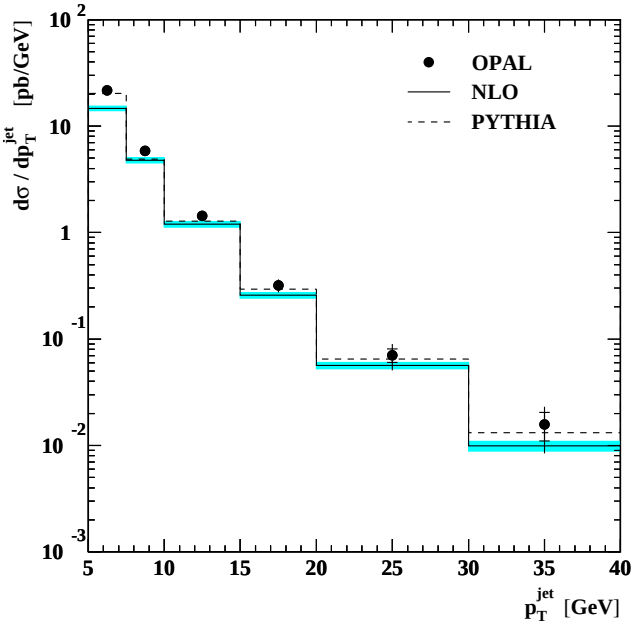

Figure 3.7: Inclusive jet differential cross section, $\mathrm{d}\sigma/\mathrm{d}p_{\mathrm{T}}^{\mathrm{jet}}$, for all jets with $|\eta^{\mathrm{jet}}| < 1.5$ compared to NLO and PYTHIA 6.221 predictions. The total of statistical and systematic uncertainties are shown where larger than the marker size. The band on the NLO shows the uncertainty associated to the variation of the renormalisation and factorisation scale.

$p_{\mathrm{T}}^{\mathrm{jet}}$ [GeV]			$\langle p_{\mathrm{T}}^{\mathrm{jet}} \rangle$ [GeV]	Background [%]	$\mathrm{d}\sigma/\mathrm{d}p_{\mathrm{T}}^{\mathrm{jet}}$ [pb/GeV]	
5.0	–	7.5	5.9	14.9 ± 0.1	$(21.7 \pm 0.2 \pm 1.3)$	
7.5	–	10.0	8.5	19.3 ± 0.2	$(58.5 \pm 0.9 \pm 3.6)$	$\times 10^{-1}$
10.0	–	15.0	11.8	22.5 ± 0.4	$(14.3 \pm 0.3 \pm 0.9)$	$\times 10^{-1}$
15.0	–	20.0	16.9	28.9 ± 0.9	$(31.8 \pm 1.9 \pm 2.6)$	$\times 10^{-2}$
20.0	–	30.0	23.5	47.1 ± 1.6	$(70.3 \pm 10.2 \pm 9.3)$	$\times 10^{-3}$
30.0	–	40.0	33.0	57.1 ± 3.2	$(15.7 \pm 4.7 \pm 2.6)$	$\times 10^{-3}$

Table 3.2: Background fraction and inclusive jet cross section for $|\eta^{\mathrm{jet}}| < 1.5$ as a function of $p_{\mathrm{T}}^{\mathrm{jet}}$. For the cross section values the first uncertainty is statistical, the second is systematic. The uncertainty given for the background fraction is statistical only.

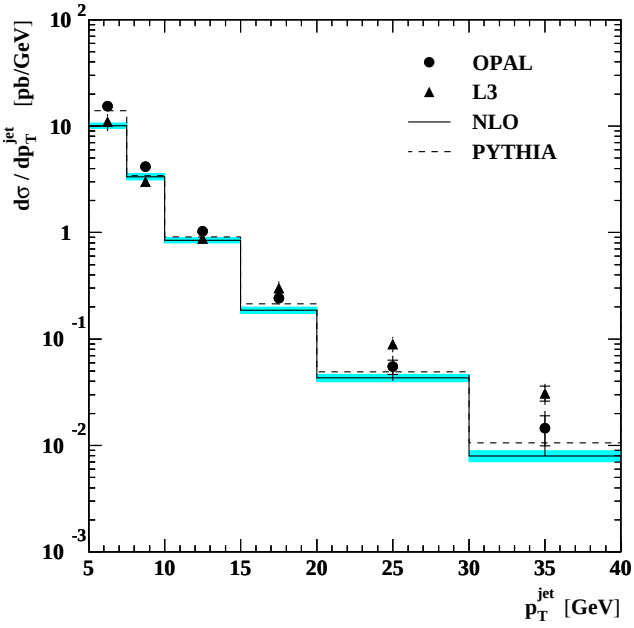

Figure 3.8: Inclusive jet differential cross section, $\mathrm{d}\sigma/\mathrm{d}p_{\mathrm{T}}^{\mathrm{jet}}$, for all jets with $|\eta^{\mathrm{jet}}| < 1.0$ compared to NLO and PYTHIA 6.221 predictions. The total of statistical and systematic uncertainties are shown where larger than the marker size. The band on the NLO shows the uncertainty associated to the variation of the renormalisation and factorisation scale.

$p_{\mathrm{T}}^{\mathrm{jet}}$ [GeV]			$\langle p_{\mathrm{T}}^{\mathrm{jet}} \rangle$ [GeV]	Background [%]	$\mathrm{d}\sigma/\mathrm{d}p_{\mathrm{T}}^{\mathrm{jet}}$ [pb/GeV]	
5.0	–	7.5	5.9	13.8 ± 0.1	$(15.3 \pm 0.1 \pm 0.9)$	
7.5	–	10.0	8.5	17.4 ± 0.3	$(41.5 \pm 0.8 \pm 2.4)$	$\times 10^{-1}$
10.0	–	15.0	11.8	21.6 ± 0.4	$(10.3 \pm 0.3 \pm 0.6)$	$\times 10^{-1}$
15.0	–	20.0	16.9	28.8 ± 0.9	$(34.1 \pm 1.6 \pm 1.6)$	$\times 10^{-2}$
20.0	–	30.0	23.3	47.6 ± 1.8	$(55.0 \pm 8.4 \pm 6.2)$	$\times 10^{-3}$
30.0	–	40.0	33.0	57.0 ± 3.6	$(14.5 \pm 4.5 \pm 2.0)$	$\times 10^{-3}$

Table 3.3: Background fraction and inclusive jet cross section for $|\eta^{\mathrm{jet}}| < 1.0$ as a function of $p_{\mathrm{T}}^{\mathrm{jet}}$. For the cross section values the first uncertainty is statistical, the second is systematic. The uncertainty given for the background fraction is statistical only.

Part II

Muon trigger efficiency measurements at ATLAS

CHAPTER 4

Rare B-decays at the LHC

The expected rate of B-hadron production will be enormous at the LHC, because of the large hadronic cross section for b quark production at the 14 TeV centre of mass energy delivered by the machine, and the high luminosity. ($\mathcal{L} = 10^{33}$ cm^{-2}s^{-1} is the goal for the first years of data-taking.) About one collision in every hundred is expected to produce a $b\bar{b}$ pair.

B-physics at ATLAS is going to rely heavily on the inclusive muon trigger described in Section 6.3.3. The selection of B-physics events by the trigger will start from a low-energy lepton detected by the Level-1 trigger, with High Level Trigger (HLT) algorithms searching for complex final states. Using this inclusive selection at Level-1, about 25% of the events triggered by the Level-1 muon trigger will contain b quarks. (As will be demonstrated in Figure 7.6.)

Even though the main focus of the ATLAS physics programme is the search for and study of physics beyond the Standard Model, through the observation of the decays of new particles, precision B-physics measurements will also be able to complement these searches, as shown in this chapter.

4.1 B-meson production at the LHC

ATLAS is going to be sensitive to B-hadrons produced with transverse momenta larger than ~ 20 GeV, which enables the usage of perturbative QCD to describe the b quark production. A calculation of the production cross section of heavy quarks as a function of the transverse momenta of the quarks [37] shows that in this kinematic region the effects of the b quark's mass can be neglected. (See Figure 4.1.)

The total $b\bar{b}$ production cross section is calculated to be about 500 μb at the LHC. The dependence of the b quark pair production cross section on the centre of mass energy of the colliding proton beams is demonstrated in Figure 4.2 together with the cross section of a few other processes. As can be seen, $b\bar{b}$ production will be one of the most prominent processes at the LHC.

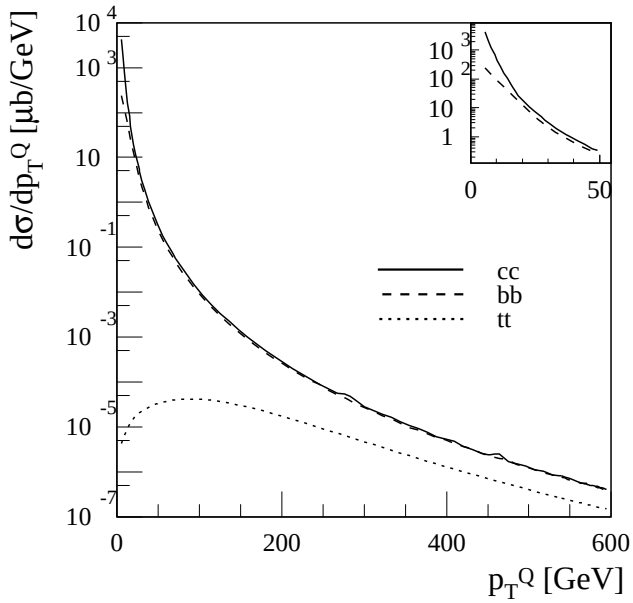

Figure 4.1: Differential cross section for heavy quark production as a function of the transverse momentum, $p_{\mathrm{T}}^{\mathrm{Q}}$, of the heavy quark, at the LHC. (Taken from [37].) The insert shows the charm and bottom production in the $p_{\mathrm{T}}^{\mathrm{Q}} < 50$ GeV region.

The relatively long lifetime of the b quark allows the formation of B-hadrons (mostly mesons), whose subsequent decays can be studied. Given the very large number of $b\bar{b}$ pairs created by the accelerator, the different B-hadrons will be produced with very large statistics, allowing precision measurements.

4.2 Rare muonic decays of B-mesons

Certain rare decays of B-hadrons, whose final states can be efficiently triggered by the Level-1 trigger in ATLAS, provide unique analysis possibilities. Given the high rate of B-hadron production at the LHC, decays with very small branching ratios will become observable. The decays most easily studied are of the type:

$$B_{d,s} \rightarrow \mu^+\mu^-(X). \tag{4.1}$$

Such decays involve flavour-changing neutral currents (FCNC) (see Figure 4.3) and are strongly suppressed in the Standard Model, with predicted branching ratios typically in the 10^{-5} – 10^{-10} range. For instance for the purely muonic

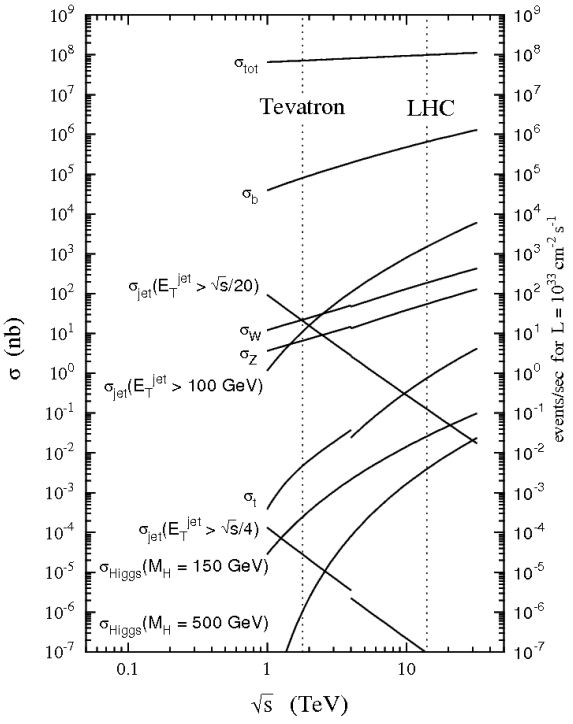

Figure 4.2: Cross sections for hard scattering processes, as a function of the centre of mass energy, $\sqrt{s}$. (Taken from [38].)

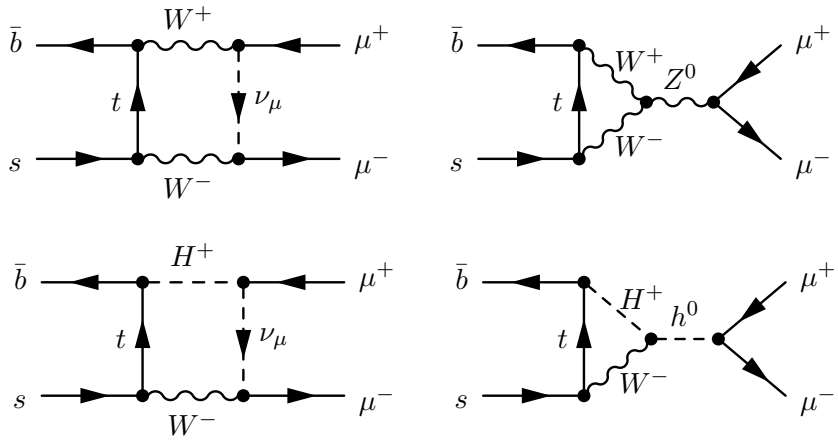

Figure 4.3: Sample diagrams contributing to the $B_s \to \mu\mu$ decay. The top two diagrams show FCNC processes allowed by the Standard Model, while the bottom two diagrams show processes allowed by the SM extension assuming two Higgs doublets.

$B_s \to \mu\mu$ decay, two diagrams – allowed by the Standard Model – contributing to the decay can be seen in the top of Figure 4.3.

However in many extensions of the Standard Model the branching ratios can be enhanced by providing more channels for the decays. As examples, the lower two diagrams in Figure 4.3 show possible decay processes in case of two Higgs doublets. As a result, any deviation in the branching ratios of these rare decays from the Standard Model predictions can be a strong indication for *New Physics*.

CHAPTER 5

$t\bar{t}$ production at the LHC

The top quark was discovered in 1995 [39, 40] at the Tevatron collider at Fermilab. It is to date the heaviest known elementary particle. Although more than 10 years have passed since its direct discovery, still it is the least known of all the quarks and leptons. The large mass of the top quark of about 172 GeV suggests that it might play a special role in nature. It behaves differently from all the other quarks because of its large mass, and corresponding short lifetime. The most notable difference is, that the top quark decays before it has time to hadronise, passing its spin information to its decay products. This provides a unique environment for studying the Standard Model and also to search for *New Physics*.

The top quark is the $Q = 2/3$ and $T_3 = +1/2$ member of the weak-isospin doublet also containing the bottom quark. It is the most recently discovered elementary particle, although its existence was suggested by the Standard Model ever since the discovery of the bottom quark in 1977 [41]. Indirect evidence for the existence of this particle became compelling over the years and constraints on the top quark mass, inferred from electroweak precision data, pointed to exactly the range where it was finally discovered. This meant a great success for the Standard Model.

In this chapter I summarise the experimental results obtained from studying the top quark, and describe its properties according to the Standard Model.

5.1 The discovery of the top quark

There are two main reasons why quarks should exist in doublets. First, it provides a natural way to suppress the experimentally not yet observed flavour changing neutral current (FCNC). Second, the Standard Model of electroweak interactions can be proven to be renormalisable under the condition that the sum of the electric charges, Q_f, of all left handed fermions is zero. The general proof that gauge theories can be renormalised, however, can only be applied

if the particular gauge theory is *anomaly free*[1]. This requires a delicate cancellation between different diagrams, relations which can be easily upset by anomalies due to fermion loops such as the one shown in Figure 5.1.

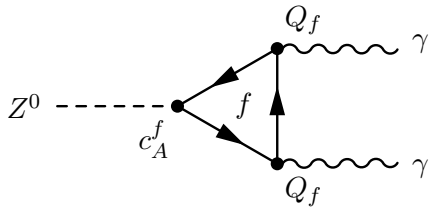

Figure 5.1: A fermion triangle diagram that could potentially cause an anomaly.

In general, anomaly freedom is guaranteed if the coefficient

$$d_{abc} = \sum_{\text{fermions}} \text{Tr}\left[\hat{\lambda}^a\{\hat{\lambda}^b, \hat{\lambda}^c\}_+\right] = 0, \tag{5.1}$$

where $\hat{\lambda}^i$ are the generators of the gauge group under consideration. In the Standard Model of electroweak interactions, the gauge group $SU(2) \times U(1)$ is generated by the three Pauli matrices, σ_i, and the hypercharge Y, so $\hat{\lambda}^i = \sigma_i$, for $i = 1, 2, 3$, and $\hat{\lambda}^4 = \hat{Y} = 2(\hat{Q} - \hat{T}_3)$. In the specific example shown in Figure 5.1, one consequence of Equation 5.1 is a relation where each triangle is proportional to $c_A^f Q_f^2$, where Q_f is the electric charge and c_A^f is the axial coupling of the weak neutral current. Thus, for an equal number (N) of lepton and quark doublets, the total anomaly is proportional to:

$$d \propto \sum_{i=1}^{N} \left(\frac{1}{2}(0)^2 - \frac{1}{2}(-1)^2 + \frac{1}{2}N_c\left(+\frac{2}{3}\right)^2 - \frac{1}{2}N_c\left(-\frac{1}{3}\right)^2 \right). \tag{5.2}$$

Consequently, taking into account the three colours of each quark ($N_c = 3$), the anomalies cancel. As three lepton doublets were observed many years ago, while not observing anomalies such as the one shown in Figure 5.1, the existence of the top quark has been suggested ever since the discovery of the bottom quark in 1977.

There is a lot of indirect experimental evidence for the existence of the top quark. Experimental limits on the FCNC decays of the b quark [42,43] such as $b \to sl^+l^-$ and the absence of large tree level (lowest order) $B_d^0\bar{B}_d^0$ mixing at the $\Upsilon(4S)$ resonance [44–47] rule out the hypothesis of an isosinglet b quark. The most compelling argument for the existence of the top quark came from the

[1] A gauge theory might be renormalisable, even if it is not anomaly free. The general proof of renormalisability, however, cannot be applied if it is not.

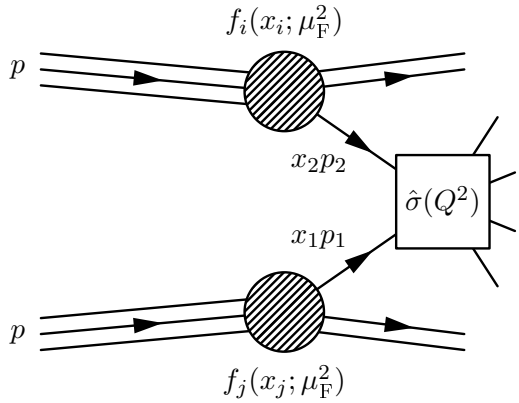

Figure 5.2: Parton model description of a hard scattering process using the factorisation approach.

wealth of data accumulated at the e^+e^- colliders LEP and SLC, particularly the detailed studies of the $Zb\bar{b}$ vertex near the Z resonance [48].

For a long time direct searches have been conducted at e^+e^- and hadron colliders to find the top quark in various reactions. The e^+e^- colliders found no direct evidence of $t\bar{t}$ pair creation, and could only raise the limits on the top quark mass in such searches. Finally, after a series of publications, the CDF and DØ experiments published the discovery of the top quark in strong $t\bar{t}$ production in [39, 40] with a production cross section $\sigma_{t\bar{t}} = 6.5\pm3$ pb at 1.8 TeV centre of mass energy.

5.2 $t\bar{t}$ production by strong interaction

The $t\bar{t}$ production at high energy pp collisions is described by perturbative QCD. In this approach, a hard scattering process between the two protons leads to an interaction between the quarks and gluons that make up the incoming protons. The description of the collisions can be separated into a short distance (hard scattering) partonic cross section for the participating partons of type i and j, $\hat{\sigma}^{ij}$, and into long distance terms which are factored into the parton longitudinal momentum distribution functions (PDFs), $f_i(x_i, \mu_F^2)$. This separation is called factorisation, and is depicted in Figure 5.2.

The separation is set by the factorisation scale μ_F^2. The short distance cross section only involves high momentum transfer and because of this, is calculable in perturbative QCD. It is insensitive to the physics of low momentum scale. It has to be noted, that when including higher order terms in the perturbative expansion, the dependence on the arbitrary μ_F^2 scale gets weaker. To demonstrate the PDF's dependence on the μ_F^2 scale, Figure 5.3 shows an example parametrisation, obtained by the CTEQ collaboration [49], for two

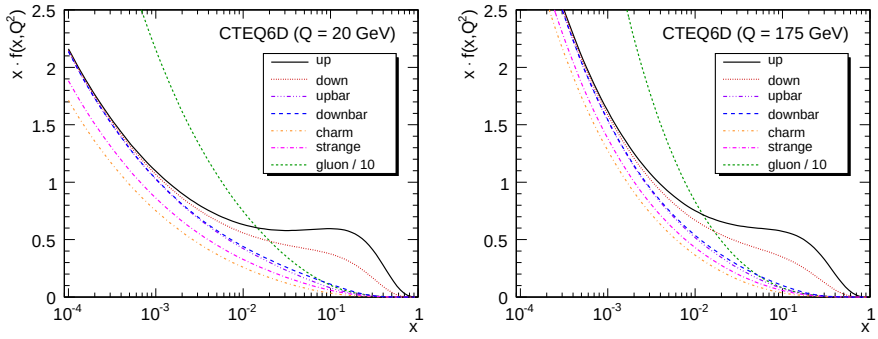

Figure 5.3: The quark, anti-quark and gluon momentum densities in the proton as a function of the longitudinal proton momentum fraction x at $Q^2 = 20$ GeV^2 (left) and at $Q^2 = m_t^2$ (right) from the CTEQ6D parametrisation [49].

different $Q^2 = \mu_{\mathrm{F}}^2$ scales.

In higher order calculations, infinities such as ultra-violet divergences appear. These divergences can be removed by a renormalisation procedure, which introduces another artificial scale, μ_{R}^2. But of course the physical quantities cannot depend on arbitrary scales such as μ_{F}^2 or μ_{R}^2. It is usual to use the same scale, $Q^2 = \mu^2$ for both, a convention which is used in the following.

The total top quark pair production cross section for hard scattering processes, initiated by a pp collision at a centre of mass energy $\sqrt{s}$ can be calculated as:

$$\sigma_{t\bar{t}}(\sqrt{s}, m_t) = \sum_{i,j=q,\bar{q},g} \int dx_i dx_j f_i(x_i, \mu^2) f_j(x_j, \mu^2) \times \hat{\sigma}_{ij\to t\bar{t}}(\rho, m_t^2, x_i, x_j, \alpha_s(\mu^2), \mu^2)\,, \tag{5.3}$$

where $f_i(x_i, \mu^2)$ and $f_j(x_j, \mu^2)$ are the PDFs of the two interacting protons. The summation indices i and j run over all $q\bar{q}$, gg, gq and $\bar{q}g$ pairs, and $\rho = 4m_t^2/\sqrt{s'}$, in which $s' = x_i x_j s$ is the effective centre of mass energy squared for the partonic process. The lowest order parton processes for top pair creation are shown in Figure 5.4.

As there has to be at least enough energy in the process to produce a $t\bar{t}$ pair at rest, $s' \geq 4m_t^2$ has to apply. This can be written as $x_i x_j = s'/s \geq 4m_t^2/s$. Since the probability of finding a parton with momentum fraction x in the proton falls with increasing x – as demonstrated in Figure 5.3 –, the typical value of $x_i x_j$ is near the threshold in $t\bar{t}$ production. Setting $x_i \approx x_j \equiv x$ gives the following:

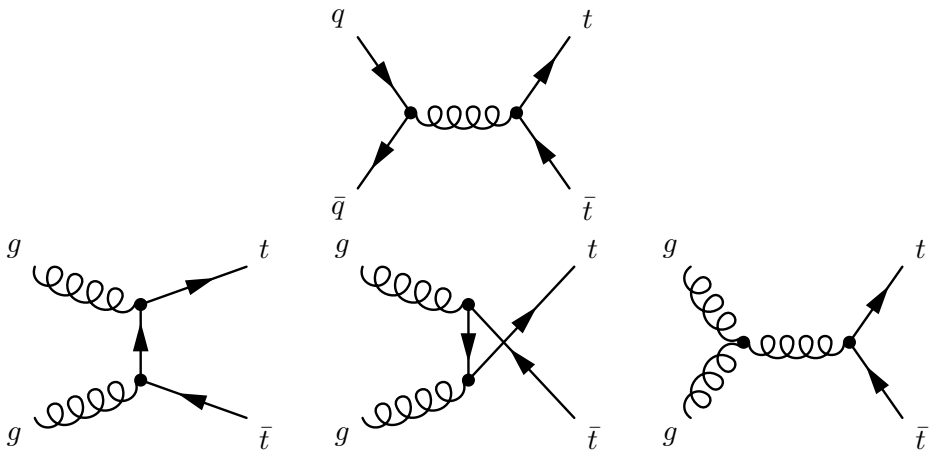

Figure 5.4: Leading order processes for top pair production at hadron colliders. The Feynman-graphs show the quark annihilation (top) and gluon fusion (bottom) processes.

$$
\begin{aligned}
x &\approx \frac{2m_t}{\sqrt{s}} \\
&= 0.18 \qquad \text{at the TEVATRON in Run II} \\
&= 0.025 \qquad \text{at the LHC}
\end{aligned}
$$

as the typical value of x for $t\bar{t}$ production. It is interesting to observe at this point, that while at the TEVATRON $t\bar{t}$ production happens mainly by quark-antiquark annihilation, at the LHC $t\bar{t}$ production is vastly dominated by gluon-gluon fusion. Because of the small x value needed at the LHC, the $t\bar{t}$ production cross section is expected to be more than a 100 times larger than that observed at the TEVATRON.

Multiple calculations have been done in the past for the total $t\bar{t}$ production cross section at the LHC. ATLAS is using the calculation presented in [50] as reference, which is predicting a total $t\bar{t}$ production cross section of $\sigma_{t\bar{t}} = 833^{+52}_{-39}$ pb.

5.3 The top quark decay

Because of its large mass, the decay width of the top quark is dominated by the $t \to Wb$ two-body decay channel. If we neglect the terms of order m_b^2/m_t^2, α_s^2 and those of order $(\alpha_s m_W^2)/(\pi m_t^2)$ in the decay amplitude, we can express the predicted decay amplitude in the Standard Model as [51]:

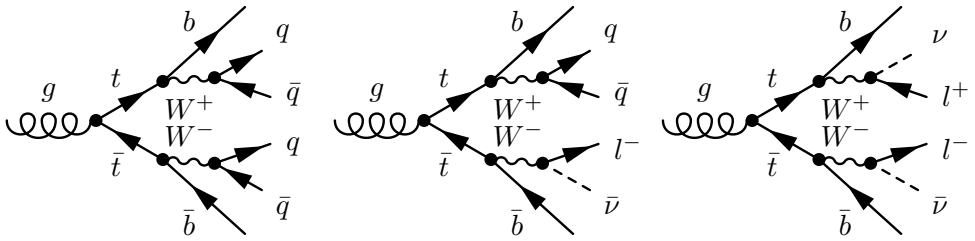

Figure 5.5: Diagrams of the three main $t\bar{t}$ decay channels: the all-jets channel (left), the semi-leptonic channel (middle) and the di-lepton channel (right).

$$\Gamma_t = \frac{G_{\mathrm{F}} m_t^3}{8\pi\sqrt{2}} \left(1 - \frac{M_W^2}{m_t^2}\right)^2 \left(1 + 2\frac{M_W^2}{m_t^2}\right) \left[1 - \frac{2\alpha_s}{3\pi}\left(\frac{2\pi^2}{3} - \frac{5}{2}\right)\right]. \qquad (5.4)$$

The decay width increases with the top mass, changing for example from 1.02 GeV for $m_t = 160$ GeV/c^2 to 1.56 GeV for $m_t = 180$ GeV/c^2 (using $\alpha_s(M_Z) = 0.118$). The corresponding lifetime of the top quark is $\approx 0.5 \times 10^{-24}$ s, which means that it decays to a b quark before top-flavoured hadrons or $t\bar{t}$-quarkonium bound states can form [52].

Given that the top quark decays in almost 100% of the time as $t \to Wb$, the final states of the top pair production process can be divided into three categories based on the decay of the participating W bosons. The three final state categories are demonstrated in Figure 5.5, showing the all-jets final state on the left, the semi-leptonic final state in the middle and the di-lepton final state on the right.

Because of *fermion universality* in electroweak interactions[2], in lowest order the W-boson decays 1/3 of the time into a $l\nu$ pair and 2/3 of the time into a $q\bar{q}$ pair. The latest measurements on the branching ratios are shown in Table 5.1.
As a result, the three different final states are observable with the following relative fractions:

- $t\bar{t} \to W^+bW^-\bar{b} \to q\bar{q}'bq''\bar{q}'''\bar{b}$ (45.7%)
- $t\bar{t} \to W^+bW^-\bar{b} \to q\bar{q}'bl\bar{\nu}_l\bar{b} + \bar{l}\nu_l bq\bar{q}'\bar{b}$ (43.7%)
- $t\bar{t} \to W^+bW^-\bar{b} \to \bar{l}\nu_l bl'\bar{\nu}_{l'}\bar{b}$ (10.6%)

[2]The W-boson can decay to pairs of leptons from all three generations and to pairs of quarks from the first two generations, each coming from three different colour states. Therefore, the W-boson can decay to $3 + 2 \cdot 3 = 9$ different fermion pairs with equal rate, yielding a branching ratio of 1/9 for each (neglecting the mass differences).

Decay mode	W branching fraction	
	Born level	Measured
$W^+ \to e^+\nu_e$	1/9	$10.75 \pm 0.13\%$
$W^+ \to \mu^+\nu_\mu$	1/9	$10.57 \pm 0.15\%$
$W^+ \to \tau^+\nu_\tau$	1/9	$11.25 \pm 0.20\%$
$W^+ \to$ hadrons	6/9	$67.60 \pm 0.27\%$

Table 5.1: Born level theoretical and best measured branching fractions [53] of the W^+-boson decay. Identical values are measured for the charge conjugate modes of the W^-.

CHAPTER 6

LHC and ATLAS

The Large Hadron Collider (LHC) [54] will provide physicists with unprecedented possibilities to study the properties of matter at the highest energies. It is designed to be a "discovery machine", making it possible to test many new theories of particle physics, and to look for particles and phenomena not observed before. Four large independent experiments are built around the LHC ring: Alice [55, 56], LHCb [57], CMS [58] and ATLAS [59]. They will make it possible to reach the full physics potential of the acceleraor by complementing each other's capabilities.

In this chapter I will review the accelerator, showing its capabilities. Then I will describe the largest of the four experiments by size – ATLAS – and show its projected performance.

6.1 The Large Hardon Collider

The LHC was designed to take advantage of the infrastructure already available at CERN. It uses the tunnel created for the LEP ring, and much of the accelerator complex built previously. A schematic view of the LHC accelerator complex is shown in Figure 6.1. As can be seen, the layout is basically the same as shown in Figure 2.1.

The LHC also relies on other parts of the complex to pre-accelerate and structure the proton beams before they are injected into the LHC rings for the final acceleration step to 7 TeV. The beam protons are created in a 90 kV Duoplasmatron proton source, first accelerated by a linear accelerator (Linac2) to 50 MeV and injected into the Proton Synchrotron Booster (PSB). The booster accelerates the protons to 1.4 GeV and injects them in the Proton Synchrotron (PS). The PS continues to accelerate the proton bunches to 25 GeV before they are injected in the Super Proton Synchrotron (SPS) ring. The SPS does the final step of acceleration before the beams get injected into the LHC rings. It accelerates the proton beams to 450 GeV. The final acceleration step is done

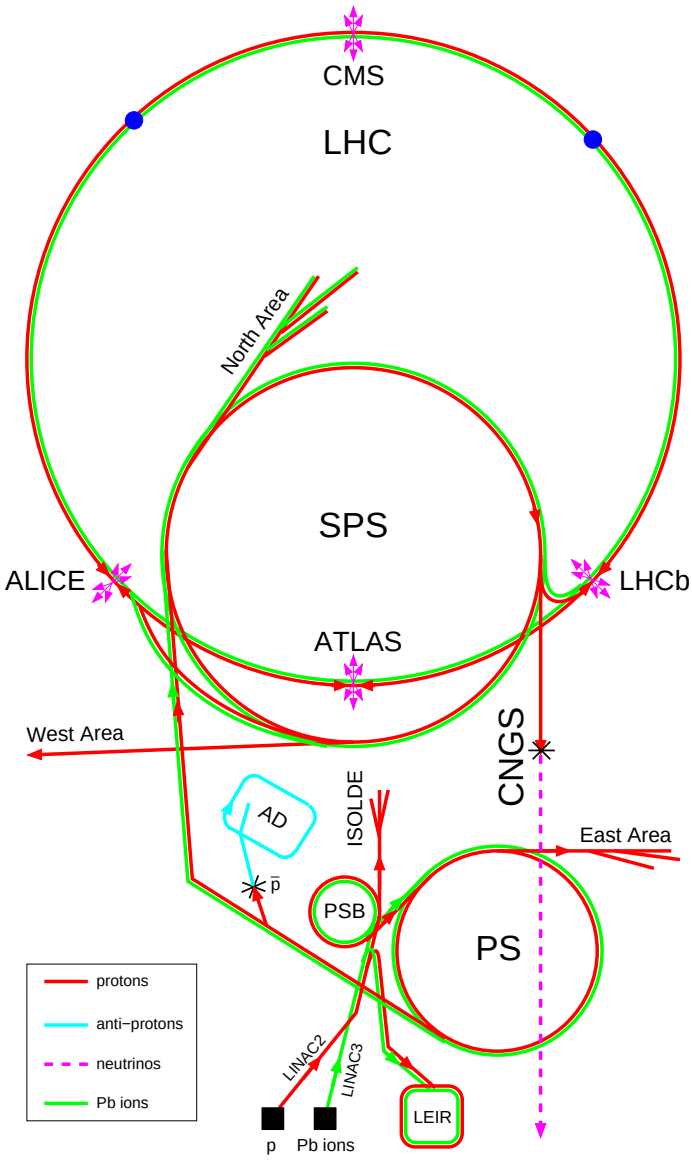

Figure 6.1: Schematic view of the LHC accelerator complex.

in the LHC rings. It accelerates the proton beams to 7 TeV each, resulting in interactions for the main experiments at a proton–proton centre of mass energy of 14 TeV.

Superconducting magnets are needed along the LHC ring to keep the proton beams in orbit with a 8.33 T peak dipole magnetic field.

6.1.1 The LHC luminosity

The instantaneous machine luminosity depends on the beam parameters, as shown already in Equation 2.1. The exploration of rare events requires a large luminosity from the accelerator, which requires high beam intensities, excellent focussing and a good beam lifetime. There are a number of effects that limit the luminosity that can be reached with the LHC.

- *Beam–beam limit:* The maximum particle density per bunch is limited by the nonlinear beam–beam interactions that each particle experiences when the bunches of the two beams collide with each other at the interaction regions.

- *Mechanical aperture:* The geometrical aperture of the LHC arcs is given by the beam screen dimensions. The beam screen has a height of approximately 2×17.3 mm and a total width of 2×22 mm. Requiring a minimum aperture of 10σ in terms of RMS beam size and assuming tolerances for linear machine imperfections, magnet alignment and geometry, implies a peak nominal beam size of 1.2 mm. Combined with the previous limiting factor, this implies a maximum bunch intensity of $N_{\mathrm{bunch}}(\mathrm{nominal}) = 1.15 \times 10^{11}$.

- *Energy stored in the machine:* A total nominal beam current of 0.584 A corresponds to a stored energy of approximately 362 MJ. In addition the LHC magnet system stores an electromagnetic energy of approximately 600 MJ yielding a total stored energy of more than 1 GJ. The machine has to be able to absorb this energy safely at the end of each run or in the case of a malfunction or emergency. This provides additional limits on the attainable beam energies and intensities.

- *Heat load:* Although the synchrotron radiation at the LHC is going to be small compared to an electron storage ring, it still poses a practical limit on the maximal beam intensities as this radiation has to be absorbed by the cryogenics system.

- *Collective beam instabilities:* The interactions of the charged particles in each beam with each other and with the conducting boundaries of the vacuum system can result in collective beam instabilities. These effects are usually proportional to the beam currents, and so limit the maximum attainable beam intensities.

All these constraints limit the ultimate LHC instantaneous luminosity to about $\mathcal{L} = 10^{34}\ \mathrm{cm}^{-2}\mathrm{s}^{-1}$.

The luminosity of the LHC is not going to be constant over a physics run, but it will decay due to the degradation of intensities and emittances of the circulating beams. The luminosity lifetime of the machine is expected to be $\tau_{\mathcal{L}} = 14.9$ h. The optimal LHC turn-around time[1] between two fills is expected to be about $T_{\rm ta} = 70$ minutes. From the experience with HERA, one expects a realistic turn-around time on the order of 7 hours [54]. The total integrated luminosity per year attains a maximum if the run per fill time satisfies the following equation [54]:

$$\ln\left(\frac{T_{\rm ta}+T_{\rm run}}{\tau_{\mathcal{L}}}+1\right)=\frac{T_{\rm run}}{\tau_{\mathcal{L}}} \tag{6.1}$$

Assuming a luminosity lifetime of 15 h, the optimum run times are 12 h and 5.5 h for an average turn-around time of 7 h and 1.2 h respectively. These give a maximum total luminosity per year between 80 fb^{-1} and 120 fb^{-1}.

6.2 A Toroidal LHC ApparatuS

The high interaction rates, radiation doses, particle multiplicities and energies at the LHC, together with the requirements for precision measurements, require new standards in the design of particle detector systems. ATLAS (A Toroidal LHC ApparatuS) is the larger one of the two general purpose detectors built for the LHC [59]. In this section I will show the main properties of ATLAS together with its main physics capabilities.

The most important benchmark to define the performance of each subsystem of ATLAS has been the need to detect the Standard Model Higgs boson over a wide range of possible Higgs masses. The detector also aims to be able to detect a large number of possible new phenomena. These goals set the following requirements for the LHC detectors in general:

- The detectors require fast, radiation-hard electronics and sensor elements. In addition, high detector granularity is needed to handle the particle fluxes and to reduce the influence of overlapping events.
- Large acceptance in pseudorapidity with almost full azimuthal angle coverage is required.[2]

[1] This is the time necessary to refill the accelerator with proton beams and start the collisions, after dumping the previous load.

[2] The right-handed coordinate system of ATLAS is the following: The beam direction defines the z-axis and the x-y plane is transverse to the beam direction. The positive x-axis is defined as pointing from the interaction point to the centre of the LHC ring and the positive y-axis is defined as pointing upwards. The azimuthal angle ϕ is measured around the beam axis, and the polar angle θ is measured from the beam axis. The pseudorapidity is defined as $\eta \equiv -\ln\tan(\theta/2)$.

- Good charged-particle momentum resolution and reconstruction efficiency is needed in the inner tracker. For the offline tagging of τ-leptons and b-jets, vertex detectors close to the interaction point are required to observe secondary vertices.

- Good electromagnetic calorimetry is required for electron and photon identification and measurements, complemented by a full coverage of hadron calorimetry for accurate jet and missing transverse energy[3] ($\not{E}_{\mathrm{T}}$) measurements.

- Good muon identification and momentum resolution is required up to the TeV scale, as well as the ability to determine the charge of the muons even at the highest p_{T}.

- Highly efficient triggering is needed for objects with high transverse momenta, with sufficient background rejection. The trigger has also to provide acceptable readout rates for most physics processes of interest.

The layout of the ATLAS detector is shown in Figure 6.2. ATLAS uses a special magnet system comprising four separate magnets, a thin superconducting solenoid surrounding the inner-detector cavity, and three large superconducting toroids – one barrel and two end-caps. The design of the magnets largely drove the design of the rest of the detector. The performance goals of the detector are listed in Table 6.1.

6.2.1 The inner detector

The Inner Detector (ID) uses pixel and silicon microstrip (SCT) trackers in conjunction with a Transition Radiation Tracker (TRT). It is immersed in a 2 T magnetic field generated by the central solenoid, which has a length of 5.3 m and a diameter of 2.5 m.

The precision tracking detectors cover the $|\eta| < 2.5$ pseudorapidity region. They are arranged on concentric cylinders around the beam axis in the barrel region, while in the end-cap regions they are located on disks perpendicular to the beam axis. The highest granularity is achieved around the vertex region using silicon pixel detectors. All of the 1744 pixel sensors are identical and have a minimum pixel size of 50×400 μm^2. The intrinsic accuracies in the barrel are 10 μm ($R-\phi$) and 115 μm (z), and in the end-caps 10 μm ($R-\phi$) and 115 μm (R). The intrinsic accuracies of the SCT per module in the barrel are 17 μm ($R-\phi$) and 580 μm (z), and in the end-caps 17 μm ($R-\phi$) and 580 μm (R). The TRT only provides $R-\phi$ information, for which it has an intrinsic accuracy of 130 μm.

[3] $\not{E}_{\mathrm{T}}$ is defined as the time component of the missing transverse momentum four-vector.

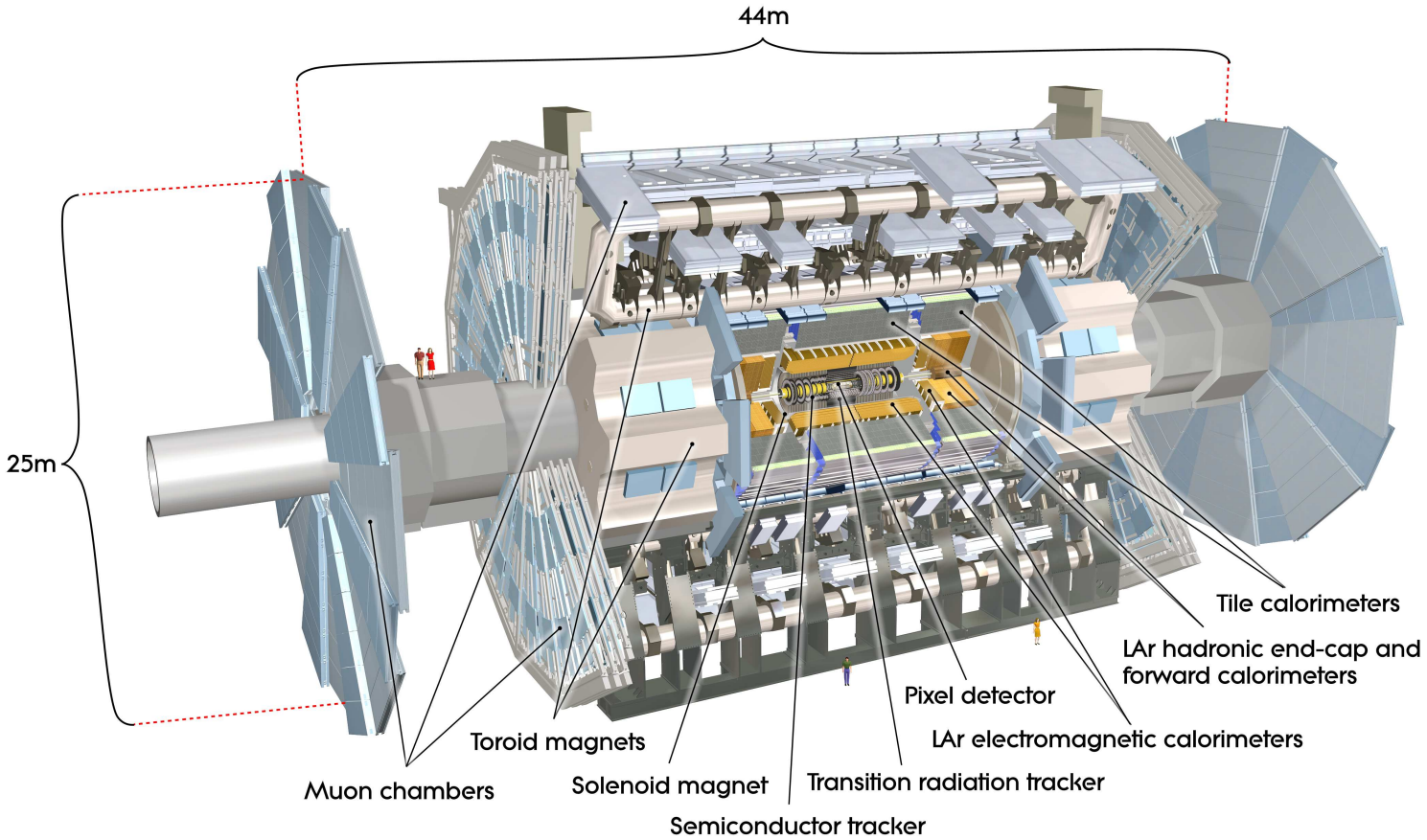

Figure 6.2: Cut-away view of the ATLAS detector.

Component	**Required resolution**	**η coverage**	
		Reconstruction	Level-1 trigger
Tracking	$\sigma_{p_{\mathrm{T}}}/p_{\mathrm{T}} = 0.05\%\ p_{\mathrm{T}} + 1\%$	± 2.5	—
EM calorimetry	$\sigma_E/E = 10\%/\sqrt{E} + 0.7\%$	± 3.2	± 2.5
Hadron calorimetry (jets)			
barrel and end-cap	$\sigma_E/E = 50\%/\sqrt{E} + 3\%$	± 3.2	± 3.2
forward	$\sigma_E/E = 100\%/\sqrt{E} + 10\%$	$3.1 < \lvert\eta\rvert < 4.9$	$3.1 < \lvert\eta\rvert < 4.9$
Muon spectrometer	$\sigma_{p_{\mathrm{T}}}/p_{\mathrm{T}} = 10\%$ at $p_{\mathrm{T}} = 1$ TeV	± 2.7	± 2.4

Table 6.1: General performance goals of the ATLAS detector. The E and p_{T} variables are expressed in GeV, and are used as dimension-less parameters. Note that for high-p_{T} muons, the muon-spectrometer performance is independent of the inner-detector system.

6.2.2 The electromagnetic calorimeter

The electromagnetic (EM) calorimeter is divided into a barrel part ($|\eta| < 1.475$) and two end-cap components ($1.375 < |\eta| < 3.2$), each housed in its own cryostat (See Figure 6.3.). The position of the central solenoid in front of the EM calorimeter demands optimisation of the material in order to achieve the desired calorimeter performance. As a consequence, the central solenoid and the LAr calorimeter share a common vacuum vessel, thereby eliminating two vacuum walls. The barrel calorimeter consists of two identical half-barrels, separated by a small gap (4 mm) at $z = 0$. Each end-cap calorimeter is mechanically divided into two coaxial wheels: an outer wheel covering the region $1.375 < |\eta| < 2.5$, and an inner wheel covering the region $2.5 < |\eta| < 3.2$.

The EM calorimeter is a lead – liquid argon detector with accordion-shaped kapton electrodes and lead absorber plates over its full coverage. The accordion geometry provides complete ϕ symmetry without azimuthal cracks. The lead thickness in the absorber plates has been optimised as a function of η in terms of EM calorimeter performance and energy resolution. Over the region devoted to precision physics ($|\eta| < 2.5$), the EM calorimeter is segmented into three longitudinal sections. For the end-cap inner wheel, the calorimeter is segmented in two longitudinal sections and has a coarser lateral granularity than for the rest of the acceptance.

In the region of $|\eta| < 1.8$, a presampler detector is used to correct for the energy lost by electrons and photons upstream of the calorimeter. The presampler consists of an active liquid argon layer with a thickness of 1.1 cm in the barrel, and 0.5 cm in the end-cap region.

6.2.3 The hadron calorimeter

The hadron calorimeter is built from three completely separate parts: a tile calorimeter in the barrel region, and two liquid argon end-caps. Their layout is demonstrated in Figure 6.3. The tile calorimeter is placed directly outside the EM calorimeter envelope. Its barrel covers the region $|\eta| < 1.0$, and its two extended barrels cover the range $0.8 < |\eta| < 1.7$. It is a sampling calorimeter using steel as the absorber and scintillating tiles as the active material. The barrel and extended barrels are divided azimuthally into 64 modules. Radially, the tile calorimeter extends from an inner radius of 2.28 m to an outer radius of 4.25 m. It is longitudinally segmented in three layers approximately 1.5, 4.1 and 1.8 interaction lengths (λ) thick for the barrel and 1.5, 2.6, and 3.3 λ for the extended barrel. The total detector thickness at the outer edge of the tile-instrumented region is 9.7 λ at $\eta = 0$. The tiles are 3 mm thick and the total thickness of the steel plates in one period (between two scintillating tiles) is 14 mm. Two sides of the scintillating tiles are read out by wavelength shifting

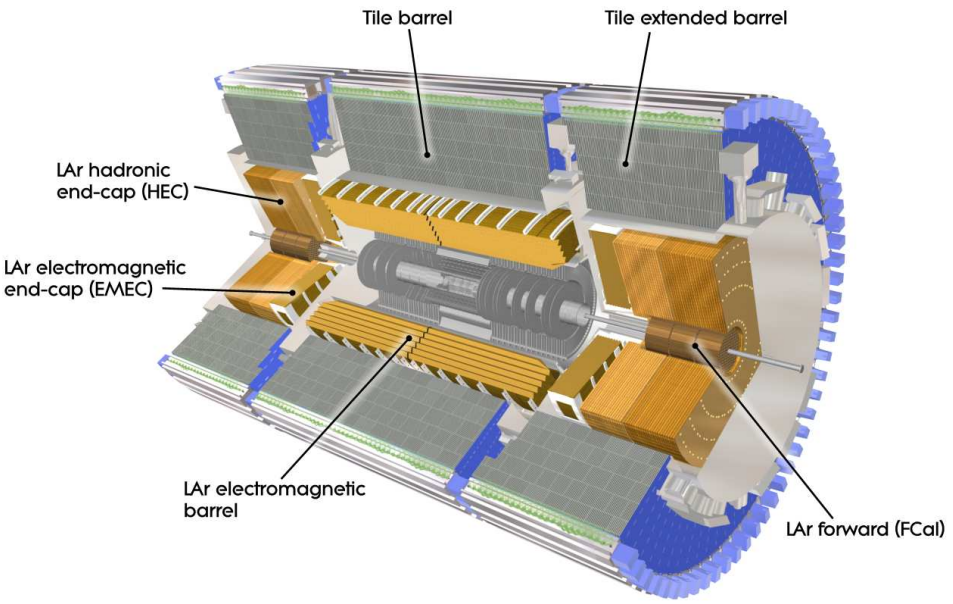

Figure 6.3: Cut-away view of the ATLAS calorimeter system.

fibres into two separate photomultiplier tubes. In η, the readout cells built by grouping fibres into the photomultipliers are pseudo-projective towards the interaction region – they are not pointing perfectly towards the interaction point, to minimise the probability of a hadron escaping the calorimeter.

The Hadronic End-cap Calorimeter (HEC) consists of two independent wheels per end-cap, located directly behind the end-cap electromagnetic calorimeter and sharing the same liquid argon cryostats. To reduce the drop in material density at the transition between the end-cap and the forward calorimeter (around $|\eta| = 3.1$), the HEC extends out to $|\eta| = 3.2$, thereby overlapping with the forward calorimeter. Similarly, the HEC η range also slightly overlaps with that of the tile calorimeter ($|\eta| < 1.7$) by extending to $|\eta| = 1.5$. Each wheel is built from 32 identical wedge-shaped modules, assembled with fixtures at the periphery and at the central bore. Each wheel is divided into two longitudinal segments, for a total of four layers per end-cap. The wheels closest to the interaction point are built from 25 mm parallel copper plates, while those further away use 50 mm copper plates (for all wheels the first plate has a thickness half of the rest). The outer radius of the copper plates is 2.03 m, while the inner radius is 0.475 m (except in the overlap region with the forward calorimeter where this radius becomes 0.372 m). The copper

plates are interleaved with 8.5 mm liquid argon gaps, providing the active medium for this sampling calorimeter.

6.2.4 The forward calorimeter

The Forward Calorimeter (FCal) is integrated into the end-cap cryostats, as this provides clear benefits in terms of uniformity of the calorimetric coverage as well as reduced radiation background levels in the muon spectrometer. In order to reduce the amount of neutrons reflected on the inner detector cavity, the front face of the FCal is recessed by about 1.2 m with respect to the EM calorimeter front face. This severely limits the longitudinal space available for this calorimeter and therefore calls for a high-density design.

The FCal is approximately 10 interaction lengths deep, and consists of three modules in each end-cap: The first is made of copper, and is optimised for electromagnetic measurements. The other two are made of tungsten, and measure predominantly the energy of hadronic interactions. Each module consists of a metal matrix, with regularly spaced longitudinal channels filled with the electrode structure consisting of concentric rods and tubes parallel to the beam axis. The liquid argon in the gap between the rod and the tube is the sensitive medium. This geometry allows for excellent control of the gaps, which are as small as 0.25 mm in the first section, in order to avoid problems due to ion buildup.

6.2.5 The muon spectrometer

Muon detection in ATLAS is based on the deflection of muon tracks in the large superconducting air-core toroid magnets. In the range $|\eta| < 1.4$, the magnetic bending is provided by the large barrel toroid. For $1.6 < |\eta| < 2.7$, muon tracks are bent by the two smaller end-cap toroid magnets inserted into both ends of the barrel toroid. Over the $1.4 < |\eta| < 1.6$ range – usually referred to as the transition region – magnetic deflection is provided by a combination of the barrel and end-cap toroid fields. The magnet configuration provides fields which are mostly orthogonal to the muon trajectories, while minimising the degradation of resolution due to multiple scattering. The conceptual layout of the muon spectrometer is shown in Figure 6.4. In the barrel region, tracks are measured in chambers arranged in three cylindrical layers around the beam axis; in the transition and end-cap regions, the chambers are installed in planes perpendicular to the beam, also in three layers.

The two end-cap toroids are inserted in the barrel toroid at each end and line up with the central solenoid. Each of the three toroids consists of eight coils assembled radially and symmetrically around the beam axis. The end-cap toroid coil system is rotated by 22.5° with respect to the barrel toroid coil

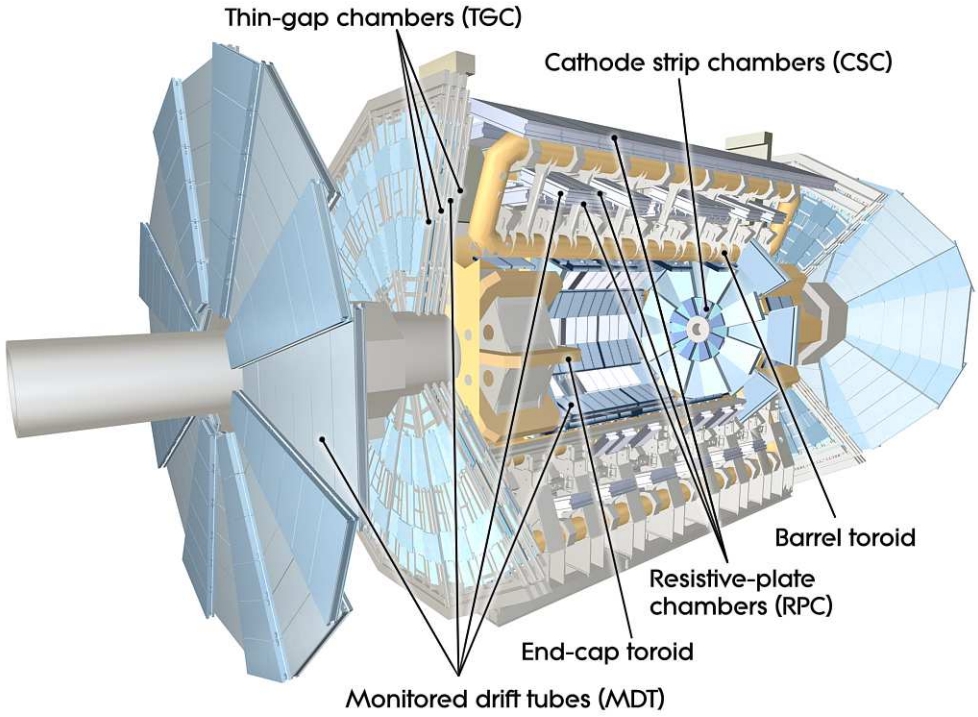

Figure 6.4: Cut-away view of the ATLAS muon system. The picture shows the location and layout of the various muon detector types.

system in order to provide radial overlap and to optimise the bending power at the interface between the two coil systems. (Figure 6.5.) The performance in terms of bending power is characterised by the field integral

$$\int B\delta l, \tag{6.2}$$

where B is the field component perpendicular to the muon direction and the integral is computed along an infinite-momentum muon trajectory (e.g. straight line originating at the interaction point), between the innermost and outermost muon-chamber planes. The barrel toroid provides 1.5 to 5.5 Tm of bending power in the pseudorapidity range $0 < |\eta| < 1.4$, and the end-cap toroids approximately 1 to 7.5 Tm in the region $1.6 < |\eta| < 2.7$. The bending power is lower in the transition regions where the two magnets overlap.

Monitored Drift Tubes (MDTs) are used over most of the η-range to measure the muon track coordinates in the principal bending direction with high precision. At large pseudorapidities, Cathode Strip Chambers (CSCs, which are multiwire proportional chambers with cathodes segmented into strips) with

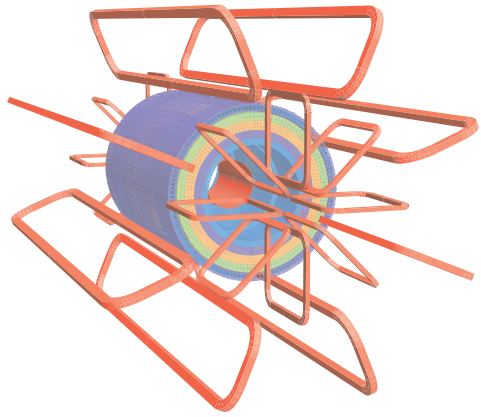

Figure 6.5: Geometry of the toroid magnet coils, together with the tile calorimeter steel.

higher granularity are used in the innermost plane over $2 < |\eta| < 2.7$, to withstand the demanding rate and background conditions. The stringent requirements on the relative alignment of the muon chamber layers are met by the combination of precise mechanical-assembly techniques and optical alignment systems both within and between muon chambers.

Dedicated trigger chambers cover the pseudorapidity range $|\eta| < 2.4$. These chambers have a pulse width narrower than the time between two bunch crossings, and provide fast signals for the trigger decision, but are less accurate than the precision chambers. Resistive Plate Chambers (RPCs) are used in the barrel region ($|\eta| < 1.05$) and Thin Gap Chambers (TGCs) are used in the end-caps ($1.05 < |\eta| < 2.4$). The purpose of the trigger chambers is actually threefold:

- Because of their high speed, they provide bunch-crossing identification for the detected muon tracks;
- They provide p_{T} threshold estimates for the detected muon candidates to be used by the Level-1 trigger system;
- They measure the muon coordinate in the direction orthogonal to that determined by the precision tracking chambers.

6.3 The ATLAS trigger system

The ATLAS Trigger and Data Acquisition (commonly called TDAQ) system has the task of selecting 200 events that are deemed interesting, from the

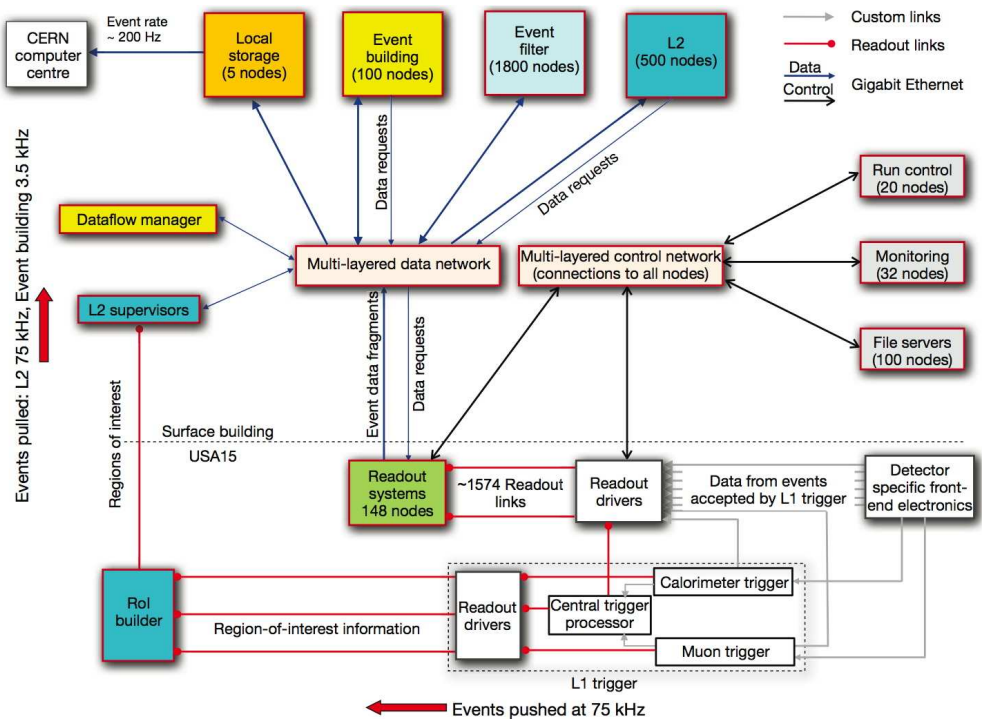

Figure 6.6: Block diagram of the ATLAS trigger and data acquisition systems.

40 million events produced every second by the LHC. The output rate is limited by the hardware used in the data acquisition, and the storage capacity available for ATLAS data. It is very important to have an efficient and well understood trigger system, since 99.9995% of the events will be thrown away by it. In the following I describe the general features of the ATLAS trigger system, with special emphasis on the single-muon trigger, as that is the main subject of the rest of the thesis.

ATLAS uses a three level trigger system. The levels are called: Level-1, Level-2 and Event-Filter. Each trigger level is designed to refine the decisions made at the previous level and, where necessary, apply additional selection criteria. A schematic view of the ATLAS TDAQ system is shown in Figure 6.6.

All the sub-detectors have to store their data for all the collisions in the last 2.5 μs, which is the time needed by the Level-1 trigger to make a decision. If the event is accepted by the Level-1 trigger, the whole event is read out from the front-end electronics by the Read Out System (ROS) PCs. At this point the event is stored in event fragments on 148 separate nodes. The Level-1 trigger provides special, so called Region of Interest (RoI) information to the

Level-2 trigger, which is transmitted on a dedicated data line.

The Level-2 trigger is guided by the RoI information coming from Level-1. It only requests information from the parts of the detector that have been flagged at Level-1 as interesting, and makes a decision based on that information. If the event is accepted at Level-2, the event is built by a dedicated farm of computers, and is given to the Event-Filter.

The Event-Filter makes its decision processing information from all the sub-detectors, and gives the final accept/reject signal. If an event is accepted by the full trigger chain, it is first stored locally in the surface buildings of ATLAS. The collected data is then periodically transferred to the CERN computer centre for further processing.

6.3.1 The Level-1 trigger system

The Level-1 trigger is built using custom-made electronics, as speed is of the highest importance here. It searches for signatures of high-p_{T} muons, electrons/photons, jets and τ-leptons decaying into hadrons. It also selects events with large missing transverse energy ($\not{E}_{\mathrm{T}}$) and total transverse energy (ΣE_{T}).

The Level-1 trigger uses reduced-granularity information from only a subset of the detectors: the RPC and TGC detectors for high-p_{T} muon identification, and all the calorimeter sub-systems to search for electromagnetic clusters, jets, τ-leptons, $\not{E}_{\mathrm{T}}$ and total transverse energy. As mentioned already, the Level-1 trigger system arrives at a decision within 2.5 μs of the bunch-crossing producing the event, with a maximum trigger rate of 75 kHz (upgradable to 100 kHz), which is limited by the readout systems.

Both the Level-1 calorimeter trigger and Level-1 muon trigger count the number of objects passing some selection criteria, and flag the event if it passed a certain event-level threshold (in the case of the $\not{E}_{\mathrm{T}}$ and ΣE_{T} triggers). These multiplicities and event level flags are transmitted on dedicated data lines to the Central Trigger Processor (CTP) for each bunch-crossing. The CTP makes the overall Level-1 trigger decision based on the received multiplicity information and event-level flags. The CTP can be programmed to handle a maximum of 256 so called trigger items. A trigger item is a condition which, if fulfilled, activates the Level-1 trigger.

Level-1 trigger items are identified by a single string that implies what was required by that item. They have the following form:

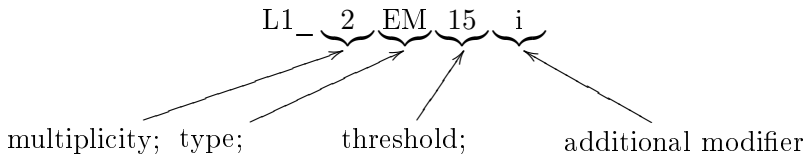

The trigger item in the example (L1_2EM15i) means that the Level-1 trigger has to find two isolated electromagnetic clusters that pass a 15 GeV threshold. The following threshold types can be specified for Level-1 trigger items: muon (MU); electron/gamma/tau (EM); jet (JT); forward jet (FJ); $\not{E}_{\mathrm{T}}$ (ME), ΣE_{T} (SE) and ΣE_{T} from all jets found (JE). Currently the only additional modifier used in the threshold names is "i", which means that the found object is *isolated* – the energy deposits in the calorimeters close to the object are below a certain threshold. A collection of such Level-1 trigger items is called the Level-1 trigger menu.

6.3.2 The high level trigger

The Level-2 and Event-Filter triggers are implemented using ordinary PCs, and together they are called the High Level Trigger (HLT). A functional layout of the HLT was shown at the top of Figure 6.6. The detector data for every event accepted at Level-1 is read out by ROS units, where they are temporarily stored and provided – on request – to the subsequent stages of the DAQ/HLT system.

As discussed already, the RoI information is sent on dedicated data paths from the Level-1 sub-systems to the RoI Builder, where they are assembled into a single data structure and forwarded to one of the Level-2 supervisors (L2SV). These nodes assign the events for which they received RoIs to one of the Level-2 processing units (L2PUs), and receive the results of the L2PU's analysis. The L2PUs make requests for event data using the received RoI information directly to the ROSs. After an accept or reject signal is returned to the L2SV, it forwards the decision to the DataFlow Manager (DFM). Also, in addition to sending the result of its analysis to the L2SV, an L2PU also sends a summary of its analysis to a Level-2 trigger-specific ROS. (This is called the Level-2 result data.)

The DFM (as the name suggests) controls the event flow in the experiment. If an event is found not to fulfil any of the Level-2 criteria, the DFM informs all the ROSs to delete the associated event data from their buffers. Each event which has been selected by the Level-2 trigger, is assigned by the DFM to an event-building node (called SFI). The SFI collects the event data from all the ROSs and builds a single event-data structure from them, the event. After building an event, the event data belonging to that event is deleted from the ROS buffers. The full event is then sent to the Event-Filter for further analysis.

The Event-Filter, in addition to the selection, classifies the selected events according to a pre-determined set of event streams and the result of this classification is added to the event structure. Selected events are subsequently sent to the output nodes (SFOs) of the TDAQ system. Conversely, those events

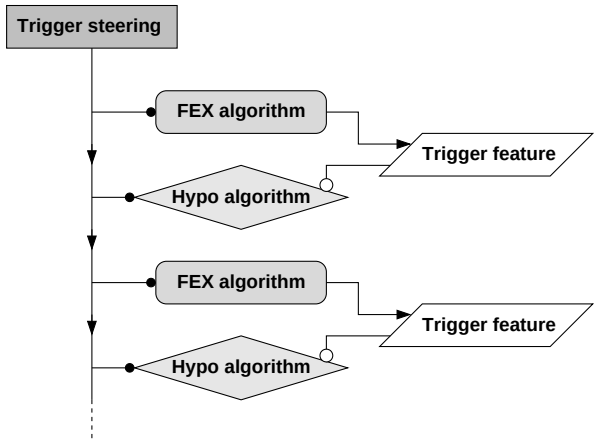

Figure 6.7: Functional diagram of a high level trigger chain.

not fulfilling any of the event filter selection criteria are expunged from the system. The events received by an SFO are stored in its local file system according to the classification performed by the event filter. The event files are subsequently transferred to CERN's central data-recording facility.

The HLT selection software

The HLT software – both at Level-2 and the Event-Filter – is composed of the following components (see Figure 6.7):

- **Trigger steering** is the main software component that receives an event for processing, and calls the selection algorithms in the order specified by the trigger configuration.
- **Feature extraction (FEX) algorithms** reconstruct detected particles or complex final states, and save the results of their reconstruction for the subsequent algorithms.
- **Hypothesis (Hypo) algorithms** take the results of previous FEX algorithms, and perform the actual trigger selection for specific signatures (e.g. 20 GeV isolated muon). They return true or false depending on whether the previously reconstructed object(s) fulfilled the selection criteria.

The trigger configuration defines chains of algorithms (trigger chains) for the HLT that have to be executed in the right sequence to test the fulfilment of a certain condition. The trigger steering executes all the trigger chains

one after the other, stopping with the execution of a chain if the event failed the selection of a hypothesis algorithm. Each trigger chain corresponds to an HLT trigger item, which is passed if the event passes the selection of all the hypothesis algorithms in the chain. Trigger items in the High Level Trigger are named similarly to the Level-1 items, the main difference being that the item type is written with lowercase letters. For instance the Level-1 item discussed previously could start the L2_2e15i Level-2 item. The names of the trigger chains are also written with lowercase letters, and take the form *2e15i* for instance.

6.3.3 The ATLAS single-muon trigger

The muon trigger system of ATLAS is described in [60]. The following is a short description of the selection performed at the various levels of the muon trigger.

Level-1

As mentioned in Section 6.2.5, Level-1 muon triggering is done with dedicated muon trigger chambers: Resistive Plate Chambers (RPCs) in the barrel region of the detector ($|\eta| < 1.05$) and Thin Gap Chambers (TGCs) in the end-cap regions ($1.05 < |\eta| < 2.4$). Muon candidates are identified and their p_{T} is estimated based on the deflection of their tracks by the toroid magnetic fields.

A demonstration of the "algorithm" is shown in Figure 6.8. If a hit is found in the pivot plane of the trigger chambers (RPC2 or TGC3), the trigger logic opens windows (so called "coincidence windows") in the neighbouring detector planes to look for coincident hits. If hits are found within the coincidence windows, muon candidates are created. Based on the size of the coincidence window in which the coincident hits are found, a p_{T} estimate is assigned to the muon candidate.

Dedicated electronics look for muon candidates in 64 barrel, 96 end-cap and 48 forward sectors[4]. The candidates are sent to the Muon to CTP Interface (MuCTPI), that creates the Regions of Interest for the Level-2 trigger from the received information, and sends the multiplicities of muon candidates passing the various p_{T} thresholds to the CTP.

Level-2

The Level-2 muon reconstruction is done in multiple steps. First, around each RoI coming from Level-1, muons are reconstructed by a fast algorithm – `muFast`

[4]The TGC detectors in the endcap area of the detector are commonly divided into an *endcap* ($1.05 < |\eta| < 1.9$) and a *forward* ($1.9 < |\eta| < 2.4$) region by the trigger community.

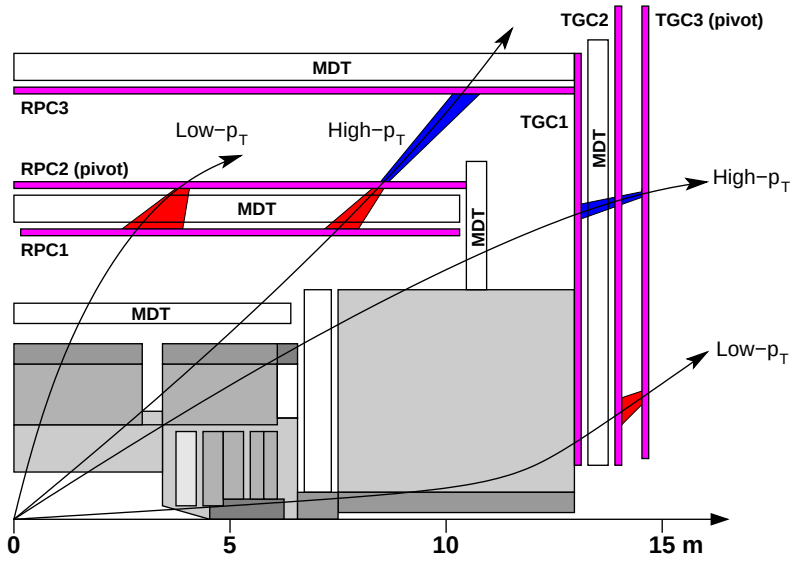

Figure 6.8: Layout of the muon trigger chambers and demonstration of the algorithm used at Level-1 to find muon trigger candidates.

[61] – using information only from the Muon Spectrometer. A hypothesis algorithm (`MufastHypo`) is run afterwards, that selects muon candidates with a p_{T} above a configurable threshold.

Next, the charged tracks are reconstructed in the Inner Detector in a window around the muon candidate reconstructed by `muFast`. Finally a match is searched for between the track reconstructed in the Muon Spectrometer and the tracks reconstructed in the Inner Detector by the `muComb` algorithm. A p_{T} selection is applied by a hypothesis algorithm (`MucombHypo`) on the combined muon candidates.

Event-Filter

The Event-Filter muon reconstruction (`TrigMoore` [62]) is built around the offline muon reconstruction package Moore/MuID [63]. It provides combined muon reconstruction in the Inner Detector and the Muon Spectrometer, using more precise calibration data and algorithms than at Level-2. The reconstructed muon candidates are selected by a single hypothesis algorithm, `TrigMooreHypo`.

I played a major role in writing software for the configuration and testing of the Level-1 central trigger hardware, and in creating their offline simulations. This code is now an official part of the ATLAS online and offline software.

CHAPTER 7

Muon triggers for B-physics in ATLAS

Selecting B-physics events at the LHC will be a non-trivial task. These events usually do not produce leptons or jets with high transverse momenta, or an overall large energy deposit in the detector. For this reason specialised trigger chains are used to select specific B-physics channels. In the High Level Trigger (HLT) usually complex signatures are searched for, which include multiple detected objects with low energy.

However in the Level-1 trigger, one cannot use too complicated signatures to start the before mentioned HLT chains. At initial, low luminosities (10^{30} - 10^{31} $\mathrm{cm}^{-2}\mathrm{s}^{-1}$) it will be possible to use low-p_{T} Level-1 single jet, electron and muon triggers, as the rate of these will be small enough to handle in the Level-2 trigger. However at design luminosities ($> 10^{32}$ $\mathrm{cm}^{-2}\mathrm{s}^{-1}$) such triggers would give too high rates for further processing.

For many physics processes no efficient triggering will be possible at nominal luminosities, but some channels will still be accessible. B-physics processes with two low-p_{T} muons in their final state may even be selected at Level-1 at high luminosities, as the di-muon trigger rate at Level-1 can be kept manageable even at the highest designed luminosity (10^{34} $\mathrm{cm}^{-2}\mathrm{s}^{-1}$).

7.1 The Level-1 di-muon triggers

The single-muon trigger of ATLAS is detailed in section 6.3.3. The Level-1 trigger uses dedicated, fast trigger chambers to detect muons. The muon tracks are bent in the toroidal magnetic field. From the track's deviation from a straight line, the transverse momentum of the muon can be estimated.

Triggering on di-muon signatures at Level-1 is complicated by the fact that the muon trigger sectors overlap with each other to maximise the acceptance

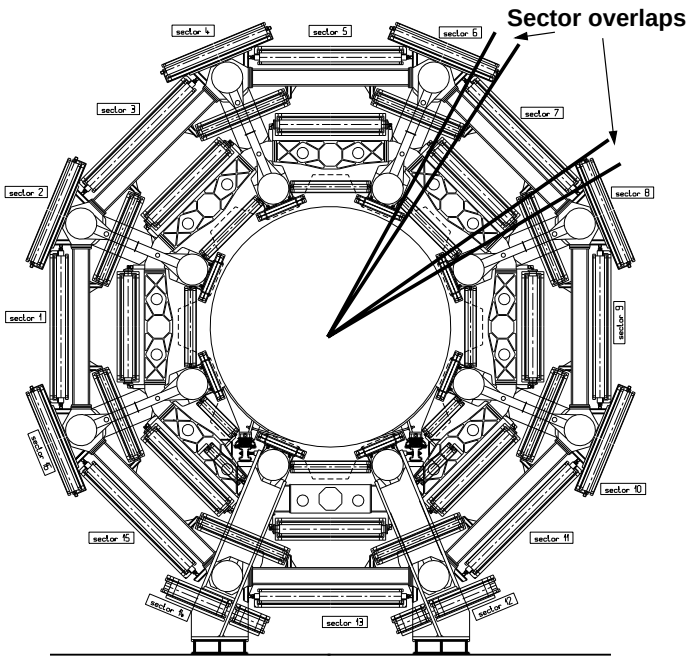

Figure 7.1: Azimuthal view of the ATLAS barrel muon detector chambers. The RPC trigger chambers are located in the middle and outer stations of the muon spectrometer.

of the trigger, so that it would not loose muons escaping between the sectors. This overlap of the trigger sectors is demonstrated in Figure 7.1 for the barrel sectors. Under certain azimuthal angles a muon may cross two neighbouring sectors, resulting in two Level-1 muon candidates being detected by the trigger electronics.

From purely geometrical considerations, a high-p_{T} muon has a 3% chance of hitting more than one muon trigger sector if it has an $|\eta| < 2.4$. The expected rate of di-muons coming from b-physics processes with the p_{T} of both muons larger than 6.0 GeV is about 300 Hz at a luminosity of 10^{33} cm^{-2}s^{-1}. At the same luminosity the single-muon 6 GeV Level-1 trigger is expected to give a 10–20 kHz trigger rate. From these simple considerations it is evident, that if the fake-double counts are not reduced somehow, they would give comparable or even larger trigger rates than the events with two real muons.

The muon candidates which are reconstructed by each barrel and end-cap sector separately, are transmitted to the Muon to Central Trigger Processor Interface (MuCTPI). The MuCTPI is responsible for collecting the muon candidates from all the trigger sectors, and transmitting them to the Region of Interest Builder (RoIB) and the Data Acquisition system (DAQ). It is also

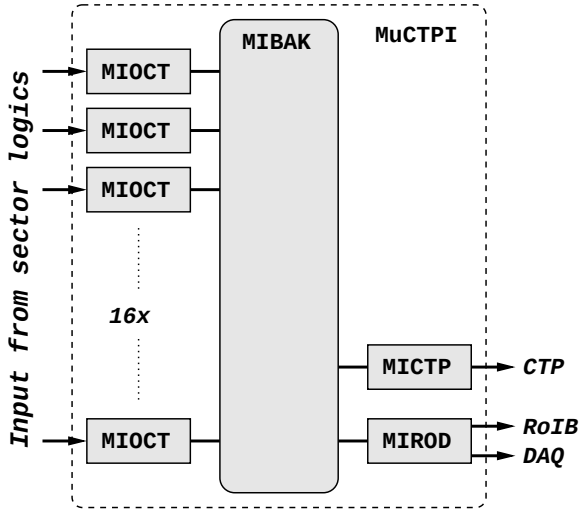

Figure 7.2: Schematic diagram of the structure of the MuCTPI.

responsible for calculating the total number of muon candidates passing each of the six programmable thresholds, taking the overlaps between the trigger sectors into account, before passing the multiplicities on to the CTP.

The schematic build of the MuCTPI is shown in Figure 7.2. The information about the Level-1 muon candidates are collected by the Muon Interface Octant (MIOCT) boards. There are 8 MIOCT boards for both hemisheres of the detector, giving 16 in total. These boards are responsible for calculating the multiplicities of the muon candidates in a given detector octant. One octant contains 4 barrel (Resistive Plate Chambers, RPC), 6 end-cap (Thin Gap Chambers, TGC) and 3 forward (TGC) sectors. The schematic layout of the trigger sectors in one octant is shown in Figure 7.3. The regions of the sectors which can be taken into account in the overlap handling, are shown in a shade of grey.

The MIOCT modules are plugged into a single VME crate with a custom backplane, called the Muon Interface Backplane (MIBAK). The main purpose of the dedicated backplane is to add up the multiplicities of the Level-1 muon candidates calculated in the different octants, to give the Level-1 muon multiplicity for the full detector.

The Muon Interface to Central Trigger Processor (MICTP) board is used to transmit this multiplicity information to the Central Trigger Processor (CTP) for each bunch-crossing. It is also the MICTP board that receives timing signals from the CTP and the accelerator.

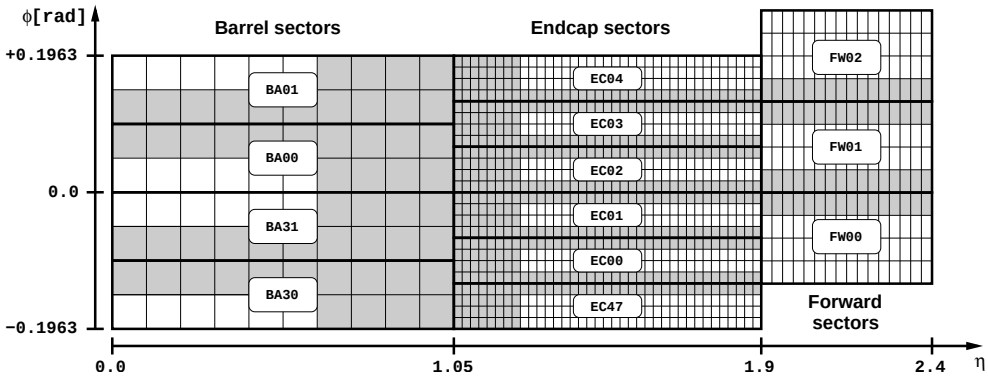

Figure 7.3: Overlaps handled by the MuCTPI. The figure shows the schematic layout of the sectors handled by a single MIOCT module. The RoIs which are considered in the overlap handling are shown in a shade of grey.

For the events accepted by the CTP, the information about the Level-1 muon candidates is read out through the Muon Interface Read-Out Driver (MIROD) board. It formats the information about the muon candidates into two separate ROD fragments to be sent to the Region of Interest Builder (RoIB) and the data acquisition (DAQ) system.

Since the Level-1 trigger hardware has to be very fast, the overlap resolution has to be done in a simple manner. I will use the notation of Figure 7.3 in the following description. The areas that can be taken into account in the overlap resolution are hard-coded in the design of the MIOCT boards. These areas are the following:

- The RoIs on the edge between BA00 & BA01 and BA30 & BA31 can be in overlap with each other. There is no overlap taken into account between BA31 and BA00. (Barrel–barrel overlap.)

- The 8 RoIs with the highest η in BA01 can be in overlap with the 32 RoIs with the lowest η in EC03 and EC04. The 8 RoIs with the highest η in BA00 can be in overlap with the 32 RoIs with the lowest η in EC02 and EC03. The overlaps are similar for BA30 and BA31. (Barrel–end-cap overlap.)

- The RoIs on the edge of the end-cap sectors can be in overlap with the RoIs of the neighbouring end-cap sector. (End-cap–end-cap overlap.)

- Similarly, the RoIs on the edge of the forward sectors can be in overlap with the RoIs of the neighbouring forward sectors. (Forward–forward overlap.)

A detailed description of the MIOCT board explaining how it can detect overlapping Level-1 muon candidates is given in [64]. The boards hold multiple carefully designed look-up tables (LUTs) that hold the RoI combinations that are considered to be overlapping with each other. The LUTs also store the p_{T} threshold and charge sign of the muon that is supposed to be considered to cause double-counting. This information is stored in the LUTs to retain flexibility, because we can only map the overlapping regions using simulations at the moment. With the start of data taking our understanding of the overlap areas might change.

As can be seen from Figure 7.3, all the end-cap and forward sectors overlap with their two neighbours. Since the MuCTPI cannot resolve overlaps between sectors belonging to separate MIOCT boards, the fake double-counts originating from these regions have to be dealt with by the TGC muon trigger sub-system. It has been shown that by masking a single strip at the edge of the overlapping sectors, the fake double-count probability can be reduced significantly without a noticeable decrease of the trigger efficiency [65].

7.2 Performance of the Level-1 di-muon triggers

In this section I will summarise the work I have done to create optimal look-up tables for all the 16 MIOCT boards of the MuCTPI, and show the effects of this optimised overlap handling at the Level-1 muon trigger on some rare B-decay channels.

7.2.1 Creating the MuCTPI configuration

The probability of a single muon producing a fake Level-1 di-muon trigger is studied using large samples of single-muon simulations processed by the full ATLAS detector simulation. The relatively little activity caused by a muon in the detector enables a reasonably fast full detector simulation of these events, which makes the production of a few million events relatively simple. A view of such an event in which both a barrel and an end-cap sector detects a single muon can be seen in Figure 7.4.

I have used samples of fully simulated single-muon events as detailed in Table 7.1. I used the full samples available for 6, 7, 10, 12, 15, 21 and 45 GeV to create the optimised LUTs for the MuCTPI. This was done by a dedicated analysis program performing the following sequence:

1. It loops over the samples, looking for events where the Level-1 trigger detected more than one muon. If the multiple muons came from regions where overlap resolution is possible in the MuCTPI, it saves the sector

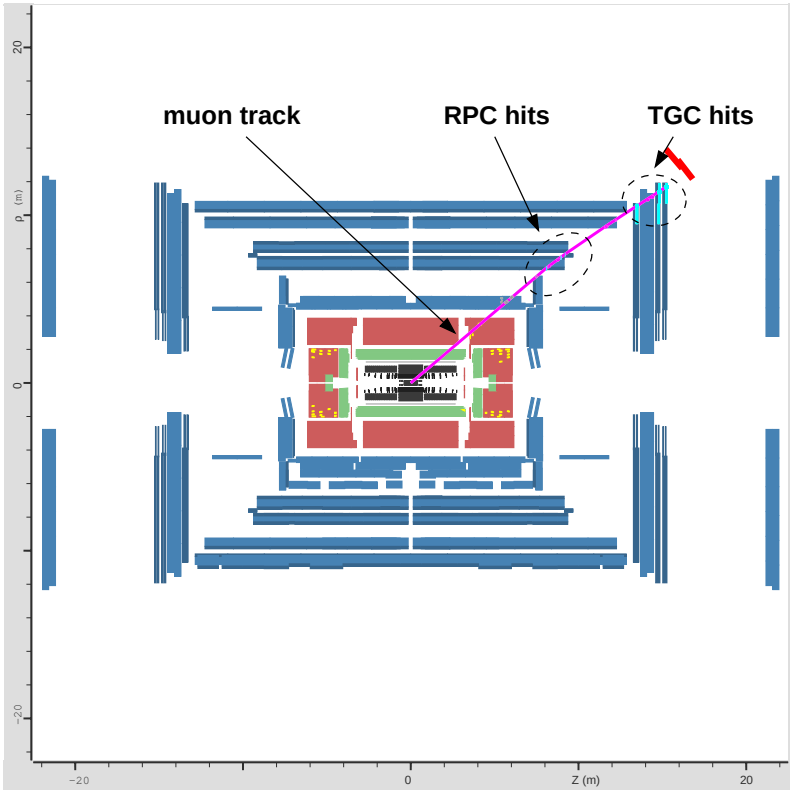

Figure 7.4: View of a simulated event with a single muon having a p_{T} of 6 GeV.

and RoI combination for which the fake double-count happened. The code counts how many times a given sector-RoI combination occured.

2. After all events have been processed, the combinations which should be considered in the overlap removal are selected by finding the combination with the highest probability and accepting all combinations that have a probability larger than some fraction of the maximal probability.

3. The combinations that are supposed to be considered in the overlap handling, are written out into a single XML file in a format that follows the look-up table logic of the MuCTPI hardware.

Step 2 takes care of removing low-probability overlaps from the LUTs and avoiding overtraining. The resulting XML file can directly be read by the offline and stand-alone simulations of the MuCTPI hardware – used in this analysis. The tuning of the LUTs can be done by adjusting the cuts in

p_{T} [GeV]	2.0	2.5	3.0	3.5	4.0	4.5	5.0	6.0
# of events	340k	390k	130k	330k	180k	290k	160k	140k

p_{T} [GeV]	7.0	9.0	10.0	12.0	13.0	15.0	17.0	19.0
# of events	90k	190k	140k	90k	180k	50k	160k	150k

p_{T} [GeV]	21.0	22.0	26.0	28.0	30.0	32.0	34.0	36.0
# of events	130k	40k	90k	90k	90k	90k	70k	90k

p_{T} [GeV]	45.0	50.0
# of events	90k	80k

Table 7.1: Samples of single-muon simulations used in the analysis.

step 2. By raising these cuts, only the most probable sector-RoI combinations are kept which increases the di-muon trigger efficiency, but also increases the fake di-muon trigger rate. Lowering the cut values increases the size of the LUTs, decreasing the fake di-muon trigger rate, but also possibly decreasing the trigger efficiency for real di-muon signatures.

The cuts in step 2 were set such that any sector-RoI combination with an overlap probability larger than 10% of the probability of the most probable combination of the respective kind (barrel–barrel, barrel–end-cap, etc.) was retained. Keeping more combinations would have resulted in too large LUTs that the hardware could not have handled, but as it will be shown in Section 7.3, this configuration did not introduce a noticeable effect in the di-muon trigger efficiency.

7.2.2 Fake di-muon trigger rate from single muons

Using the reference LUTs created by the program described above, the fake di-muon trigger probabilities were evaluated. I define the fake trigger probability as follows:

$$P_{\mathrm{fake}} = \frac{\text{Number of events with more than one muon detected}}{\text{Number of events with a triggered muon}} \tag{7.1}$$

The numbers in the numerator and the denominator correspond to muons passing the same Level-1 muon trigger threshold. I assign a fake probability

for each sector overlap type listed in Section 7.1, which means there are 4 different kinds of fake double-counts in my analysis:

- Barrel–Barrel double counts (BB): When a single muon is detected by two overlapping RPC sectors.
- Barrel–End-cap double counts (BE): When a single muon is detected by an overlapping RPC–TGC sector pair.
- End-cap–End-cap double counts (EE): When a single muon is detected by two overlapping "End-cap" TGC sectors.
- Forward–Forward double counts (FF): When a single muon is detected by two overlapping "Forward" TGC sectors.

Each of these fake double-count types have been evaluated separately. The analysis used the full single-muon data samples summarised in Table 7.1. The effect of the MuCTPI's overlap handling is demonstrated in Figure 7.5 a) and b). The figures show the Barrel–End-cap fake double count probability for the six "nominal" di-muon trigger items in case the muon was detected by the barrel, for muons with transverse momenta between 2 and 50 GeV.

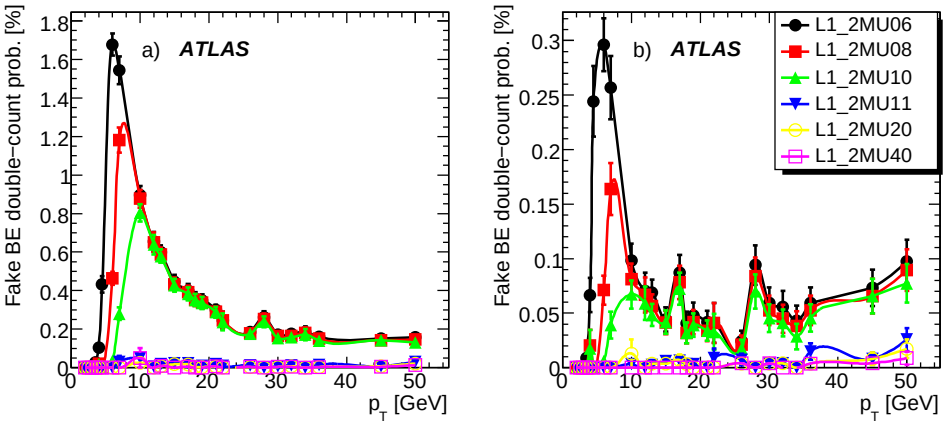

Figure 7.5: Barrel–End-cap fake di-muon trigger probabilities for various Level-1 di-muon trigger items without (a) and with (b) using the overlap handling of the MuCTPI.

As can be seen in Figure 7.5, the fake trigger probabilities are not uniform in p_{T}. In order to make a good estimation of the rate of these fake triggers, this p_{T} dependence has to be taken into account. The detailed probabilities for 6 and 20 GeV muons to cause fake di-muon triggers without using the overlap handling of the MuCTPI, for all available Level-1 muon thresholds can be seen in Table 7.2.

p_T [GeV]	BB prob. [%]	BE prob. [%]	EE prob. [%]	FF prob. [%]
Fake L1_2MU4 probability				
6.0	1.56 ± 0.07	1.39 ± 0.08	1.00 ± 0.07	0.81 ± 0.06
20.0	1.43 ± 0.06	0.13 ± 0.02	0.49 ± 0.05	0.55 ± 0.05
Fake L1_2MU5 probability				
6.0	1.14 ± 0.06	1.17 ± 0.07	0.40 ± 0.05	0.56 ± 0.06
20.0	1.43 ± 0.06	0.13 ± 0.02	0.49 ± 0.05	0.55 ± 0.05
Fake L1_2MU6 probability				
6.0	1.11 ± 0.05	0.97 ± 0.06	0.39 ± 0.04	0.55 ± 0.05
20.0	1.43 ± 0.06	0.13 ± 0.02	0.49 ± 0.05	0.55 ± 0.05
Fake L1_2MU8 probability				
6.0	0.87 ± 0.05	0.38 ± 0.06	0.31 ± 0.05	0.58 ± 0.07
20.0	1.33 ± 0.06	0.10 ± 0.02	0.42 ± 0.05	0.45 ± 0.05
Fake L1_2MU10 probability				
6.0	0.68 ± 0.05	0.12 ± 0.08	0.21 ± 0.09	0.54 ± 0.13
20.0	1.26 ± 0.06	0.10 ± 0.02	0.36 ± 0.04	0.36 ± 0.04
Fake L1_2MU11 probability				
6.0	0.43 ± 0.21	0.00 ± 0.00	0.32 ± 0.15	0.42 ± 0.16
20.0	0.86 ± 0.05	0.00 ± 0.00	0.33 ± 0.04	0.32 ± 0.04
Fake L1_2MU20 probability				
6.0	0.28 ± 0.28	0.00 ± 0.00	0.48 ± 0.34	0.00 ± 0.00
20.0	0.75 ± 0.05	0.00 ± 0.00	0.24 ± 0.03	0.18 ± 0.03
Fake L1_2MU40 probability				
6.0	0.42 ± 0.42	0.00 ± 0.00	0.00 ± 0.00	0.00 ± 0.00
20.0	0.49 ± 0.04	0.00 ± 0.00	0.08 ± 0.03	0.08 ± 0.03

Table 7.2: Probabilities for single muons with transverse momenta 6 and 20 GeV that caused a single muon trigger, to also cause a fake di-muon signature. (Without using the overlap handling of the MuCTPI.)

Single muon trigger rate calculation

The single muon trigger rates are esimated from the muon trigger efficiencies calculated using single-muon simulations, and the theoretical cross sections for

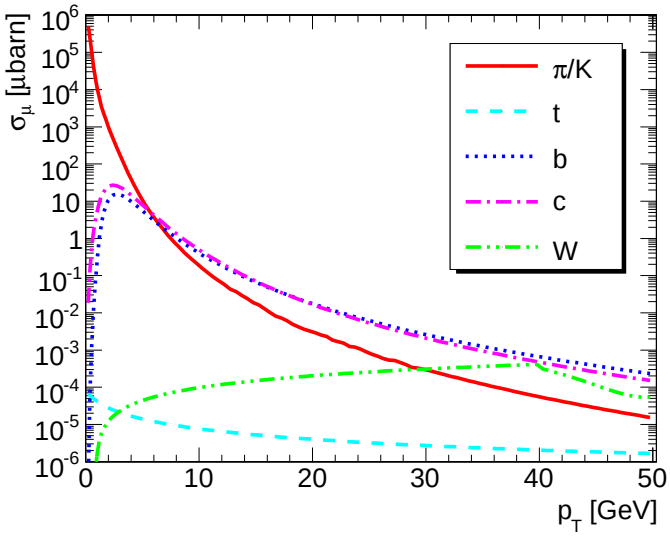

Figure 7.6: Inclusive muon production cross sections at the LHC from different processes. All cross sections are integrated for the full η coverage of the ATLAS Level-1 muon detectors. (References to the calculations are presented in [65].)

inclusive muon production at the LHC. The cross section of inclusive muon production from different processes at 14 TeV proton–proton collissions for $\eta < 2.4$ are shown in Figure 7.6. As it can be seen from the plot, the largest contributors to inclusive muon production are the processes involving the creation of a pion or kaon (which subsequently decay to a muon), a b or a c quark.

All the calculations presented here go up to 50 GeV in muon transverse momenta. The calculations show that the trigger rates coming from muons that have a p_{T} larger than 50 GeV are much smaller than the uncerainties in the cross sections at low-p_{T} – which are responsible for the largest part of the rates –, and are hence neglected.

Because of fundamental differences in the muon detectors, the muon spectrometer has been split into 4 regions for the trigger rate calculations, as these regions show different trigger efficiency curves. The trigger rates in the 4 η regions are calculated separately and their contributions are added up. The single muon trigger rate in one region for a certain trigger item is calculated using the following formula:

$$R = \mathcal{L} \int_{p_T^{cutoff}}^{p_T^{inf}} \sigma_\mu(p_T)\epsilon(p_T)dp_T, \tag{7.2}$$

where $\mathcal{L}$ is the instantaneous luminosity of the accelerator, and ϵ is the Level-1 trigger efficiency. As detailed previously, p_T^{inf} is effectively 50 GeV in the calculations. p_T^{cutoff} was chosen to be 2 GeV as the trigger efficiency for muons below this transverse momentum is practically zero, they do not have enough energy to reach the muon spectrometer.

Detailed calculations for the single muon trigger rates at all levels of the ATLAS muon trigger can be found in [65].

Fake di-muon trigger rate calculation

To calculate the fake di-muon trigger rates coming from inclusive muon production, a modified version of the code for calculating the single muon trigger rates was used. The fake di-muon trigger probabilities were calculated in the same η regions used in the trigger rate calculation. Hence these probabilities can easily be folded into Equation 7.2:

$$R_{\text{fake}} = \mathcal{L} \int_{p_T^{cutoff}}^{p_T^{inf}} \sigma_\mu(p_T)\epsilon(p_T)P_{\text{fake}}dp_T. \tag{7.3}$$

In the actual calculations – for the sake of simplicity – the fake di-muon trigger probabilities have been linearly interpolated for the muon p_{T} values where no exact measurement was available. The fake Level-1 di-muon trigger rates coming from different areas of the detector are collected in Table 7.3. Of course the fake rate increases as we lower the thresholds on the muons, as can be nicely seen in the table. It is also obvious that the majority of the fake di-muon triggers with the current optimisation is caused by the barrel muon detector sectors.

7.3 Level-1 di-muon triggers for $B_s \to \mu^+\mu^-\phi$

The branching ratios of the rare B decay channels will most easily be determined from their relative difference from known decays. For the $B_s \to \mu^+\mu^-\phi$ channel one can use the $B^+ \to J/\psi(\mu^+\mu^-)K^+$ channel as reference, using the

Trigger item	BB rate [Hz]	BE rate [Hz]	EE rate [Hz]	FF rate [Hz]	Total fake rate [Hz]
L1_2MU04	1846.6 ± 119.2	271.6 ± 14.1	136.2 ± 24.5	69.2 ± 12.3	2323.7 ± 123.1
L1_2MU05	243.9 ± 13.0	203.1 ± 10.6	35.3 ± 10.5	33.3 ± 6.5	515.5 ± 20.8
L1_2MU06	193.9 ± 12.4	82.6 ± 7.1	24.6 ± 6.0	24.7 ± 4.7	325.7 ± 16.2
L1_2MU08	114.1 ± 9.8	16.1 ± 2.1	9.7 ± 3.0	12.4 ± 3.3	152.3 ± 11.0
L1_2MU10	79.2 ± 8.0	4.9 ± 1.2	4.8 ± 2.2	5.5 ± 2.0	94.4 ± 8.6
L1_2MU11	11.7 ± 1.8	0.1 ± 0.1	3.9 ± 2.0	4.5 ± 1.8	20.1 ± 3.2
L1_2MU20	2.4 ± 0.4	0.1 ± 0.0	2.4 ± 1.9	0.7 ± 0.5	5.5 ± 2.0
L1_2MU40	0.8 ± 0.1	0.0 ± 0.0	1.7 ± 1.7	0.1 ± 0.1	2.6 ± 1.7

Table 7.3: Rates of different kinds of fake Level-1 di-muon triggers at $\mathcal{L} = 10^{33}$ cm^{-2}s^{-1}.

$$BR(B_s \to \mu^+\mu^-\phi) = \frac{N^{\rm obs}_{B_s}}{\alpha_{B_s} \cdot \epsilon^{\rm total}_{B_s}} \cdot \frac{\alpha_{B^+} \cdot \epsilon^{\rm total}_{B^+}}{N^{\rm obs}_{B^+}} \cdot \frac{f_u}{f_s} \cdot BR(B^+ \to J/\psi K^+) \cdot BR(J/\psi \to \mu^+\mu^-) \quad (7.4)$$

formula [66], where $N^{\rm obs}_x$ is the number of respective candidates observed, α_x is the geometrical and kinematic acceptance for the channel, $\epsilon^{\rm total}_x$ is the total event selection efficiency including trigger, offline reconstruction and analysis selection, and f_u/f_s accounts for the different b quark fragmentation probabilities. It is very important in these analyses to understand and control all biases introduced by the event selection. Biases are evaluated from Monte Carlo simulations and will be validated with experimental data of known physics processes.

First I describe the datasets under investigation in Section 7.3.1. Section 7.3.2 presents the Level-1 single- and di-muon trigger efficiencies for this channel using various $p_{\rm T}$ thresholds. Section 7.3.3 then gives details on the bias introduced by the Level-1 di-muon trigger as a function of the opening angle between the muons in the final state.

7.3.1 About the dataset

The process under analysis was simulated with the PYTHIA Monte-Carlo generator [67] using the PythiaB interface [68] developed for ATLAS. In the simulation, the following branching ratios were used: $Br(B_s \to \mu^+\mu^-\phi) = 1 \times 10^{-6}$, with $Br(\phi \to K^+K^-) = 0.492$. Each generated event was required to have two muons, one with $p_{\rm T} > 4$ GeV and the other with $p_{\rm T} > 6$ GeV. The total cross section of the simulated process after the generator cuts was calculated to be 0.57 pb. I have analysed a total of 34400 fully simulated and reconstructed events, representing about 19.6 fb^{-1} of collected integrated luminosity. (About 2 years of data at "low" luminosity.)

7.3.2 Trigger efficiencies for various configurations

The overall Level-1 muon trigger efficiencies were tested for multiple configurations on the previously descibed B signal and control samples. Table 7.4 shows the trigger efficiencies with respect to the generated events for the $B_s \to \mu^+\mu^-\phi$ and $B^+ \to J/\psi(\mu^+\mu^-)K^+$ processes.

The MuCTPI's overlap removal does not affect the single-muon trigger efficiencies, hence the respective table cells are empty. An efficiency reduction due to the usage of overlap removal can be observed systematically for all channels and trigger items, but it is of the order of the statistical uncertainty of the analysis. As the next section will show, this reduction is mainly an

	Efficiency [%]	
Trigger item	w/o overlap removal	with overlap removal
$B_s \to \mu^+\mu^-\phi$		
L1_MU04	97.0 ± 0.1	—
L1_MU06	93.1 ± 0.1	—
L1_2MU04	69.4 ± 0.2	69.0 ± 0.2
L1_2MU06	53.7 ± 0.2	53.2 ± 0.2
$B^+ \to J/\psi(\mu^+\mu^-)K^+$		
L1_MU04	96.8 ± 0.1	—
L1_MU06	92.9 ± 0.1	—
L1_2MU04	69.1 ± 0.2	68.8 ± 0.2
L1_2MU06	53.4 ± 0.2	52.9 ± 0.2

Table 7.4: Absolute Level-1 muon trigger efficiencies for the $B_s \to \mu^+\mu^-\phi$ and $B^+ \to J/\psi(\mu^+\mu^-)K^+$ channels with respect to all the generated events.

effect coming from events where the Level-1 muon trigger detected one of the simulated muons twice while missing the other one. Hence the decrease is not a fault of the overlap removal, but of the muon trigger coverage.

Although the low-p_{T} single-muon triggers are clearly much more efficient than the di-muon triggers, these will only be usable at initial, low luminosities of the accelerator. At higher luminosities the trigger rate can be reduced by several orders of magnitude by switching to the di-muon triggers, while still keeping an acceptable efficiency.

7.3.3 Opening angle dependency

In case of studying some quantity as a function of a certain parameter x, one must ensure that the trigger efficiency is independent of the parameter x or correct for the efficiency to avoid a bias from the trigger. Many analyses will use various angular distributions of the muons for their calculations. It is therefore very important to fully control any bias that the trigger may have on these distributions.

Figure 7.7 a) and b) show the L1_2MU04 and L1_2MU06 trigger efficiencies as a function of the opening angle[1], ΔR, between the two *leading muons* in $B_s \to \mu^+\mu^-\phi$ events. The leading muons are the two muons with the high-

[1] ΔR is calculated as $\sqrt{\Delta\eta^2 + \Delta\phi^2}$, where $\Delta\eta$ and $\Delta\phi$ are the pseudorapidity and azimuth angle differences between the two 4-momentum vectors.

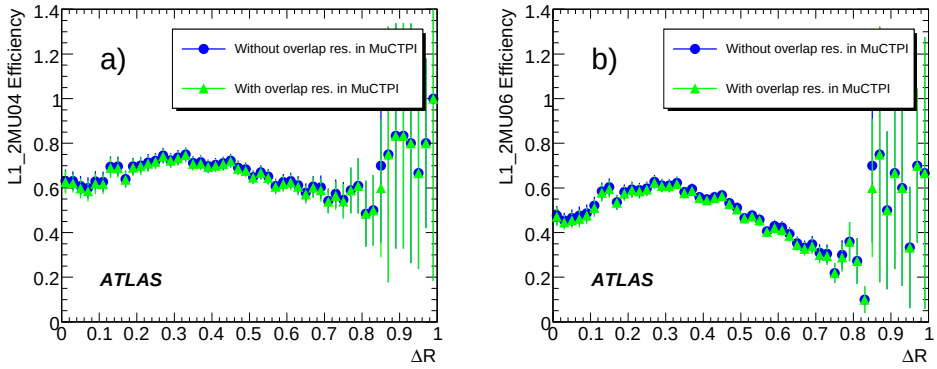

Figure 7.7: Trigger efficiency as a function of ΔR in the semi-leptonic rare B decay $B_s \to \mu^+\mu^-\phi$ using the L1_2MU04 (a) and L1_2MU06 (b) triggers.

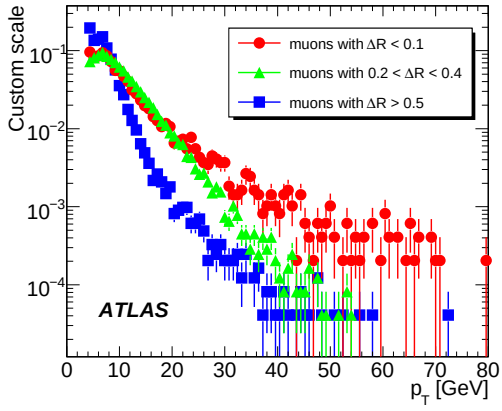

Figure 7.8: The simulated p_{T} distribution of the two leading muons with different opening angles in the ΔR ranges: $\Delta\mathrm{R} < 0.1$ (circle), $0.2 < \Delta\mathrm{R} < 0.4$ (triangle) and $\Delta\mathrm{R} > 0.5$ (rectangle) on $B_s \to \mu^+\mu^-\phi$ events.

est transverse momentum in the Monte Carlo record. No offline selection is applied to see the bias only from the Level-1 trigger.

The trigger efficiency clearly depends on the opening angle of the leading muons. Since overlap removal between the muon candidates does not play a role at large opening angles, this effect is purely kinematic. The $m(B_s) - m(\phi)$ mass difference determines the p_{T} spectrum of the muons coming from the decay at different opening angles. Figure 7.8 shows the p_{T} distribution of the leading muons for three different ΔR ranges of $\Delta\mathrm{R} < 0.1$, $0.2 < \Delta\mathrm{R} < 0.4$ and $\Delta\mathrm{R} > 0.5$. The muons at large opening angles clearly have a softer p_{T} distribution.

The effect is even more clearly visible for higher threshold di-muon trigger items, as the probability of having muons at large ΔR with transverse momenta high enough to trigger a high threshold di-muon trigger item is very small, but non-negligible at small opening angles.

The small efficiency loss in Figure 7.7 at very small opening angles is however due to the trigger system. In the case that the muons both leave hits in the same RoI, only one muon can be triggered by the system. The effect of turning the overlap handling in the MuCTPI on or off is negligible compared to the effects discussed previously, and is below our current statistical uncertainty.

7.4 Conclusions

It will be possible to study some B-physics processes at the LHC with the ATLAS detector even at the highest designed luminosities. The precise measurement of the branching ratios of rare decays of the B mesons could provide a good tool for finding proof of the existence of physics beyond the Standard Model.

The ATLAS trigger system will have to be set up carefully to select events with two low-p_{T} muons in their final states, as the overlaps between the muon trigger sectors can produce fake di-muon trigger signatures. In this chapter I demonstrated that it is possible to reduce the rate of such fake di-muon events by about 70% using the overlap handling of the MuCTPI alone. I also demonstrated on a selected rare B_s meson decay that the overlap handling in the Level-1 trigger has no unforeseen effects on the trigger efficiency.

CHAPTER 8

Muon triggers for top physics in ATLAS

As shown in Section 5.2, the LHC will provide its experiments with an unprecedented number of $t\bar{t}$ pairs. It is very important to use efficient triggers that are well understood to select these events. The first cross section measurements will need precise trigger efficiency calculations from early on.

It is possible to efficiently select semi-leptonic $t\bar{t}$ decays – where one of the W-bosons decays to an electron or a muon – with the single-lepton triggers of ATLAS. This is made possible by the hard p_{T} spectrum of the leptons coming from the W decays, as demonstrated in Figure 8.1.

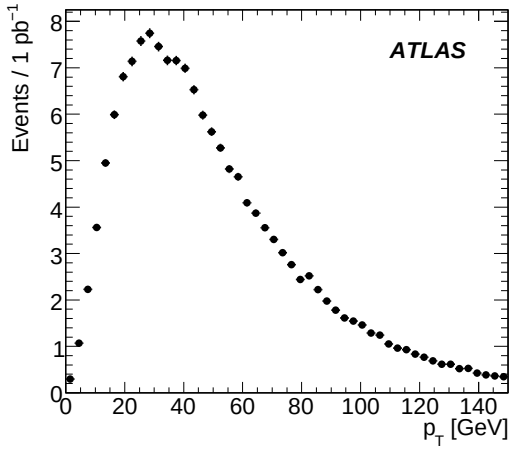

Figure 8.1: p_{T} spectrum of simulated muons from $W \to \mu\nu$ decays in semi-leptonic $t\bar{t}$ events. The distribution is scaled to correspond to an integrated luminosity of 1 pb^{-1}.

In this chapter the efficiency of the whole chain of muon triggers in ATLAS – both Level-1 and HLT – is presented for semi-leptonic $t\bar{t}$ events. Subsequently an example $t\bar{t}$ production cross section analysis is presented which utilises these trigger efficiencies.

8.1 Monte Carlo samples

The analysis used about 600k fully simulated semi-leptonic $t\bar{t}$ events – representing a total integrated luminosity of 945.6 pb^{-1}. About one third of the events has a W decaying to an electron, one third has it decaying to a muon and one third has it decaying to a tau particle. There is also a small percentage of fully leptonic $t\bar{t}$ decay events in the sample following the decay branching ratio of the unfiltered W. Throughout this chapter I am going to refer to the $t\bar{t}$ events where one of the W-s decays to a muon as semi-muonic events.

The most important background to $t\bar{t}$ production at the LHC are the processes with real leptons coming from W decays, with additional jets in the event. These are commonly referred to as W + jet events. In my analysis I used about 22k fully simulated W + jet events in which the W decays to a muon. These events represent a total integrated luminosity of 686.5 pb^{-1}.

8.2 Muon trigger configuration

The Level-1 trigger simulation used the standard single-muon trigger items on the samples, which are: L1_MU06, L1_MU08, L1_MU10, L1_MU11, L1_MU20 and L1_MU40.

As shown in Section 6.3.3, the single-muon High Level Trigger of ATLAS runs 3 consecutive "hypothesis" algorithms that implement the event selection. All these algorithms apply cuts only on the reconstructed transverse momentum of the muon that was found. The p_{T} cuts used for this analysis are listed in Table 8.1 for the *mu06*, *mu20i* and *mu40i* trigger chains. There is currently no optimised *mu40i* trigger implemented for ATLAS, the cuts chosen for this analysis are only educated guesses of how such a trigger item could be implemented.

8.3 Overall muon trigger efficiencies

The efficiency of each Level-1 item to trigger on a $t\bar{t}$ event is shown in Figure 8.2 a). Here the efficiency is calculated with respect to the total number of simulated semi-muonic events in the $t\bar{t}$ sample. It can be seen that the high-p_{T} Level-1 single muon triggers provide high efficiency for selecting the events.

Signature	MufastHypo [GeV]	MucombHypo [GeV]	TrigMooreHypo [GeV]
mu06	5.49	5.83	6.0
mu20i	18.95	19.33	20.0
mu40i	36.0	38.0	40.0

Table 8.1: Selection cuts applied by the muon HLT hypothesis algorithms.

When running at an increased luminosity (10^{34} cm^{-2}s^{-1}), the threshold can easily be raised to 40 GeV without an unacceptable loss in efficiency.

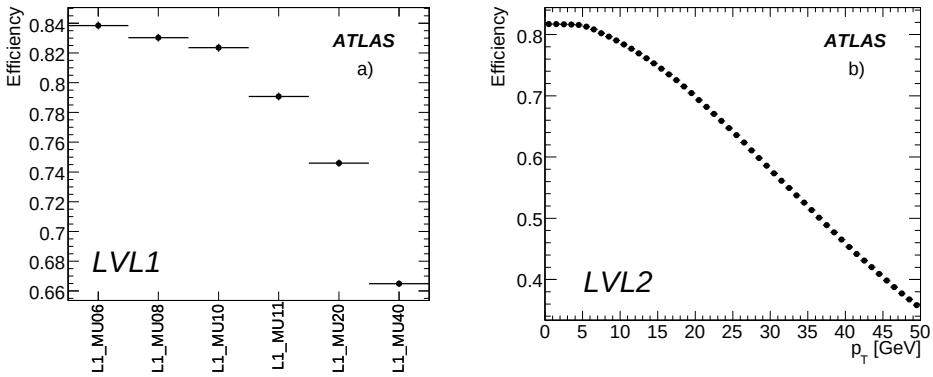

Figure 8.2: Efficiency of the single muon Level-1 (a) and Level-2 (b) trigger item as a function of the used Level-1 thresholds and Level-2 p_{T} cut applied by the MucombHypo hypothesis algorithm respectively.

Figure 8.2 b) shows the absolute efficiency of the Level-2 single muon trigger, in case of the HLT chain being started by a muon RoI passing the MU06 threshold. The p_{T} cut applied by the `MucombHypo` algorithm is shown on the horizontal axis. Figure 8.3 shows similar efficiencies when the EF chain is started by a LVL2 muon candidate fulfilling the *mu06* signature. The p_{T} cut applied by the `TrigMooreHypo` algorithm is shown on the horizontal axis.

The absolute trigger efficiency for the HLT cannot be read directly from these plots, however. The Level-2 *mu20i* processing will only be initiated by Level-1 RoIs which fulfill the L1_MU20 requirements. The efficiency for each trigger level, normalised to the number of simulated semi-muonic events have been calculated for a few trigger signatures. These are shown in Table 8.2.

Comparing Table 8.2 with Figure 8.2 b) and 8.3, one can see that the differences are small, indicating that the figures can be used to accurately estimate the effects of a change in the trigger thresholds.

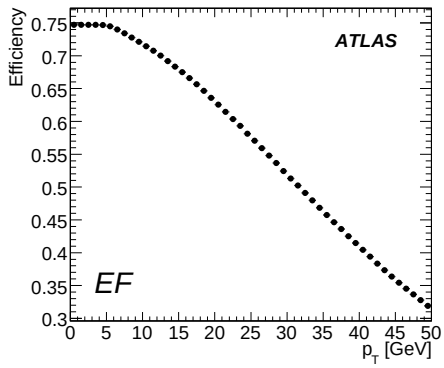

Figure 8.3: Efficiency of the single muon Event-Filter trigger item as a function of the p_{T} cut applied by the TrigMooreHypo algorithm.

Trigger chain name	Level-1 Eff. [%]	Level-2 Eff. [%]	Event-Filter Eff. [%]
mu06	83.7	80.0	72.9
mu20i	74.5	66.1	58.7
mu40i	66.3	43.1	36.0

Table 8.2: Efficiencies of the standard *mu06* and *mu20i* trigger chains, together with those of a theoretical *mu40i* chain on simulated semi-muonic $t\bar{t}$ events.

8.4 Differential muon trigger efficiencies

One can also determine the efficiency of the trigger to detect a single muon with a given p_{T} in $t\bar{t}$ events and produce so called turn-on curves. For this one has to execute a matching between the simulated and the trigger muons. At this time the best method for matching a trigger muon to a simulated muon is based on their η and ϕ coordinates at the interaction point.

8.4.1 Muon trigger turn-on curves in $t\bar{t}$ events

A Level-1 muon is matched to a simulated or reconstructed muon if its ΔR distance from the muon is smaller than 0.15. Figures 8.4 a) and b) show the efficiency of a simulated muon, with a p_{T} as indicated on the horizontal axis, to pass the L1_MU06 and L1_MU20 triggers, respectively. Figure 8.4 b) also shows the trigger efficiency for a reconstructed muon with a p_{T} as indicated on the horizontal axis. The efficiency to trigger a muon that has been identified by the reconstruction is slightly higher, just as one would expect. It can also be seen, that the plateau efficiency to trigger on high-p_{T} muons with the

L1_MU20 trigger is a little lower than to trigger on them with the L1_MU06 trigger. This is easily understood taking into account that the RPC sector logic only requires a coincidence between two detector stations for the L1_MU06 trigger, but they require a coincidence between three stations for the L1_MU20 trigger.

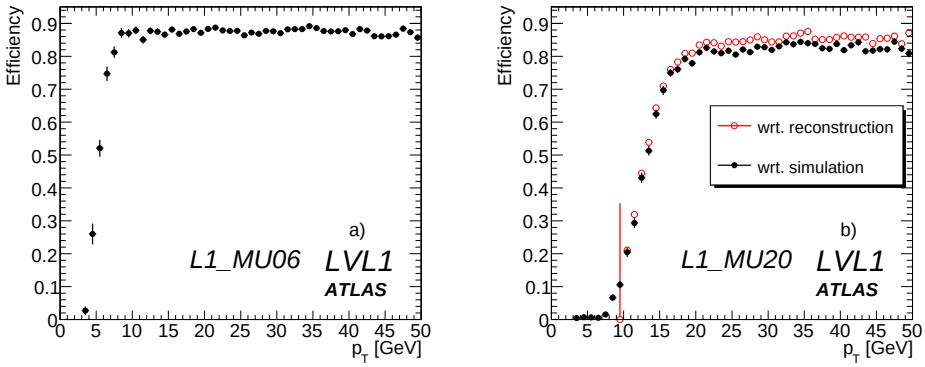

Figure 8.4: Level-1 trigger efficiencies as a function of the p_T of the simulated or reconstructed muon. The trigger efficiency with respect to reconstruction is only shown for L1_MU20, since reconstructed muons with a p_T lower than 10 GeV were not included in my analysis.

The plateau of the efficiency is around 80% in both cases, which is mostly due to the deficiencies in muon trigger detector coverage. The trigger efficiency stays flat above 50 GeV up to a muon transverse momentum of about 1 TeV.

Figures 8.5 a) and b) show the relative efficiency of the Level-2 muon trigger for the L2_mu06 and L2_mu20 trigger items. The efficiency on the plateau is near 100%, implying that few muons identified at Level-1 are missed at Level-2. The efficiency curves with respect to simulated and reconstructed muons are very similar, which is also understandable from the high efficiency of the Level-2 muon trigger. At the same time the curves are much sharper around the threshold energies, which shows that much more precise p_T estimation is possible at Level-2 than at Level-1.

Similarly, Figures 8.6 a) and b) show the relative efficiency of the Event-Filter single muon triggers, EF_mu06 and EF_mu20 as a function of the p_T of the simulated and reconstructed muons. The turn-on curve is the sharpest at this level. The EF_mu20 efficiency is larger on the plateau with respect to reconstructed muons. The Event-Filter reconstruction uses much of the same tools and algorithms which are used in the offline reconstruction which are known to be less efficient in identifying muons than Level-2, so this separation is also understandable.

The Event-Filter uses the most strict reconstruction of muons, which

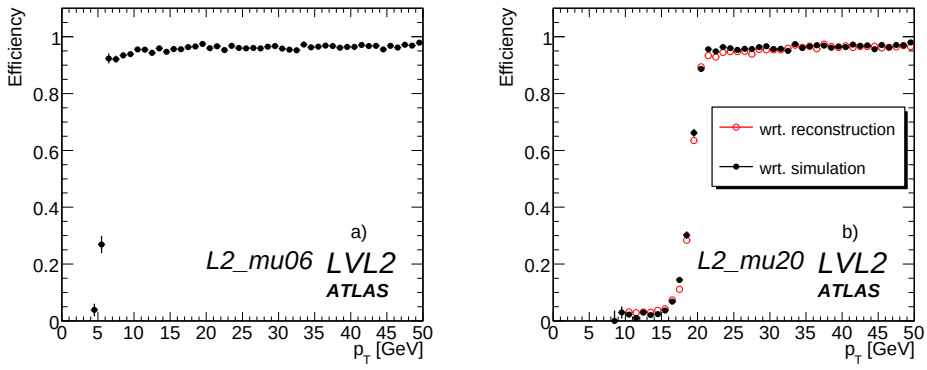

Figure 8.5: Level-2 trigger efficiencies as a function of the p_{T} of the simulated or reconstructed muon. The trigger efficiency with respect to reconstruction is only shown for L2_mu20, since reconstructed muons with a p_{T} lower than 10 GeV were not included in my analysis.

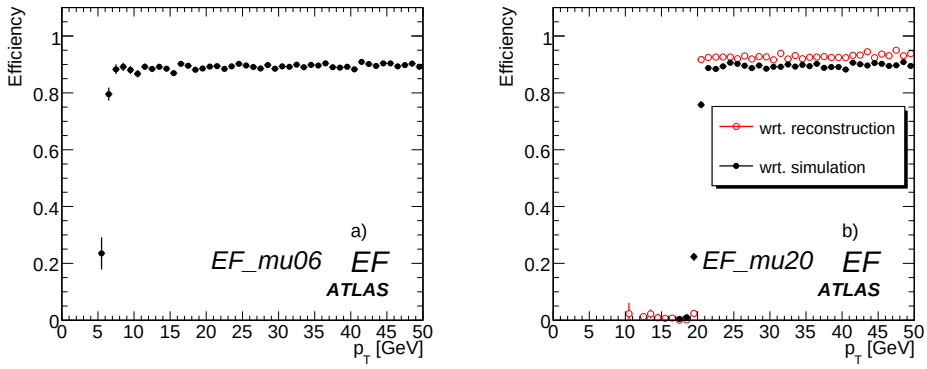

Figure 8.6: Event-Filter trigger efficiencies as a function of the p_{T} of the simulated or reconstructed muon. The trigger efficiency with respect to reconstruction is only shown for EF_mu20, since reconstructed muons with a p_{T} lower than 10 GeV were not included in my analysis.

leads to decreases in reconstruction efficiency in certain detector parts. This is demonstrated in more detail in the next section.

As can be seen from Figure 8.4 b), the L1_MU20 trigger efficiency does not reach its plateau fully for reconstructed muons with $p_{\mathrm{T}} = 20$ GeV. For this reason the offline muons that I will use in Section 8.5 have to have a p_{T} of at least 25 GeV. The absolute trigger efficiencies for events that have a muon with $p_{\mathrm{T}} > 25$ GeV are listed in Table 8.3 for all trigger levels for the *mu20i* trigger chain.

Trigger chain name	Level-1 Eff. [%]	Level-2 Eff. [%]	Event-Filter Eff. [%]
Relative to previous level			
mu20i	84.34	94.79	92.07
Absolute			
mu20i	84.34	79.94	73.60

Table 8.3: Efficiencies of the standard *mu20i* trigger chain, on $t\bar{t}$ events with a reconstructed muon with $p_{\mathrm{T}} > 25$ GeV.

8.4.2 Angular muon trigger efficiencies in $t\bar{t}$ events

One can also show the efficiency as a function of the direction of the reconstructed muon. Figure 8.7 a) shows the efficiency to trigger the L1_MU20 trigger item, as a function of the η coordinate of the muon. Similarly Figure 8.7 b) shows the efficiency as a function of the ϕ coordinate. The Level-1 trigger efficiency is not uniform in the detector. The barrel, covering the range $|\eta| < 1.05$, displays areas of greatly reduced efficiency, for example at the feet of the detector. The reduction in efficiency can also be seen in ϕ, as shown in Figure 8.7 b), where the feet are visible at ϕ values close to -2 and -1. It has to be noted that with new optimisations of the Level-1 trigger configuration – not available at the time of the Monte Carlo productions for this analysis – improvements were made in making the trigger efficiency more uniform in the end-cap regions ($|\eta| > 1.05$).

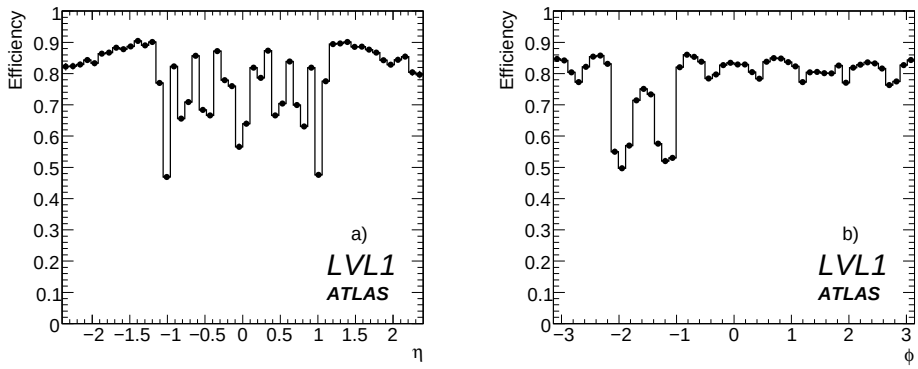

Figure 8.7: Level-1 trigger efficiency as a function of the η (a) and ϕ (b) coordinate of the reconstructed muon for the L1_MU20 trigger item.

The Level-2 trigger efficiencies, relative to Level-1, as a function of the η and ϕ coordinates of the muon can be seen in Figures 8.8 a) and b), re-

spectively. The Level-2 muon reconstruction in the end-caps ($|\eta| > 1.05$) was newly developed for the trigger at the time of creating the $t\bar{t}$ Monte Carlo simulations. For this reason the optimisation of the reconstruction was not yet finalised. This is clearly visible as a loss in efficiency compared to the values in the barrel in Figure 8.8 a). These figures include the efficiency loss due to the p_{T} cut applied at Level-2, causing the efficiency to be lower than the plateau efficiency in Figure 8.5 b).

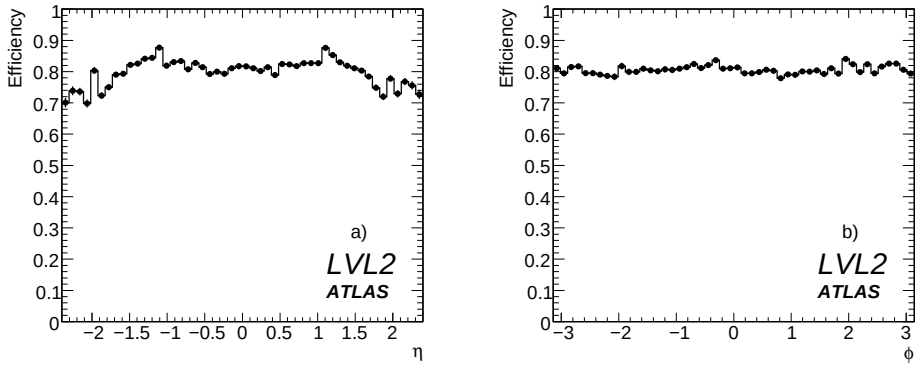

Figure 8.8: Level-2 trigger efficiency as a function of the η (a) and ϕ (b) coordinate of the reconstructed muon for the L2_mu20 trigger item. The efficiency is calculated relative to Level-1.

The Event-Filter trigger efficiencies for the EF_mu20i signature relative to Level-2 are shown in Figures 8.9 a) and b). As detailed previously, the Event-Filter muon reconstruction uses the same algorithms and tools as the offline reconstruction, which results in a close to flat efficiency as a function of the η and ϕ coordinates of the reconstructed muon.

8.5 $t\bar{t}$ production cross section analysis

The top pair production rate at the LHC will be approximately 1 Hz at a luminosity of 10^{33} cm^{-2}s^{-1}. Apart from leading to an extensive investigation of the top sector, top production will also be a significant background to many searches for *New Physics*. Hence the measurement of the top pair production cross section is a very important part of the ATLAS physics programme.

Understanding the trigger is an important part of any cross section analysis at the LHC, just like understanding all the other parts of the event selection process. In this section I present a simple analysis extracting the $t\bar{t}$ production cross section using the trigger efficiencies calculated specifically for my analysis, from so called *streamtest* data. These data sets were produced as part of the ATLAS Computing System Commissioning (CSC) effort to simulate real

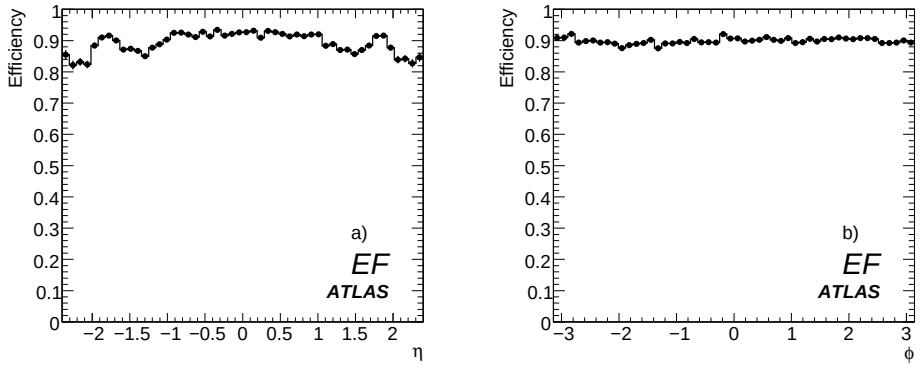

Figure 8.9: Event-Filter trigger efficiency as a function of the η (a) and ϕ (b) coordinate of the reconstructed muon for the EF_mu20 trigger item. The efficiency is calculated relative to Level-2.

data coming from the detector. The data roughly represents the output of 10 half-hour runs of the ATLAS detector in early data-taking (10^{33} cm^{-2}s^{-1}).

This section is not intended as a full cross section analysis, so proper uncertainties on the results will not be discussed. The goal is just to show how trigger efficiency results can be used in a real physics analysis.

8.5.1 Cross section analysis method

I am using the so called *counting method* to calculate the $t\bar{t}$ production cross section. Semi-leptonic $t\bar{t}$ events have a characteristic signature that is easy to select from the data. The $t\bar{t}$ production cross section can then be calculated from the number of events passing our selection with the formula:

$$\sigma_{t\bar{t}} = \frac{N_{\text{sel}} - N_{\text{bkg}}}{\mathcal{L} \cdot A \cdot \varepsilon_{\text{trigger}} \cdot \varepsilon_{\text{reco}} \cdot \varepsilon_{\text{filter}}}, \tag{8.1}$$

where N_{sel} is the number of data events passing all selection criteria, N_{bkg} is the number of background events passing the selection criteria estimated from Monte Carlo, $\mathcal{L}$ is the integrated luminosity of the data sample, A is the acceptance of the detector and $\varepsilon_{\text{trigger}}$, $\varepsilon_{\text{reco}}$ and $\varepsilon_{\text{filter}}$ are the trigger, reconstruction and Monte Carlo filter efficiencies respectively. In the analysis I am going to calculate the acceptance and reconstruction efficiency as one term, ε_{sel}.

8.5.2 Data selection

I used the inclusive muon streaming dataset. This dataset holds all the events from the streaming test that caused a muon trigger to fire. I selected the

L2_mu20 trigger for selecting the semi-muonic $t\bar{t}$ events. The Event-Filter level of the ATLAS trigger was not run on the streaming test data for technical reasons. Because of this, I calculate all trigger efficiencies on the Monte Carlo data up to Level-2. The dataset corresponds to a total integrated luminosity of 15.46 pb^{-1}.

I only used the $t\bar{t}$ and W + jets Monte Carlo data described in Section 8.1 to estimate the effects of my event selection, as it has been shown previously [65] that using my selection criteria, only this type of background is non-negligible.

Object definitions

The event selection uses 3 kinds of reconstructed objects: muons, jets and missing transverse energy. I used the following criteria to select these objects from the reconstruction output:

1. **Muon definition:** A muon is an object reconstructed by the MuID algorithm, and satisfies:

   - $p_{\text{T}} > 25$ GeV
   - $|\eta| < 2.4$

   Only muons that have a ΔR distance greater than 0.3 from a reconstructed jet, are included in the analysis. This suppresses muons coming from K/π decays. The distance between muons and the closest jet is shown in Figure 8.10 for the streamtest dataset.

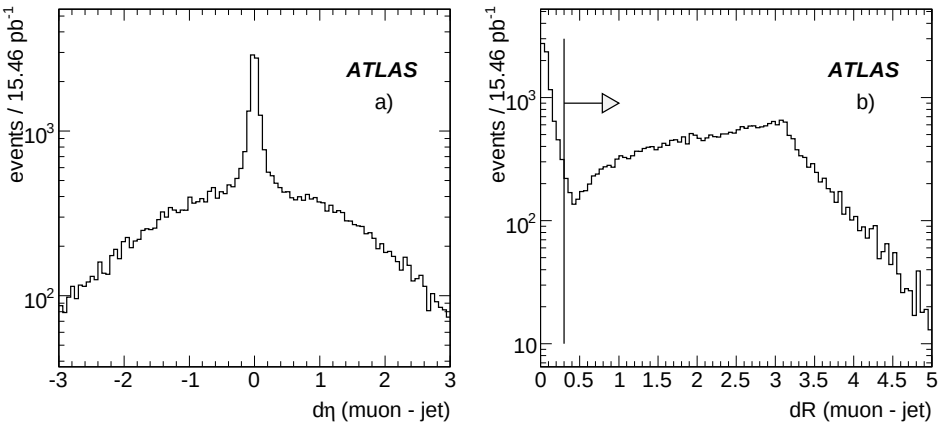

Figure 8.10: Distributions of jet-to-muon distances in η (a), and ΔR (b) before jet-muon overlap removal is performed.

2. **Jet definition:** In the analysis I consider jets reconstructed with the cone algorithm with a radius of 0.4. The jets have to also satisfy:

   - $p_{\mathrm{T}} > 20$ GeV
   - $|\eta| < 2.5$

   Since the analysis does not use electrons or taus, I do not check the overlaps between jets and such objects.

3. **Missing transverse energy definition:** The missing transverse energy used in the analysis is calculated from a sum over specifically calibrated calorimeter cells in 3 categories: cells in electromagnetic clusters, in jets, and in clusters not associated with any reconstructed calorimeter object [59]. This sum is then corrected for the E_{T} of identified muon candidates and for probable energy losses in the cryostat.

Event selection

The following event selection assumes a good understanding of the ATLAS reconstruction, as it uses reconstructed parameters not considered reliable with first data. The following cuts are executed before giving an event to the top reconstruction algorithm detailed later in the section:

- Only events passing the L2_mu20 trigger item are considered.
- The event has to have at least one muon passing the object selection detailed previously. Additionally, this muon also has to be close ($\Delta\mathrm{R} < 0.1$) to a Level-2 muon passing L2_mu20, as this ensures that the trigger efficiency calculation will be correct.
- The missing transverse energy of the event has to be greater than 20 GeV.
- The event has to have at least 4 jets passing the object selection detailed previously.

The number of selected events after each cut is summarised in Table 8.4. The table at first sight suggests that the event selection is performing worse for selecting $t\bar{t}$ events than for selecting W + jet events. Remember however, that the $t\bar{t}$ Monte Carlo contains events where one of the W-s decays to an electron, muon and tau, in the correct mixture (see Table 5.1) – so 2/3 of the events are not targeted by this analysis –, while the W + jets Monte Carlo contains only events where the W decays to a high-p_{T} muon. The events passing these selection criteria are passed to an algorithm reconstructing hadronic top quarks.

Selection cut	Streamtest data		$t\bar{t}$ MC	$W(\mu\nu_\mu)$ + jets MC
	[events]	[%]	[%]	[%]
Full sample	81110	100.0	100.0	100.0
L1_MU20	63236	77.96	35.87	57.06
L2_mu20	54096	66.69	29.75	49.82
Good muon	40860	50.38	20.26	37.52
$\not{E}_{\mathrm{T}}$	33139	40.86	18.48	32.68
4 jets	524	0.65	9.29	18.79

Table 8.4: Event selection flow: The number of events after applying each cut.

8.5.3 Hadronic top quark reconstruction

The hadronically decaying top quark is reconstructed in the following way:

1. Top quark candidates are produced from all 3-jet combinations in the event.

2. The candidates are ordered according to their p_{T}, putting the one with the highest p_{T} first.

3. The candidate with the highest p_{T}, that fulfills the following criteria is selected as the reconstructed top quark:

   - One of the 2-jet combinations from the selected 3 jets has a mass within 10 GeV of the current world-average W mass.
   - Exactly one of the selected jets is b-tagged.

The top quark reconstruction algorithm is run on all the previously selected events. It "accepts" an event if it is able to reconstruct at least one hadronic top quark candidate in it. The efficiencies of the reconstruction are summarised in Table 8.5. As can be seen, the reconstruction rejects most of the W + jets background events, while succeeding with most of the signal events.

Data type	Streamtest data		$t\bar{t}$ MC	W + jets MC
	[events]	[%]	[%]	[%]
Reconstructed top	289	55.15	63.42	8.64

Table 8.5: Hadronic top quark reconstruction statistics on the events selected previously.

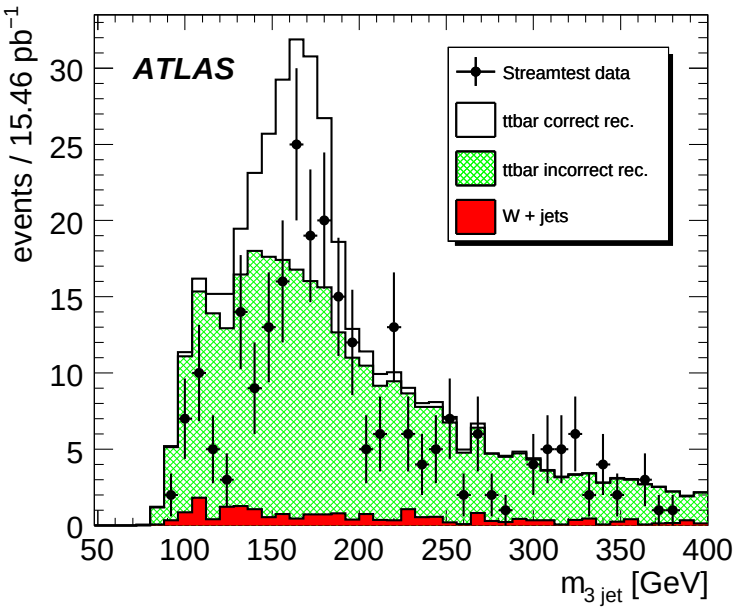

Figure 8.11: Reconstructed top quark mass distribution comparing streamtest data with $t\bar{t}$ and W + jets Monte Carlo.

A plot of the mass distribution of the reconstructed hadronic top quark candidates can be seen in Figure 8.11. It is possible to evaluate on the signal Monte Carlo if the hadronic top quark reconstruction found the correct reconstructed objects to reconstruct the top quark. For this, a matching is performed between the simulated b quark and the light quarks from the W decay and the reconstructed jets.

8.5.4 Cross section

Now I have all the constituents for Formula 8.1. From Table 8.5 $N_{\text{sel}} = 289$. The number of background events after all selection (scaled to the luminosity of the streamtest data set) is $N_{\text{bkg}} = 25.06$. As discussed in Section 8.5.2, the total integrated luminosity of the streaming test data sample is $\mathcal{L} = 15.46$ pb^{-1}. The combined selection efficiency (acceptance, trigger- and reconstruction efficiency) is extracted from Tables 8.4 and 8.5, $\varepsilon_{\text{sel}} = 0.05892$. The Monte Carlo filter efficiency for the semi-leptonic $t\bar{t}$ Monte Carlo can be calculated from the W branching ratios from the PDG values. The filter efficiency is expressed as:

$$\varepsilon_{\text{filter}} = 1 - (1 - br_{\text{lep}})^2 \,, \tag{8.2}$$

where br_{lep} is the branching ratio of a W to decay to a lepton. The filter

efficiency is $\varepsilon_{\text{filter}} = 0.5372$ from this formula. Using these results, I get a total $t\bar{t}$ production cross section of

$$\sigma_{t\bar{t}} = \frac{N_{\text{sel}} - N_{\text{bkg}}}{\mathcal{L} \cdot \varepsilon_{\text{sel}} \cdot \varepsilon_{\text{filter}}} = 539 \pm 33(\text{stat})\ \text{pb} \tag{8.3}$$

from the streamtest dataset. When comparing this result with the theoretical cross section presented in Section 5.2, one can observe a large discrepancy. During the analysis I came to the conclusion that the change in the offline jet reconstruction software between the version used for the reconstruction of the streamtest data and the version used to reconstruct the other Monte Carlos, introduced a discrepancy between the event selection efficiency calculated on the $t\bar{t}$ Monte Carlo and the selection efficiency in the streamtest data. I did however verify that applying the analysis procedure to the $t\bar{t}$ Monte Carlo itself reproduces the correct cross section. Hence the analysis itself is working correctly. As the streamtest data is just another Monte Carlo set employed here to demonstrate the use of the trigger corrections in a cross section measurement, I did not further investigate this discrepancy. For real data rigourous tests will have to be carried out to ensure that the Monte Carlo simulation used to correct the data for detector effects describes the data correctly.

8.6 Conclusions

$t\bar{t}$ events provide very good possibilities for commissioning the ATLAS detector. Because of the high mass of the top quark, these events usually deposit a lot of energy in the detector, producing a lot of particles in jets. The semi-leptonic $t\bar{t}$ events also include a high-p_{T} lepton and missing transverse energy. For this reason, nearly all parts of the ATLAS offline reconstruction can be tested with $t\bar{t}$ events selected from the first data.

As shown in Section 8.3, the high-p_{T} single-muon triggers provide good efficiency for selecting the semi-muonic $t\bar{t}$ events, which makes it possible to select such events even at the highest instantaneous luminosities of the LHC.

The measurement of the $t\bar{t}$ production cross section will be one of the first physics results of ATLAS once it starts to collect data. As shown in Section 8.5, a cross section measurement – with a sizeable uncertainty – will be possible already from a few days of datataking.

Summary

In my thesis I discussed the work I have done in two separate experiments. In the two-photon group of the OPAL collaboration I implemented multiple event selection techniques not used in the group before, for selecting photon–photon interactions in which a jet is produced. I found that the most reliable method for selecting high energy photon–photon events was a likelihood based selection.

Using this event selection method, I measured the inclusive jet production cross section in photon–photon collisions in the data taken between 1998 and 2000 at centre of mass energies $\sqrt{s_{\mathrm{ee}}} = 189 - 209$ GeV that represents a total integrated luminosity of 593 pb^{-1}. The analysis was an extension of a study done previously to determine the same cross section for centre of mass energies $\sqrt{s_{\mathrm{ee}}} = 130 - 136$ GeV. This analysis was motivated by the fact, that the L3 collaboration found in this process an excess in the production cross section at high $p_{\mathrm{T}}^{\mathrm{jet}}$. In my analysis I have found a good agreement between the measurement and the cross section predicted by NLO QCD calculations.

In the second part of my thesis I discussed the work I have done in the trigger group of the ATLAS collaboration. In the trigger group it was my responsibility to develop and maintain the offline simulation of the Muon to Central Trigger Processor Interface (MuCTPI), and using this simulation to help design the final version of the MuCTPI hardware for the ATLAS detector. Among other things, the MuCTPI is responsible for handling the overlaps between the muon trigger chambers, by eliminating fake di-muon trigger signatures in the case when a single muon was detected by multiple trigger sectors. Using the offline simulation, I evaluated the probability that a single muon would generate a fake di-muon trigger signature in the detector for different configurations of the MuCTPI hardware. With the optimal configuration I calculated the expected fake Level-1 di-muon trigger rates, and verified on B-physics samples that the configuration does not degrade the physics performance of the detector.

As a member of the top-physics group of the ATLAS collaboration, I took part in estimating the trigger efficiencies for selecting events with a top quark pair ($t\bar{t}$). I was responsible for calculating the single-muon trigger efficiencies

for various trigger configurations. I have found that the single-muon trigger of ATLAS will be capable of selecting $t\bar{t}$ events with high efficiency throughout the lifetime of the Large Hadron Collider (LHC).

The observation and study of $t\bar{t}$ creation at the LHC will be a very important physics process with initial data. The $t\bar{t}$ decay usually produces high momentum leptons, multiple high energy jets and missing energy in the detector. This makes the decay ideal for testing almost all aspects of the detector. Measuring the $t\bar{t}$ production cross section at 14 TeV centre of mass energy is going to be one of the first physics results of the LHC. In the last section of my thesis I showed how a simple analysis can be executed that extracts the $t\bar{t}$ production cross section from data, using a specially mixed Monte Carlo, mimicking data coming from the detector. I found that even with a few days of data at nominal luminosity (10^{33} cm^{-2}s^{-1}) it is already possible to get a crude measurement of the cross section.

Összefoglalás

A dolgozatomban két különböző kísérletben elvégzett munkámat mutattam be. Az OPAL kollaboráció két-foton csoportjában több olyan új eseményválogatási eljárást hoztam létre foton–foton kölcsönhatások kiválogatására amelyekben hadronzápor (jet) keletkezik, amik korábban nem voltak használatban a csoportban. Úgy találtam, hogy a legmegbízhatóbb eljárás a nagyenergiás foton–foton események kiválogatására egy likelihood alapú válogatás volt.

Ezt az eseményválogatási eljárást felhasználva, meghatároztam az inkluzív jet keletkezési hatáskeresztmetszetet foton–foton ütközésekben az 1998 és 2000 között, $\sqrt{s_{\mathrm{ee}}} = 189 - 209$ GeV tömegközépponti energián gyűjtött adatokban, ami összesen 593 pb^{-1} integrált luminozitásnak felel meg. Az analízis egy korábbinak a kiegészítése volt, ami ugyanezt a hatáskeresztmetszetet vizsgálta $\sqrt{s_{\mathrm{ee}}} = 130 - 136$ GeV tömegközépponti energián. Az analízis abból az okból is érdekes volt, mivel az L3 kollaboráció megnövekedett jet keletkezési hatáskeresztmetszetet talált ebben a folyamatban magas $p_{\mathrm{T}}^{\mathrm{jet}}$ értékeknél. A saját analízisemben jó egyezést találtam a mért hatáskeresztmetszet és az NLO QCD számolások által jósolt eredmények között.

A dolgozatom második részében azt a munkát mutattam be, amit az ATLAS kollaboráció trigger-csoportjában végeztem. Az én feladatom volt a trigger-csoporton belül a "Muon to Central Trigger Processor Interface" (MuCTPI) hardver-elem szimulációjának megírása és karbantartása, és ennek a szimulációnak a felhasználásával én is segítettem az ATLAS detektor végső MuCTPI hardverének megtervezésében. Egyebek mellett a MuCTPI a felelős a trigger kamrák közötti átfedések kezeléséért azzal, hogy kiszűri az olyan hamis két-müon trigger-jeleket, amelyeket egyetlen müon okozott azzal, hogy több trigger-szektorban is jelet hagyott. A szimulációt használva meghatároztam annak a valószínűségét, hogy egyetlen müon hamis két-müon jelet hozzon létre a detektorban a MuCTPI hardver különböző beállításai mellett. Az optimális beallítást használva kiszámoltam a várható hamis, első szintű, két-müon trigger hozamokat, és ellenőriztem B-fizikai mintákon, hogy ez a konfiguráció nem rontja le a detektor fizikai teljesítőképességét.

Az ATLAS kollaboráció top-fizikai csoportjának tagjaként részt vettem

a top kvark párokat ($t\bar{t}$) tartalmazó események kiválasztási trigger-hatásfokainak a meghatározásában. Én voltam a felelős az egy-müon trigger-hatásfokok meghatározásáért különböző trigger-beállítások mellett. Úgy találtam, hogy az ATLAS egy-müon triggere képes lesz nagy hatásfokkal kiválasztani a $t\bar{t}$ eseményeket a Nagy Hadron Ütköztető (LHC) teljes életidején keresztül.

A $t\bar{t}$ keletkezés megfigyelése és vizsgálata az LHC-nél nagyon fontos fizikai folyamat lesz az első adatokkal. A $t\bar{t}$ bomlás általában nagy impulzusú leptonokat, több nagyenergiás hadronzáport és hiányzó energiát hoz létre a detektorban. Ez ideálissá teszi a detektor majdnem minden tulajdonságának ellenőrzéséhez. A $t\bar{t}$ keltés hatáskeresztmetszetének mérése 14 TeV tömegközépponti energián egyike lesz az LHC első fizikai eredményeinek. A dolgozatom utolsó fejezetében bemutattam, hogyan lehet végrehajtani egy egyszerű analízist, amely meghatározza a $t\bar{t}$ keletkezési hatáskeresztmetszetet a gyűjtött adatokból. Ehhez egy speciálisan kevert Monte Carlo-t használtam, ami a detektorból érkező adatokat utánozta. Azt találtam, hogy már néhany napnyi tervezett luminozitás (10^{33} cm^{-2}s^{-1}) melletti adatból durva becslést lehet adni a hatáskeresztmetszetre.

Acknowledgments

I would like to thank first of all my supervisor Prof. Dr. Dezső Horváth for introducing me to particle physics. His help was pivotal in my work in the OPAL collaboration, which in turn led to my involvement in the ATLAS experiment. I would also like to thank my other supervisor, Dr. Thorsten Wengler, for bringing me to the forefront of particle physics. The thesis could not have been completed without his supervision. My sincere thanks goes also to Dr. Nicholas Ellis for providing me with great possibilities for completing my studies, as my group leader in ATLAS. I am greatly indebted to Dr. Aleandro Nisati for helping my work in the muon trigger group in ATLAS, and providing me with valuable consultations.

I owe a big thanks to Dr. Naoko Kanaya and Theodota Lagouri for their involvement in the Level-1 di-muon trigger studies. Their knowledge of the Level-1 muon trigger system of ATLAS helped me to solve a lot of problems. I would also like to express my gratitude toward Dr. Maria Smizanska for the support I got from her in the B-physics group of ATLAS.

I am also grateful to Simon Head and the ATLAS Manchester group in general. The many consultations we had about top quark physics and technical issues of analysing ATLAS data helped me a lot in completing my studies. I am indebted to the people writing the `EventView` code of the ATLAS offline software, for providing me with a lot of great tools for my analyses.

Last but not least, I would like to thank my parents and my sister for their support and encouragement during my years of study and studentship at CERN.

Bibliography

[1] R. Nisius, *"The photon structure from deep inelastic electron photon scattering",* Phys. Rept. **332** (2000) 165 [arXiv:hep-ex/9912049].

[2] P. Kessler, *"Sur une méthode simplifiée de calcul pour les processus relativistes en électrodynamique quantique",* Il Nuovo Cim. **17** (1960) 809.

[3] C. F. von Weizsacker, *"Radiation emitted in collisions of very fast electrons",* Z. Phys. **88** (1934) 612.

[4] E. J. Williams, *"Nature of the high-energy particles of penetrating radiation and status of ionization and radiation formulae",* Phys. Rev. **45** (1934) 729.

[5] S. Jadach, E. Richter-Was, B. F. L. Ward and Z. Was, *"Monte Carlo program BHLUMI-2.01 for Bhabha scattering at low angles with Yennie-Frautschi-Suura exponentiation",* Comput. Phys. Commun. **70** (1992) 305.

[6] S. Jadach, W. Placzek, E. Richter-Was, B. F. L. Ward and Z. Was, *"Upgrade of the Monte Carlo program BHLUMI for Bhabha scattering at low angles to version 4.04",* Comput. Phys. Commun. **102** (1997) 229.

[7] K. Ahmet *et al.* [OPAL Collaboration], *"The OPAL Detector at LEP",* Nucl. Instrum. Meth. A **305** (1991) 275.

[8] M. Arignon *et al.* [OPAL Collaboration], *"The Trigger system of the OPAL experiment at LEP",* Nucl. Instrum. Meth. A **313** (1992) 103.

[9] M. Z. Akrawy *et al.* [OPAL Collaboration], *"Measurement of the cross-sections of the reactions $e^+e^- \to \gamma\gamma$ and $e^+e^- \to \gamma\gamma\gamma$ at LEP",* Phys. Lett. B **257** (1991) 531.

[10] K. Ackerstaff *et al.* [OPAL Collaboration], *"Inclusive Jet Production in Photon–Photon Collisions at $\sqrt{s_{ee}}$ = 130 and 136 GeV",* Z. Phys. C **73** (1997) 433.

[11] P. Achard *et al.* [L3 Collaboration], *"Inclusive jet production in two-photon collisions at LEP",* Phys. Lett. B **602** (2004) 157 [arXiv:hep-ex/0410012].

[12] J. Allison *et al.* [OPAL Collaboration], *"The Detector Simulation Program for the OPAL Experiment at LEP",* Nucl. Instrum. Meth. A **317** (1992) 47.

[13] T. Sjostrand, *"High-energy physics event generation with PYTHIA 5.7 and JETSET 7.4",* Comput. Phys. Commun. **82** (1994) 74.

[14] G. A. Schuler and T. Sjostrand, *"A scenario for high-energy gamma–gamma interactions",* Z. Phys. C **73** (1997) 677 [arXiv:hep-ph/9605240].

[15] G. A. Schuler and T. Sjostrand, *"Towards a complete description of high-energy photoproduction",* Nucl. Phys. B **407** (1993) 539.

[16] F. A. Berends, P. H. Daverveldt and R. Kleiss, *"Radiative Corrections to the Process $e^+e^- \to e^+e^-\mu^+\mu^-$",* Nucl. Phys. B **253** (1985) 421.

[17] F. A. Berends, P. H. Daverveldt and R. Kleiss, *"Monte Carlo Simulation of Two Photon Processes. 1. Radiative Corrections to Multiperipheral $e^+e^-\mu^+\mu^-$ Production",* Comput. Phys. Commun. **40** (1986) 271.

[18] F. A. Berends, P. H. Daverveldt and R. Kleiss, *"Monte Carlo Simulation of Two Photon Processes. 2. Complete Lowest Order Calculations for Four Lepton Production Processes in Electron–Positron Collisions",* Comput. Phys. Commun. **40** (1986) 285.

[19] F. A. Berends, P. H. Daverveldt and R. Kleiss, *"Monte Carlo Simulation of Two Photon Processes. 3. Complete Lowest Order Calculations for $e^+e^- \to e^+e^-\mu^+\mu^-$ with Large Angle Tagging Conditions",* Comput. Phys. Commun. **40** (1986) 309.

[20] G. Marchesini, B. R. Webber, G. Abbiendi, I. G. Knowles, M. H. Seymour and L. Stanco, *"HERWIG: A Monte Carlo event generator for simulating hadron emission reactions with interfering gluons. Version 5.1 - April 1991",* Comput. Phys. Commun. **67** (1992) 465.

[21] G. Corcella *et al.*, *"HERWIG 6: An event generator for hadron emission reactions with interfering gluons (including supersymmetric processes)",* JHEP **0101** (2001) 010 [arXiv:hep-ph/0011363].

[22] S. Jadach, B. F. L. Ward and Z. Was, *"The Monte Carlo program KORALZ, version 4.0, for the lepton or quark pair production at LEP/SLC energies",* Comput. Phys. Commun. **79** (1994) 503.

[23] J. Fujimoto *et al.*, *"grc4f v1.1: A Four-fermion Event Generator for e^+e^- Collisions",* Comput. Phys. Commun. **100** (1997) 128 [arXiv:hep-ph/9605312].

[24] S. Catani, Y. L. Dokshitzer, M. H. Seymour and B. R. Webber, *"Longitudinally Invariant $k_\perp$ Clustering Algorithms For Hadron–Hadron Collisions",* Nucl. Phys. B **406** (1993) 187.

[25] G. Abbiendi *et al.* [OPAL Collaboration], *"Di-Jet Production in Photon–Photon Collisions at $\sqrt{s_{\rm ee}}$ from 189 to 209 GeV",* Eur. Phys. J. C **31** (2003) 307 [arXiv:hep-ex/0301013].

[26] A. M. Rooke, *"An analysis of the hadronic final state and jets in deep inelastic e-gamma scattering events using the OPAL detector at LEP",* PhD thesis, London Univ. (1998).

[27] J. Chyla and J. Cvach, *"Virtual photon structure from jet production",* arXiv:hep-ph/9707277.

[28] R. Hawkings, *"Tools for training and using neural networks",* OPAL Technical Note (1997) **TN501**.

[29] C. Peterson, T. Rognvaldsson and L. Lonnblad, *"JETNET 3.0: A Versatile artificial neural network package",* Comput. Phys. Commun. **81** (1994) 185.

[30] D. A. Karlen, *"Using projections and correlations to approximate probability distributions",* Comput. Phys. 12, 4 (1998) 380.

[31] G. Abbiendi *et al.* [OPAL Collaboration], *"Total hadronic cross-section of photon–photon interactions at LEP",* Eur. Phys. J. C **14** (2000) 199 [arXiv:hep-ex/9906039].

[32] M. Klasen, G. Kramer and B. Potter, *"Inclusive jet production with virtual photons in next-to-leading order QCD",* Eur. Phys. J. C **1** (1998) 261 [arXiv:hep-ph/9703302].

[33] S. Frixione, *"A general approach to jet cross sections in QCD",* Nucl. Phys. B **507** (1997) 295 [arXiv:hep-ph/9706545].

[34] S. Frixione and G. Ridolfi, *"Jet photoproduction at HERA",* Nucl. Phys. B **507** (1997) 315 [arXiv:hep-ph/9707345].

[35] M. Gluck, E. Reya and A. Vogt, *"Parton Structure of the Photon Beyond the Leading Order",* Phys. Rev. D **45** (1992) 3986.

[36] M. Gluck, E. Reya and A. Vogt, *"Photonic Parton Distributions",* Phys. Rev. D **46** (1992) 1973.

[37] *ATLAS Detector and Physics Performance: Technical Design Report, 2,* CERN (1999) Technical Design Report ATLAS.

[38] *Proceedings of the CERN Workshop on Standard Model Physics (and more) at the LHC,* 25 - 26 May 1999, CERN, Geneva, Switzerland.

[39] F. Abe *et al.* [CDF Collaboration], *"Observation of top quark production in $\bar{p}p$ collisions",* Phys. Rev. Lett. **74** (1995) 2626 [arXiv:hep-ex/9503002].

[40] S. Abachi *et al.* [DØ Collaboration], *"Observation of the top quark",* Phys. Rev. Lett. **74** (1995) 2632 [arXiv:hep-ex/9503003].

[41] S. W. Herb *et al.*, *"Observation of a dimuon resonance at 9.5 GeV in 400 GeV proton–nucleus collisions",* Phys. Rev. Lett. **39** (1977) 252.

[42] G. L. Kane and M. E. Peskin, *"A Constraint from B Decay on Models With No t Quark",* Nucl. Phys. B **195** (1982) 29.

[43] A. Bean *et al.* [CLEO Collaboration], *"Improved Upper Limit on Flavor Changing Neutral Current Decays of the b Quark",* Phys. Rev. D **35** (1987) 3533.

[44] D. P. Roy and S. Uma Sankar, *"B_d^0 – $\bar{B}_d^0$ Mixing as the Evidence for the Existence of the Top Quark",* Phys. Lett. B **243** (1990) 296.

[45] H. Albrecht *et al.* [ARGUS Collaboration], *"Observation of B^0 – $\bar{B}^0$ Mixing",* Phys. Lett. B **192** (1987) 245.

[46] H. Albrecht *et al.* [ARGUS Collaboration], *"A Study of $\bar{B}^0 \to D^{*+} l^- \bar{\nu}$ and $B^0\bar{B}^0$ Mixing Using Partial D^{*+} Reconstruction",* Phys. Lett. B **324** (1994) 249.

[47] J. E. Bartelt *et al.* [CLEO Collaboration], *"Two Measurements of $B^0\bar{B}^0$ Mixing",* Phys. Rev. Lett. **71** (1993) 1680.

[48] The ALEPH Collaboration, The DELPHI Collaboration, The L3 Collaboration, The OPAL Collaboration, The SLD Collaboration, The LEP Electroweak Working Group and The SLD Electroweak and Heavy Flavour Groups, *"Precision electroweak measurements on the Z resonance",* Phys. Rept. **427** (2006) 257 [arXiv:hep-ex/0509008].

[49] J. Pumplin, D. R. Stump, J. Huston, H. L. Lai, P. Nadolsky and W. K. Tung, *"New generation of parton distributions with uncertainties from global QCD analysis",* JHEP **0207** (2002) 012 [arXiv:hep-ph/0201195].

[50] R. Bonciani, S. Catani, M. L. Mangano and P. Nason, *"NLL resummation of the heavy-quark hadroproduction cross-section",* Nucl. Phys. B **529** (1998) 424 [arXiv:hep-ph/9801375].

[51] M. Jezabek and J. H. Kuhn, *"QCD Corrections to Semileptonic Decays of Heavy Quarks",* Nucl. Phys. B **314** (1989) 1.

[52] I. I. Y. Bigi, Y. L. Dokshitzer, V. A. Khoze, J. H. Kuhn and P. M. Zerwas, *"Production and Decay Properties of Ultraheavy Quarks",* Phys. Lett. B **181** (1986) 157.

[53] W. M. Yao *et al.* [Particle Data Group], *"Review of Particle Physics",* J. Phys. G **33** (2006) 1.

[54] O. S. Brüning, P. Collier, P. Lebrun, S. Myers, R. Ostojic, J. Poole and P. Proudlock, *"LHC Design Report",* CERN (2004).

[55] F. Carminati *et al.* [ALICE Collaboration], *"ALICE: Physics Performance Report, Volume I",* J. Phys. G **30** (2004) 1517.

[56] B. Alessandro *et al.* [ALICE Collaboration], *"ALICE: Physics Performance Report, Volume II",* J. Phys. G **32** (2006) 1295.

[57] S. Amato *et al.* [LHCb Collaboration], *"LHCb: Technical Proposal",* CERN (1998) LHC Experiments Committee.

[58] M. Della Negra *et al.* [CMS Collaboration], *"CMS Physics Technical Design Report",* CERN (2006) Technical Design Report CMS.

[59] G. Aad *et al.* [ATLAS Collaboration], *"The ATLAS Experiment at the CERN Large Hadron Collider",* JINST **3** (2008) S08003.

[60] A. S. Sidoti, *"The ATLAS Trigger Muon Slice",* IEEE Trans. Nucl. Sci. **55** (2008) 151.

[61] S. Armstrong *et al.*, *"Online Muon Reconstruction in the ATLAS Level-2 Trigger System",* IEEE Trans. Nucl. Sci. **53** (2006) 1339.

[62] G. Cataldi [ATLAS Collaboration], *"Muon Identification With the Event Filter of the ATLAS Experiment at CERN LHC",* IEEE Trans. Nucl. Sci. **53** (2006) 870.

[63] N. C. Benekos, *"Muon Identification and Reconstruction in the ATLAS Detector at the LHC",* Prepared for the 9th ICATPP Conference on Astroparticle, Particle, Space Physics, Detectors and Medical Physics Applications, Villa Erba, Como, Italy, 17-21 Oct 2005.

[64] S. Haas *et al.*, *"The Octant Module of the ATLAS Level-1 Muon to Central Trigger Process Interface"*, Proc. of the 12th Workshop on Electronics for LHC and Future Experiments (LECC 2006), Valencia, Spain, 25-29 Sep 2006, 319.

[65] The ATLAS Collaboration, *"Expected Performance of the ATLAS Experiment, Detector, Trigger and Physics"*, CERN-OPEN-2008-020, Geneva (2008), to appear.

[66] R. Bernhard *et al.* [CDF and DØ Collaboration], *"A Combination of CDF and DØ Limits on the Branching Ratio of* $B^0_{s(d)} \to \mu^+\mu^-$ *Decays"*, arXiv:hep-ex/0508058.

[67] T. Sjostrand, S. Mrenna and P. Skands, *"PYTHIA 6.4 Physics and Manual"*, JHEP **0605** (2006) 026 [arXiv:hep-ph/0603175].

[68] M. Smizanska, *"PythiaB: an interface to Pythia6 dedicated to simulation of beauty events"*, Technical Report ATL-COM-PHYS-2003-038, CERN (2003).

List of Figures

List of Tables